Peter Namdar, BSc

# Higher-Order Interference in Quantum Physics induced by Optical Nonlinearities

**MASTER'S THESIS**

to achieve the university degree of

Diplom-Ingenieur

Master's degree programme: Technical Physics

submitted to

**Graz University of Technology**

**Supervisor**

Assoc.Prof. Dipl.-Ing. Dr. Markus Koch
Institute of Experimental Physics, Graz University of Technology

in cooperation with

**Institute of Physics, University of Vienna**

Graz, 12 2020

# AFFIDAVIT

I declare that I have authored this thesis independently, that I have not used other than the declared sources/resources, and that I have explicitly indicated all material which has been quoted either literally or by content from the sources used. The text document uploaded to TUGRAZonline is identical to the present master's thesis.

---

Date, Signature

# ABSTRACT

In this work we aim to go deeper into the understanding of interference in quantum mechanics which was established from ideas taken from classical physics. We go beyond the conventional idea of second-order interference that was accepted to be the general situation for interfering quantum particles for more than a century and demonstrate a theoretical framework and an experimental setup to determine interference of third-order.

Since the beginning of the 20th century scientists have tried to interpret the behaviour of quantum particles with ideas from classical physics. In 1926, Max Born and Erwin Schrödinger formulated the basic relations for superposition and the wave behaviour of propagating quantum particles inspired by classical wave mechanics. While Schrödinger formulated a wave-equation to describe the behaviour of a quantum-particle, Max Born postulated a square-relation between the wave function $|\psi\rangle$ and a measurable observable like the position of the particle. This also led to the assumption, that interference only leads to a second-order term to describe the superposition of two quantum particles.

By redefining interference in general, a mathematical definition of higher-order terms can be expressed. In the last decade, a path was taken that started with ruling out higher order-interference in traditional slit experiments and has led to contemporary experiments which have found a non-vanishing third-order interference originating from Feynman paths.

In this work we present a different origin for third-order interference, originating from nonlinear optical interactions of photons. Using the framework of nonlinear optics, our idea shows that there is a third-order interference term for a system of three beams, interacting by $\chi^{(2)}$-processes in a nonlinear crystal. Furthermore, a quantum description for this system is given within this thesis and an experimental setup measuring a non-zero third-order interference component in a nonlinear optical system is presented. It thus encourages further investigation on higher-order interference due to nonlinear coupling.

# ZUSAMMENFASSUNG

In dieser Arbeit versuchen wir, das Verständnis vom herkömmlichen Begriff der Interferenz in der Quantenmechanik, welcher aus etablierten Ideen der klassischen Mechanik abgeleitet wurde, zu erweitern. Wir hinterfragen die Konvention, Interferenz als Phänomen zweiter Ordnung zu verstehen, welche für über 100 Jahre Gültigkeit behielt, und zeigen eine theoretische Formulierung und einen experimentellen Aufbau, um Interferenz dritter Ordnung zu messen.

Anfang des 20. Jahrhunderts wurde versucht, grundlegende quantenphysikalische Phänomene anhand des Wissens über klassische Physik zu beschreiben. Im Jahr 1926 haben Max Born und Erwin Schrödinger in deren jeweiligen Arbeiten hierbei die Beschreibungen zur Superposition und Ausbreitung von Quantenteilchen formuliert. Während Erwin Schrödinger eine Wellengleichung zur Fortbewegung von Quantenteilchen darlegte, hat Max Born einen quadratischen Zusammenhang zwischen einer Wellenfunktion $|\psi\rangle$ und einer Messgröße, zum Beispiel dem Ort, festgestellt. Dadurch sind auch Interferenzterme, welche durch die Superposition zweier oder mehrerer Wellen entstehen, von zweiter Ordnung. Durch eine generelle Formulierung von Interferenz kann eine mathematische Definition von Interferenztermen höherer Ordnung gegeben werden. Im letzten Jahrzehnt hat sich dadurch ein spannender Weg von der Reduzierung des Interferenzverhaltens auf zweite Ordnung in üblichen Spaltexperimenten mit zeitgemäßen Messauflösungen bis hin zur Detektion von Interferenz dritter Ordnung, entstehend durch exotische Feynman-Pfade, ergeben. In dieser Arbeit setzen wir den Weg fort und präsentieren einen weiteren Ursprung für Interferenzterme höherer Ordnung, resultierend aus einem Gebiet der nichtlinearen Optik, nämlich nichtlinearen Prozessen zweiter Ordnung. Dies hat in Berechnungen ergeben, dass in einem System von drei interagierenden Lichtstrahlen in einem nichtlinearen Kristall Interferenzen dritter Ordnung auftreten. Ebenso wird ein quantenmechanisches Modell zur Beschreibung des Systems dargelegt. Des Weiteren wurde ein Experiment aufgebaut und durchgeführt, das Interferenz dritter Ordnung in solchen Systemen zeigt. Dies ermutigt zu weiteren Untersuchungen nichtlinearer Systeme auf Interferenzen dritter Ordnung und die genaue Quantifizierung dessen, sowie der Formulierung des Ergebnisses im Zuge der Quantenmechanik.

# ACKNOWLEDGEMENTS

First of all, I would like to thank Univ.-Prof. Philip Walther for letting me be part of this research group. It not only allowed me to discover various topics and doing research in the foundations of quantum physics, but also to develop myself further in a different environment. Therefore, I would also like to express my gratitude to Lee Rozema for always answering my questions and being that brilliant physicist, but also for giving me space and trust to develop our ideas further - conceptionally, theoretically and experimentally.

I would like to thank Alessandro Trenti for introducing me to the interesting field of nonlinear optics and the supervision of the nonlinear optical calculations, as well as Irati Alonso Callafel for introducing me to the lab work, all the components and methods and giving helpful experimental input in general. I also want to thank Philipp Jenke for his support with all the Python-problems. Besides answering all the questions about theoretical physics, Ass.-Prof. Borivoje Dakić supported me with his great teaching and introduced me to theoretical quantum optical methods in his lectures, on the corridor and in his or our office. Thank you, Bori! I would also like to express my gratitude to Dr. Milan Radonjić from the Univesity of Kaiserslautern for his helpful input on theoretical calculations and Mathematica and to Assoc.Prof. Markus Koch for the uncomplicated and kind communication and processing.

It was far more than just lunch sessions where I enjoyed the company of Ale, Sophie, Stefan, Beate, Ira, Philipp, Sebastian, Nicolas, Fatemeh, Josh, Michele, Raffa, Lee, Guilherme and many more. I would like to thank all of you for the mutual support in the challenging times of 2020 with lockdown(s) and political actions, when life was not easy for all of us.

Since the research work was also connected with living in a different city, I would like to express my gratitude to my flatmates: Big thanks to Jakob for our numerous cooking and music sessions, Joane and Herr Weber for sharing a great time even during lockdown and Jana for always having an open ear. Furthermore some old friends welcomed me warmly to Vienna: Thanks to Eli, Nikos, Eva, Lena, Thomas, Mona and all the others! I also want to thank Klemens for keeping me on track with our numerous discussions on physics and technics, music and everything in between.

Last but definitely not least I want to express my deepest gratitude to my wonderful siblings and parents for their endless support. Because of my mum and dad I was able to visit Singapore and Vienna during my studies and to always go my own way. Thank you!

# CONTENTS

# LIST OF FIGURES

# 1 INTRODUCTION

In general, quantum mechanics is accepted to be a precisely predicting theory within its boundaries describing a world far beyond the length scale we got used to during the evolution of human beings. Based on some axioms and new ideas, specific experimental setups and thought experiments came up in the beginning of the 20th century and were used to describe some key ideas of this new field of physics discovered and developed by Niels Bohr, Erwin Schrödinger, Werner Heisenberg, Max Born, Albert Einstein - who was not only a supporter of the consequences of the recent quantum ideas back then - and many more.

One of the key experiments in the beginning of quantum mechanics was the famous double-slit experiment. Although it was first introduced by Thomas Young in 1801 to demonstrate the wave nature of light, it revealed even deeper insight into the behaviour of quantum particles about 100 years later. Indeed, Richard Feynman said 'the double-slit experiment has in it the heart of quantum mechanics. In reality, it contains the only mystery.' On the one hand it showed that some mysterious 'collapse' of the wave behaviour towards particle behaviour takes place as a consequence of a measurement, and, on the other hand, it demonstrated the superposition of two paths of a quantum particle and its interference. In this work, we deal with the experimental realization of new theoretical concepts coming from interference in quantum physics. In general, interference is obtained when two waves interact according to the superposition principle. In every common classical wave theory there is a square-relation between amplitude or field and the intensity of a wave. In quantum mechanics a similar relation was found; the so-called Born's rule, formulated by Max Born in 1926. This rule leads intuitively to second-order terms as interference terms, which means that in a double-slit experiment both slits always contribute to the interference of wave functions by their product. To prove this assumption, experiments with more slits were conducted and the outcome interference pattern was always shown to be reducible to second-order terms. However, recent theoretical work by Rozema L., et al. (2020) [21] showed that the observation of the interference pattern was generally done within linear quantum systems. In addition, it was mathematically shown that within certain nonlinear systems, interference of higher order can be observed. In this work, the first experimental realization of such a system and the first measurement of higher-order interference due to nonlinearities is described. In the experiment, up to three laser beams interact with each other in a nonlinear crystal in analogy to the triple-slit experiment. All interactions happen due to $\chi^{(2)}$-processes of sum-frequency generation, difference-frequency generation and full three-wave mixing. The outgoing power of the incoming and the generated beams then give insights into the interference caused by nonlinear optical effects. We use descriptions in the framework of nonlinear and quantum optics to describe the physics behind the experiment. Although instabilities are currently present in the experiment, we can observe the presence of third-order interference and our setup will allow us to precisely quantify higher-order interference in near future.

In chapter 2 we start from traditional slit experiments and the common understanding of interference and give an overview of the role that Feynman paths played towards the observation of higher-order interference. We then mention recent theoretical concepts of how a nonlinear system can lead to higher-order interference. This was our motivation for developing a specific scenario to find third-order interference. We show how three-photon processes can induce third-order interference in experimental setups and present our rudimentary calculations that motivated us to realize the work described in this thesis.

In chapter 3 the physical and mathematical foundations for this work are presented. In section 3.1 we show the foundations of nonlinear optics that are necessary to understand and later calculate the experimental processes in more detail. Section 3.2 states that the idea of reducing interference to second-order originates already from classical physics. Section 3.3 provides the quantum optical foundations for the calculations done in chapter 5.

In chapter 4 a model for second-harmonic generation including the phenomena of spatial and temporal walk-Off as well as depletion of beams, formulated by Wang H. and Weiner A. (2004) [11], was taken and combined with fundamental three-wave mixing equations and modified to also give predictions about all the nonlinear processes in our experiment, including difference-frequency generation of photons and three-wave mixing. With the description of all these processes for our experimental arrangements we could make a prediction for non-vanishing higher-order interference. In our case this was for third-order interference. This furthermore gives insights into the consequences of experimental imperfections onto the outcome of the experiment.

In chapter 5, experimental data and a theoretical model from quantum optics were used to describe the behaviour of the system and the nonlinearity of the sum-frequency process was approximated by a Baker-Campbell-Hausdorff expansion and further mathematical treatment. However, its general formulation allows it to be easily adapted to the other $\chi^{(2)}$ processes described by the same Hamiltonian. Therefore it should be possible to describe third-order interference when a solid set of measurements is taken and associate it with nonlinear processes by the help of our model. This is work will be done in near future.

In chapter 6 the setup, experimental details and the results are described in detail. A focus is set on showing the relations between the nonlinearity of the processes and the third-order interference terms with two different measurement methods.

All in all, it is exciting for me to show within this thesis that even well-established phenomena and assumptions within a theory solid as quantum mechanics can be shown to be only valid within certain regimes. Furthermore, we could already show within the theoretical predictions that the presence of third-order interference does not necessarily require a post-quantum theory, but could be explained by a better understanding of basic concepts of quantum mechanics.

# 2 BASIC IDEA OF HIGHER-ORDER INTERFERENCE

In this chapter we go from traditional slit experiments and the common understanding of interference towards modern approaches and the first observations of third-order interference caused by exotic Feynman paths. We then show new theoretical approaches to obtain higher-order interference from nonlinear interactions and present our basic idea of how to realize that in an experiment. In section 2.1 we start from the superposition of quantum particles and Born's rule and see how interference in slit experiments is always reduced to second-order independent of the number of slits. We then show how a small theoretical third-order contribution is caused by Feynman paths and review their experimental observation. In section 2.2 we go from recent theoretical approaches towards our idea of taking specific nonlinear interactions between photons to obtain third-order interference. We present first calculations that show that our ideas should indeed allow for third-order interference.

## 2.1 FROM RULING OUT TO OBSERVING HIGHER-ORDER INTERFERENCE IN SLIT EXPERIMENTS

Interference is a general concept in every wave theory in classical as well as in quantum physics. It is a direct consequence of the superposition of two waves or more. Since interference has already been defined and experimentally observed in detail for classical wave phenomena for centuries, in the beginning of quantum mechanics the assumption came up that quantum physics is based on wave functions to describe the behaviour of quantum particles. The key interference experiment, originally in classical and later in quantum physics, is the double-slit experiment. Originally performed by Thomas Young in 1801 to show the wave nature of light [31], it was later directly performed to demonstrate the superposition of quantum particles. Even one particle was shown to interfere with itself [2] and it also led to a demonstration of wave-particle duality for quantum particles in general [7]. In figure 2.1 the solid black pattern shows the intensity pattern of a double-slit experiment with both slits open, while the green dashed lines show a scenario with one slit blocked. In this work we follow the standard textbook interpretation of quantum mechanics, meaning that the quantum particle propagates as a probability wave that collapses to, for instance, a particle at a specific position when its position is measured [32].

When the probability waves in the double-slit experiment are not collapsed before hitting the screen by measurements, an intensity pattern at the screen establishes over time following the probability density of the photons. The photons are described

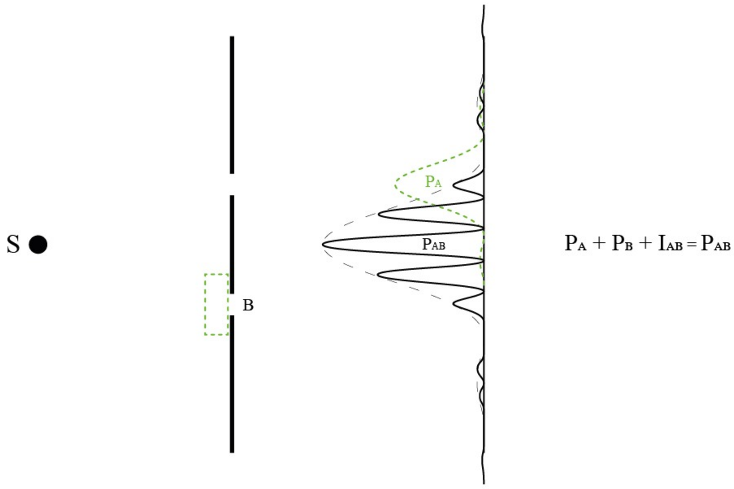

**Figure 2.1: Intensity pattern in the double-slit experiment.** It is the go-to experiment to demonstrate interference as well as the wave-particle dualism in quantum mechanics. When not collapsed first, photons or any other quantum particles behave as waves when propagating through a double-slit configuration. At a screen behind the slit to detect the position of the particle, it's wave function is collapsed to a position determined statistically from the wave function. $P_{AB}$ is the intensity pattern when both slits are open and $P_A$, represented by the green dashed line, is the intensity pattern for only slit $A$ open and $B$ blocked. It can be seen by the dashed black line, that the envelope of a double-slit pattern has the form of a single-slit outcome.

by the wave function $\psi$. The square-relation between the amplitude of a wave and its intensity in classical physics inspired Max Born to find a fundamental relation in quantum mechanics; known as Born's Rule [32]. While the state $|\psi(\vec{x},t)\rangle$ is not measurable itself, the absolute value squared,

$$P(\vec{x},t) = \left|\psi(\vec{x},t)\right|^2, \tag{2.1}$$

is the direct probability of finding particle $\psi$ at time $t$ at position $\vec{x}$. $P(\vec{x},t)$ is known as the probability density of the state $|\psi(\vec{x},t)\rangle$ and in the case of the double-slit experiment a pattern like in figure 2.1 is obtained over time when the experiment is conducted with many photons.

### 2.1.1 Interference of photons

One reason why the double-slit experiment is the go-to experiment to demonstrate interference in quantum mechanics is the simple demonstration of superposition, both experimentally and mathematically. Since there are no specific interactions between the two paths, the pattern can be described as follows: As shown in figure 2.1 the two slits are referred to by the labels 'A' and 'B' and the paths assigned to those slits are described by the wave functions $|\psi_A\rangle$ and $|\psi_B\rangle$. Evaluating the probability density of each of those states would give a pattern as if only the specific slit was open and the other slit closed, e.g. sketched by the probability density $P_A$. Now the observed pattern when both slits are open can be directly obtained by applying Born's rule of the superposition of the two paths:

$$P_{AB} = |\psi_A + \psi_B|^2 = \underbrace{|\psi_a|^2}_{P_A} + \underbrace{\psi_A^* \psi_B + \psi_A \psi_B^*}_{I_{AB}} + \underbrace{|\psi_B|^2}_{P_B} \tag{2.2}$$

When analyzing equation 2.2 it is obvious that the first and the last term on the right side are equal to the probability densities of a wave function in a single slit experiment. The superposition of the waves and the evaluation via Born's rule leads to the terms with contribution of both slits $\psi_A^{(*)} \psi_B^{(*)}$. This makes the double-slit result differ from the sum of the individual single-slit results; those terms are referred to as interference term $I_{AB} = \psi_A^* \psi_B + \psi_A \psi_B^*$. A deeper insight in superposition and interference is given in section 3.2. The probability density of equation 2.2 can then be written as

$$P_{AB} = |\psi_A + \psi_B|^2 = P_A + I_{AB} + P_B \ . \tag{2.3}$$

The square relation in Born's rule leads to the product of $\psi_A$ and $\psi_B$ as interference terms, which are mathematically of second order. It is of importance for this work to notice that there is no source for a third- or higher-order interference term in the double-slit experiment.

### 2.1.2 Interference in the Triple-Slit Experiment

The triple-slit experiment is the straight-forward extension of a double-slit experiment: A source of quantum particles, in our case photons, is sent onto a mask with three slits and the resulting intensity pattern along an axis parallel to the mask is observed on a screen. The setup is sketched in figure 2.2. To analyze the probability density and the corresponding interference, the same procedure as in the double-slit experiment can be applied. Again, due to no interactions between the paths, the superposition of the wave functions $\psi$ of the individual slits can be evaluated by Born's rule as in equation 2.3 [24].

$$P_{ABC} = |\psi_A + \psi_B + \psi_C|^2 \tag{2.4}$$

$$= |\psi_A|^2 + |\psi_B|^2 + |\psi_C|^2 + \psi_A^* \psi_B + \psi_A \psi_B^* + \psi_A^* \psi_C + \psi_A \psi_C^* + \psi_B^* \psi_C + \psi_B \psi_C^* \tag{2.5}$$

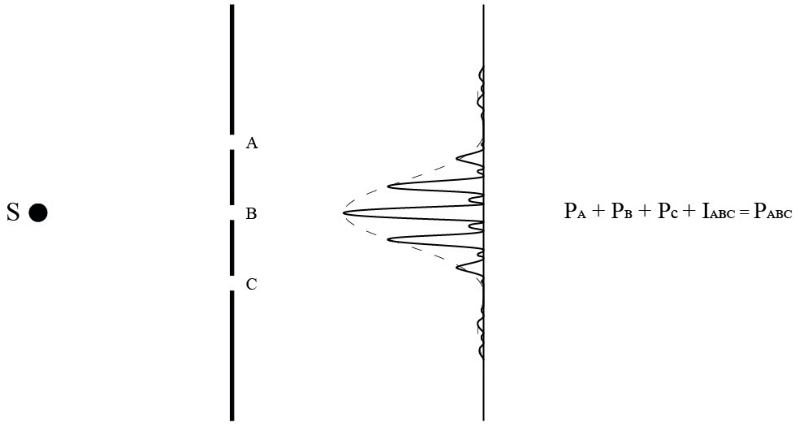

**Figure 2.2: Intensity pattern in the triple-slit experiment.** To demonstrate and observe interference in quantum mechanics, the triple slit experiment can be taken as a follow-up setup from the double-slit experiment. A source is sending photons onto a mask with three slits labelled as slits $A$, $B$ and $C$. On a screen behind the mask, the resulting intensity pattern $P_{ABC}$ parallel to the mask is measured. By blocking individual slits, the identical configuration as in a corresponding single- or double-slit experiment can be obtained.

By analyzing equation 2.5 and formulating it as single-slit patterns and interference terms as in equation 2.3, it can be written as

$$P_{ABC} = P_A + P_B + P_C + I_{AB} + I_{AC} + I_{BC} \ . \tag{2.6}$$

Even though the experiment is performed with three slits open, it is reducible to probability densities of individual single-slit experiments and second-order interference terms. As a first step towards generalization, apparently triple-slit experiments also lead to interference terms of only second-order. When performing the same analysis to experiments with more slits open, it is always reducible to intensity patterns of individual single-slit terms and second-order interference terms due to the superposition principle and Born's rule.

Therefore, interference in quantum mechanics can generally be reduced to second-order. Several communities within the foundations of quantum mechanics have even termed it as a second-order theory [24].

### 2.1.3 The Sorkin parameter and higher-order interference

Born's rule is an axiom within quantum mechanics and was determined empirically to be true in several interference experiments. However, due to the dependence of the order of interference on Born's rule it is crucial to prove its validity also for experiments with more slits to eliminate higher-order interference patterns.
When subtracting all the single-slit patterns $P_j = |\psi_j|^2$ and the interference patterns $I_{ij}$ from the total probability density $P_{ABC}$, the outcome value is expected to vanish:

$$P_{ABC} - P_A - P_B - P_C - I_{AB} - I_{AC} - I_{BC} = 0 \tag{2.7}$$

Equation 2.6 can also be equivalently replaced by probability densities only as shown in equation 2.3:

$$P_{ABC} - P_{AB} - P_{AC} - P_{BC} + P_A + P_B + P_C = 0 = \kappa \tag{2.8}$$

Equation 2.8 consist purely of intensity patterns and therefore it is directly measurable. This is the main formulation of the triple-slit experiment when proving its concept experimentally. The parameter $\kappa$ was therefore introduced since it can be directly observed in an experiment. $\kappa$ is known as the Sorkin paramter, named after Raphael Sorkin who was the first one to theoretically question the order of interference in quantum mechanics [26]. As described in this chapter it is expected to be zero when the physics of the experiment can be described by Born's rule. On the other hand, a non-vanishing Sorkin parameter would mean, the assumptions taken in this description and wrong and need to be adapted.

### 2.1.4 Experimental observation of the Sorkin parameter

Since an experiment to prove the boundaries of Born's rule was inspiration for this work and directly made use of equation 2.8, I will briefly explain it here: As mentioned in section 2.1.2, the assumption of breaking down a triple-slit experiment to the superposition principle using Born's rule leads to intensity terms that can directly be measured. A team around Urbasi Sinha in the group of Gregor Weihs conducted a triple-slit experiment in 2010 and proved Born's rule to hold up to small experimental errors [24]: Each term in equation 2.8 can be directly determined by blocking the slits that are not indicated in the individual term. By making use of a mask that contains all the necessary permutations of the combination of slits, the Sorkin parameter was directly obtained. A sketch of the mask is shown in figure 2.3. It can be seen, that all the necessary slit arrangements can be set with the mask.

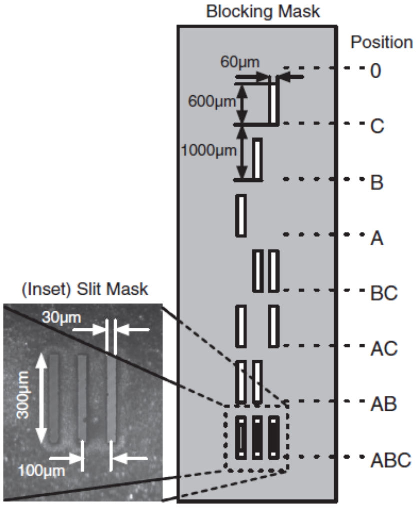

**Figure 2.3: The mask used in Ref. [24] to test Born's rule.** The mask contains all the combinations to conduct singe-slit experiments (A, B and C), double-slit experiments (BC, AC and AB), the triple-slit combination (ABC) and the background noise (0). (Figure taken from Sinha U., et al. (2010) [24].)

By adding a term for the background noise $P_0$, the experimental evaluation was done with a parameter formulated as

$$\kappa = P_{ABC} - P_{AB} - P_{AC} - P_{BC} + P_A + P_B + P_C - P_0 \ . \tag{2.9}$$

The experiment was conducted with three different source and detector configurations. In figure 2.4 two of the results are shown graphically and quantitatively. In configuration (**a**) a laser was taken as a light source and a powermeter unit as detector. In configuration (**b**) a single-photon source was used and a so-called Avalanched Photon Detector (APD) as detection unit.

While single-photon states can obviously be explained by quantum mechanics, laser light can also be described as so-called coherent states (see chapter 2.2.2) within quantum mechanics. This made both configurations useful for proving Born's rule. The evaluation of equation 2.9 led to a Sorkin parameter smaller than 0.01 and was therefore taken as not significantly deviating from zero and lying within experimental imperfections. This could be taken as a test of Born's rule for various slit-experiments which also means that the interference patterns can be reduced to second-order.

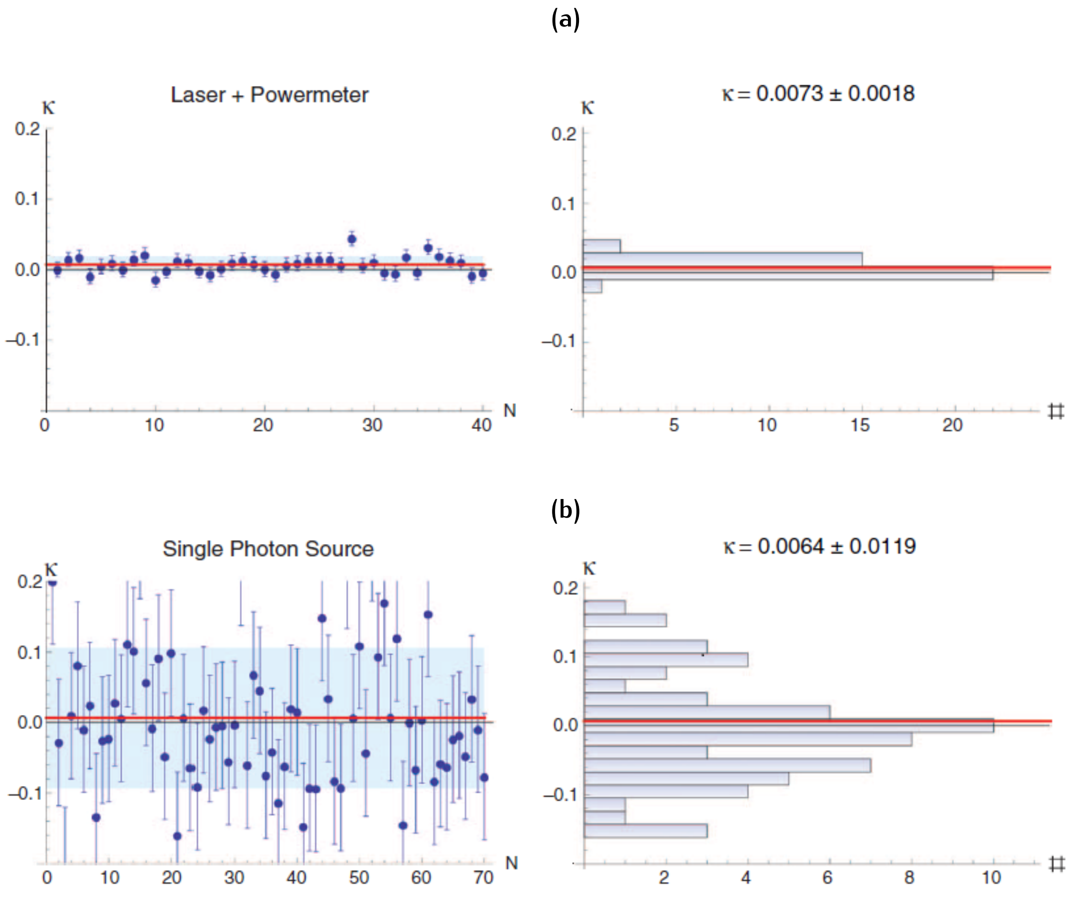

**Figure 2.4: The results of the experiment conducted by Sinha, U. et al. (2010)** [24]. The mask of figure 2.3 was taken and a photon source and a detector to measure the light intensity behind the mask. In (**a**) a Laser was taken as a source and a powermeter unit as a detector. In (**b**) single photons were used and detected by APD-units. The obtained Sorkin parameter was vanishing up to $10^{-2}$ which was within the range of experimental imperfections.

### 2.1.5 Third-Order Interference through Exotic Looped Paths

According to quantum mechanics, each particle propagating from A to B via its wave function has a contribution in its motion from every possible path as Richard Feynman described in 1948. He also provided the tool to describe this phenomenon, today known as Feynman Path Integrals [8]. In the case of a double-slit experiment this means that a part of the contribution of a particle starting at the source point S goes through slit A, then back through slit B and again through slit A to finally arrive at the final position D. In theory this is even possible to measure with a very small, yet finite, probability. It was first calculated by H. Yakubi in 1986 [30]. The same scenario applies to every other possible path between S and D. In the case of a triple-slit experiment, this could look like the path demonstrated in figure 2.5. One should keep in mind that according to the standard interpretation of quantum mechanics this cannot be seen as a particle-like

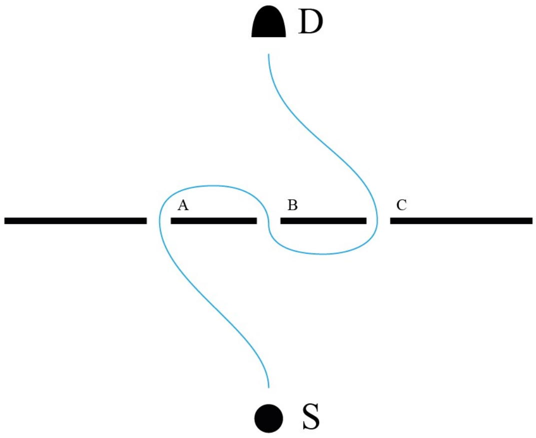

**Figure 2.5: Conceptual sketch of a possible path in a triple-slit configuration.** As described by the Feynman Path Description of Quantum Mechanics, a particle emitted from a source S can go through slit A, than go back through slit B and again to slit C to afterwards propagate towards the final detector D [23].

target propagating in a deterministic way from S towards slit A, then back through slit B and again through slit C to finally arrive at D, but as a contribution in the behaviour of the wave function in a system described by its Hamiltonian. When measuring, the wave function collapses in a probabilistic way so that a certain path was taken. The probability of the looped paths (as in figure 2.5) to occur - including the symmetrically equivalent path where slit C is entered before slit B and A - was calculated by Rahul, S. et al.in 2014 [23]. In principle, the contribution of any path follows the least-action-principle, which makes the standard paths occur much more likely than any exotic path [8].

The optimized configuration for obtaining a non-zero Sorkin parameter from looped trajectories in a triple-slit experiment with optical wavelengths turned out to be "*slit width* $d_s = 30\ \mu m$, *interslit distance* $d_{id} = 100\ \mu m$, *distance between source and slits and slits and detector* $d_{ss,sd} = 18\ cm$ *and incident wavelength* $\lambda = 810\ nm$" [23]. These are experimentally challenging parameters that are hard to realize. However, one can see that third-order interference from looped paths exists in theory. In 2016 Magana-Loaiza, O. et al. have shown that looped paths in a triple-slit experiment would indeed lead to higher-order interference [17]. In the experiment, surface plasmons in a gold sample have been excited by incident light. Above the sample, a triple slit mask was placed and due to the experimental arrangement, when incident light was sent onto slit A, surface plasmons with their Poynting vectors as shown in figure 2.7 were present such that photons were emitted from the part of the sample below slit C, as shown in figure 2.7. When placing different masks to observe the different components of the Sorkin parameter, similar to 2.3, the result from figure 2.8 is obtained. In figure 2.8 the Sorkin parameter is evaluated and plotted. The blue line shows the theoretical calculations and the dots the measured data. It therefore becomes clear, that looped paths lead to a non-vanishing Sorkin parameter.

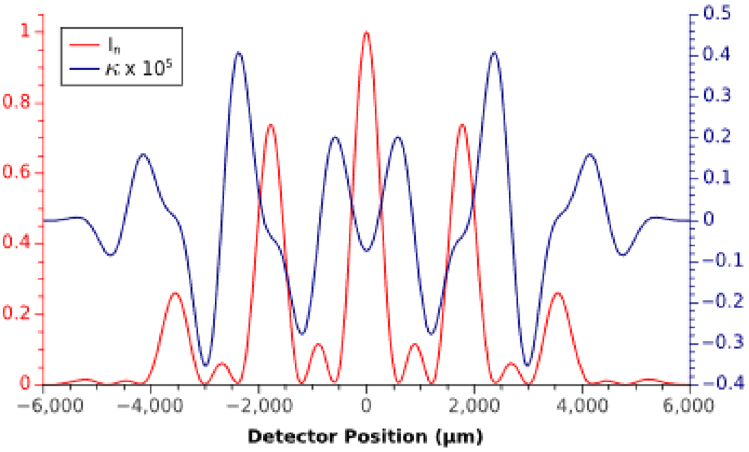

**Figure 2.6: The normalized Sorkin parameter in a triple-slit configuration.** The calculation is fully theoretical. The red line represents the intensity normalized by the maximum intensity at the detecting screen. The x-axis shows the detector position parallel to the plain of the mask. The position '0' is centered to the middle slit. These are the conditions for a theoretically optimized $\kappa$ with "slit width $d_s = 30\ \mu m$, interslit distance $d_{id} = 100\ \mu m$, distance between source and slits and slits and detector $d_{ss,sd} = 18\ cm$ and incident wavelength $\lambda = 810\ nm$" (Rahul, S. et al. (2014)) [23]. (Taken from Ref. [23].)

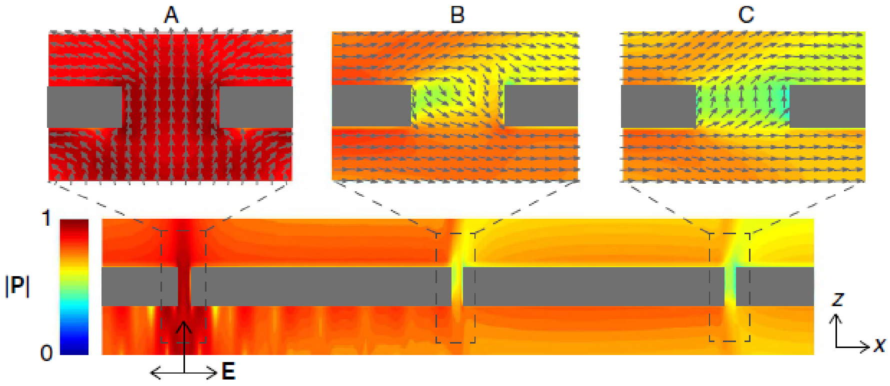

**Figure 2.7: A triple-slit arrangement with a mask above a gold sample from [17].** In the sample surface plasmons can be exited. By specific arrangements, specific alignments of the Poynting vectors can be obtained. The little arrows demonstrate the alignments of the Poynting vector of the excited surface plasmons in the gold sample when slit A is hit by incident light. The parameters are explained in detail in Ref. [17]. (Taken from Ref. [17].)

Indeed, in 2018 it was proven for the first time that such exotic paths occur in reality also in free space and cause a non-vanishing Sorkin parameter. In an experiment of Rengaraj, G. et al. (2018) it was demonstrated, that when looped paths are prevented, the Sorkin parameter $\kappa$ vanishes [20]. The contribution of the looped paths can be

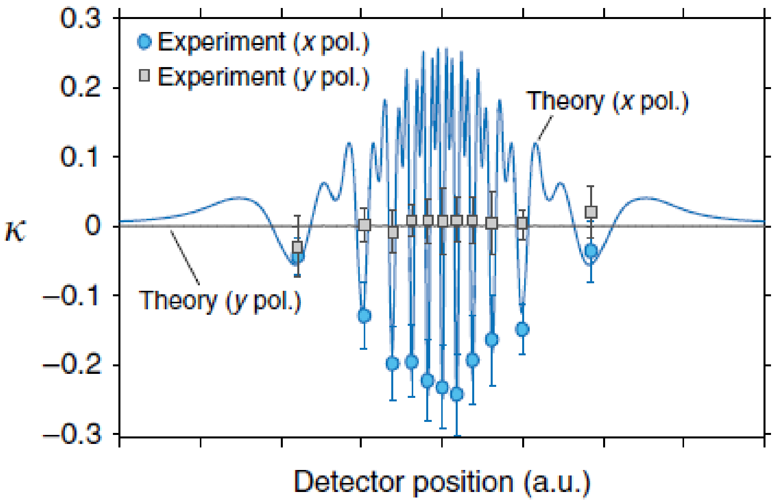

**Figure 2.8: The Sorkin parameter obtained by surface plasmons in a gold-sample in the experiment of** [**17**]**.** The blue dots describe the measured Sorkin parameter and the blue line shows the theoretical predictions. The grey dots show the data without surface plasmons and the grey line the theoretical predictions. (Taken from Ref. [17].)

decreased by baffles as shown in figure 2.9. The size of the baffles were varied between each set of measurements to associate the Sorkin parameter with the prevention of looped paths. The results are shown in figure 2.10. It can be seen that indeed the Sorkin parameter decreases with a bigger baffle size as the exotic paths are prevented [20]. The experiment was conducted with microwaves and very specific experimental parameters, which show that significant looped paths are only present in specific cases.

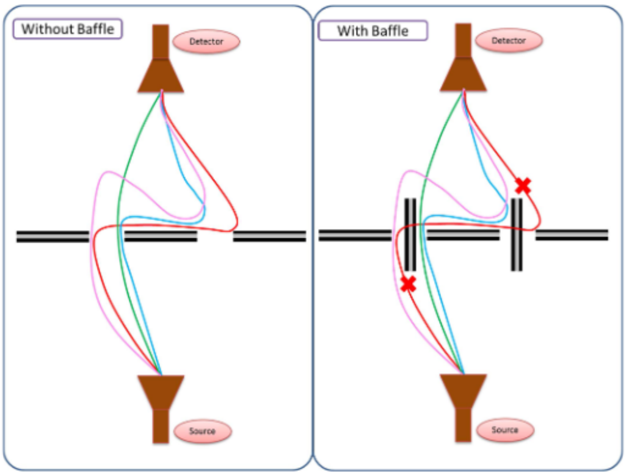

**Figure 2.9: Baffles to prevent exotic loops in Ref.** [20]. In the experiment by Rengaraj, G. et al. (2018) [20] baffles were inserted to block looped paths in the triple-slit experiment. Each set of measurements of a Sorkin parameter was done with a certain baffle size that was varied afterwards. (Taken from Ref. [20].)

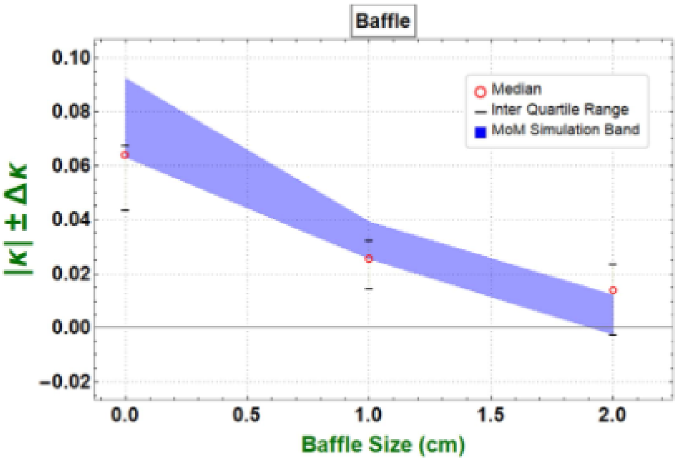

**Figure 2.10: The Sorkin parameter as a function of the baffle size in the experiment of Rengaraj, G. et al.** [20]. The red points show the data from 10 sets of measurements each and the blue area the result of theoretical simulations. (Taken from Ref. [20].)

## 2.2 HIGHER-ORDER INTERFERENCE IN QUANTUM MECHANICS

However, as shown in a theoretical paper by Rozema L., et al. (2020) [21], there can be a different origin of higher-order interference. Actually, it can reach up to any arbitrary order depending on the experimental arrangement. It is based on nonlinear multi-particle interactions that are not typically present in a simple multi-slit interference experiment. Furthermore, it can be fully expressed within the framework of quantum physics and does not require any post-quantum theory.

In the theoretical work, the description was done within second quantization. To define the order of interference in an arbitrary system, as a first step a look at a scheme like sketched in figure 2.11 is taken.

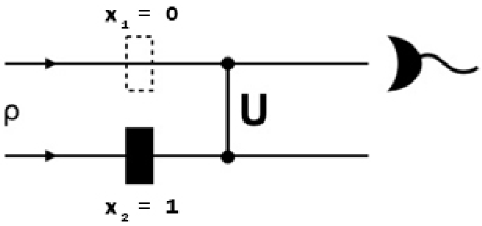

**Figure 2.11: A general two-path setup.** Two paths associated with an arbitrary quantum state described by $\rho$ can be individually kept open or being blocked. In this case, the upper part is open and therefore assigned a blocking configuration $x_1 = 0$ and the lower path is blocked with $x_2 = 1$, respectively. The paths afterwards interact by an unitary operator $U$ and the intensity in a path, in this case the upper one, is measured by a detector. (Figure adapted from [21].)

Two paths, where each one can be blocked or kept open, are shown. The paths are assigned to any quantum state represented by the density matrix $\rho$, as for instance given by photons moving along trajectories. They then interact by a unitary operator and the intensity in the specific path is measured afterwards. To denote different configurations, a path $j$ is assigned with the blocking configuration $x_j = 0$ when open or $x_j = 1$ when blocked. A configuration as in figure 2.11 is then described by $[x_1 = 0, x_2 = 1]$ and the associated intensity is denoted as $I_{01}$ . For each configuration, a measurement of the intensity can be taken along each part. To stay consistent, the measurement is here always taken in the first path. As described by the double-slit experiment in section 2.1.1, interference is the component of intensity that makes the pattern with both slits open differ from individual configurations. In direct analogy, this can be generalized and the interference component $\mathcal{I}_2$ for the two-path setup can be expressed as

$$\mathcal{I}_2 = I_{00} + I_{11} - I_{01} - I_{10} \ . \tag{2.10}$$

For the general case of $M$ paths, equation 2.10 can be generalized to

$$\mathcal{I}_M = \sum_{x_1,\ldots,x_M=0}^{1} (-1)^{x_1+\cdots+x_M} I_{x_1\ldots x_M} \text{ [21]}. \tag{2.11}$$

Besides the well-defined paths, the rest of the double-slit setup is equal to the two-path setup. In our case, each path can be opened or closed and each intensity term is always measured in one specific path, e.g. the first one. The non-vanishing $\mathcal{I}_M$ with the highest number of paths is then the order of interference for the present configuration. R. Sorkin has shown, that if for any $M$ $\mathcal{I}_M$ vanishes, all the higher-order components also vanish [26].
It can be seen that equation 2.11 is identical to equation 2.10 for the two-path case. For three paths, equation 2.11 becomes a form equivalent to the Sorkin parameter in section 2.1.2, pointing out that the Sorkin parameter is equivalent to third-order interference as discussed in Ref. [21]:

$$\mathcal{I}_3 = I_{000} - I_{100} - I_{010} - I_{001} + I_{110} + I_{101} + I_{011} - I_{111} \tag{2.12}$$

### 2.2.1 Generalizing second-order interference and single photon states in a setup

When well defined paths are considered, unlike in the slit experiments but as in the experiments described in this work, it can be shown that with single-photons the interference reduces also to second-order. To show this, we provide the following calculation: Assuming a single-photon input state with a superposition in the three paths a, b and c,

$$|\psi\rangle = \alpha\,|a\rangle + \beta\,|b\rangle + \gamma\,|c\rangle \tag{2.13}$$

where $|\alpha|^2 + |\beta|^2 + |\gamma|^2 = 1$ and a random three-dimensional unitary operator

$$\begin{pmatrix} U_{11} & U_{12} & U_{13} \\ U_{21} & U_{22} & U_{23} \\ U_{31} & U_{32} & U_{33} \end{pmatrix} \tag{2.14}$$

acting on the input state, the state after the unitary operator is described by $|\psi\rangle' = U\,|\psi\rangle$. Expressed in the basis of the three paths, the state can be expressed by

$$\begin{pmatrix} U_{11} & U_{12} & U_{13} \\ U_{21} & U_{22} & U_{23} \\ U_{31} & U_{32} & U_{33} \end{pmatrix} \begin{pmatrix} \alpha \\ \beta \\ \gamma \end{pmatrix} = \begin{pmatrix} \alpha\, U_{11} + \beta\, U_{12} + \gamma\, U_{13} \\ \alpha\, U_{21} + \beta\, U_{22} + \gamma\, U_{23} \\ \alpha\, U_{31} + \beta\, U_{32} + \gamma\, U_{33} \end{pmatrix}. \tag{2.15}$$

The probability of finding the photon in path a is then described by $\left|a'\right|^2 = \left|\alpha\ U_{11} + \beta\ U_{12} + \gamma\ U_{13}\right|^2$. Meaning that for the configuration of all three paths open, the probability to find the single-particle then at path a is

$$I_{000}: \quad \begin{aligned} \left|\alpha'\right|^2 = {} & |\alpha|^2\ |U_{11}|^2 + |\beta|^2\ |U_{22}|^2 + |\gamma|^2\ |U_{33}|^2 \\ & + \beta\alpha^* U_{12} U_{11}^* + \gamma\alpha^* U_{13} U_{11}^* + \alpha\beta^* U_{11} U_{12}^* \\ & + \gamma\beta^* U_{13} U_{12}^* + \alpha\gamma^* U_{11} U_{13}^* + \beta\gamma^* U_{12} U_{13}^*. \end{aligned} \tag{2.16}$$

For a Sorkin parameter measured at path a, this can be interpreted as the $I_{000}$-term. $I_{001}$ would be the same procedure with a blocked path c, meaning the input state would become

$$|\psi\rangle = \begin{pmatrix} \alpha \\ \beta \\ 0 \end{pmatrix} \tag{2.17}$$

and the probability of finding the particle in path a is

$$I_{001}: \quad \left|\alpha'\right|^2 = |\alpha|^2\ |U_{11}|^2 + |\beta|^2\ |U_{22}|^2 + \beta\alpha^* U_{12} U_{11}^* + \alpha\beta^* U_{11} U_{12}^*. \tag{2.18}$$

The same can be done for the other possible configurations. When each term is then inserted into the formula of the Sorkin parameter from equation 2.9, one obtains

$$\begin{aligned} \kappa &= I_{000} - I_{100} - I_{010} - I_{001} + I_{110} + I_{101} + I_{011} - I_{111} \\ &= |\alpha|^2 |U_{11}|^2 + |\beta|^2 |U_{22}| + \ldots - \ \gamma\beta^* U_{12}^* U_{13} \\ &= 0. \end{aligned} \tag{2.19}$$

As we have done this general calculation, it shows that for any single-photon state this always leads to only second-order interference terms as in equation 2.16. However, for other states with a larger photon-number, Rozema et al. have found that in specific setups higher-order interference can arise. The number of photons can even be not well-defined, as with coherent states (see section 2.2.2). One example given in Ref. [21] is a setup sketched in figure 2.12 with M paths and M nonlinear two-mode phase-shifters acting between the first path and each of the other paths. The first two paths interact by a 50:50 beam splitter eventually. When sending in coherent states as input states with an equal mean photon number of $\langle n \rangle$, the interference component can be expressed as ([21])

$$\mathcal{I}_M = \left| \langle n \rangle \left( \exp[-\langle n \rangle (1 - e^{-i\theta})] - 1 \right)^{M-2} \right| \cos(\varphi_2 - \varphi_1 - \delta), \tag{2.20}$$

with $\delta$ being a fringe offset and $\varphi_1$ and $\varphi_2$ a phase of the states in the first two paths. $\theta$ is a characteristic magnitude of the nonlinear phase-shifters $U_{ij}$. However, instead of going into detail, this equation is presented to show that, depending on the number of coupled paths, higher-order interference can arise. Furthermore, it was stated that

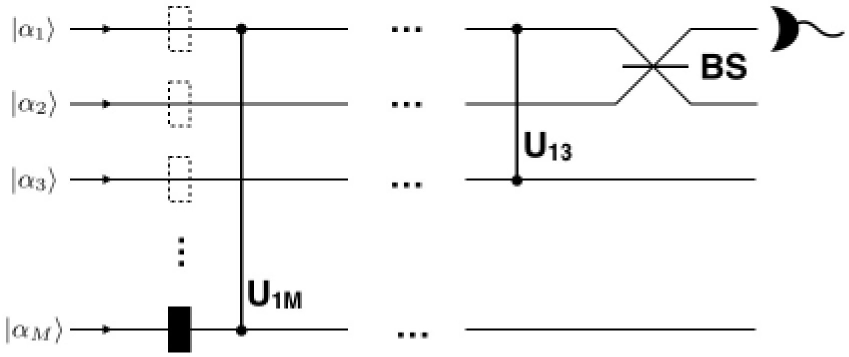

**Figure 2.12: Sketch of a set-up for measuring higher-order interference.** Coherent states $|\alpha_i\rangle$ are propagating along a path if not blocked and then going through a sequence of nonlinear phase shifters $U_{1M}, \ldots, U_{13}$. As a final element, a 50:50 beam splitter is put between the first two paths and the intensity is measured in the first path. The obtained interference is described by equation 2.20. (Taken from Ref. [21].)

for any system showing higher-order interference originating from nonlinear unitary interactions, a Hamiltonian nonlinear in its ladder operators $\hat{a}$ and $\hat{a}^\dagger$ is necessary. This leads to the assumptions that also with tools of nonlinear optics, higher-order interference should be detectable in a specific setup.

Inspired by this, we made use of a standard nonlinear crystal and three-photon processes to come up with a scheme where third-order interference should be present. The experiment is described in chapter 6.

### 2.2.2 Quantum Description of Nonlinear Optics and Coherent States

Since it was shown that nonlinear interactions can lead to higher-order interference, we started to look for common descriptions of nonlinear systems in quantum mechanics and to check for higher-order interference. We found an example by a system with three-photon processes in a nonlinear medium. While a detailed description is usually done within nonlinear optics as in chapter 3.1, the basic Hamiltonian gives rise to an accurate intuition. Basically, in a quantum picture of light a nonlinear medium allows the conversion of two photons into a third photon and vice versa under the conditions of energy and momentum conservation. A basic Hamiltonian describing second-order nonlinear three-photon processes is [9]

$$\hat{H} = \hbar\omega_a\ \hat{a}\hat{a}^\dagger + \hbar\omega_b\ \hat{b}\hat{b}^\dagger + \hbar\omega_c\ \hat{c}\hat{c}^\dagger + i\hbar\chi^{(2)}(\hat{a}\hat{b}\hat{c}^\dagger - \hat{a}^\dagger\hat{b}^\dagger\hat{c})\ . \tag{2.21}$$

Where the first three terms $\hbar\omega\hat{n}$, with $\hat{n} = \hat{a}^\dagger\hat{a}$ being the number operator, come from the fact, that a photon can be seen as a harmonic oscillator in the electromagnetic field with a certain energy $\hbar\omega$, and the last term brings in the nonlinear component. $\chi^{(2)}$ is the second-order susceptibility (see chapter 3.1) which can be seen as an indicator of the strength of the processes and the ladder operators $\hat{a}$ and $\hat{a}^\dagger$ give direct insight into the processes themselves. $\hat{a}$ is the annihilation operator for state a, which annihilates a photon from state a and $\hat{a}^\dagger$ is the creation operator that creates a photon in mode a. Assuming a number n of indistinguishable photons in a so-called Fock State $|n\rangle$, $\hat{a}$ and $\hat{a}^\dagger$ act as

$$\begin{aligned} \hat{a}\ |n\rangle &= \quad \sqrt{n} \quad |n-1\rangle \\ \hat{a}^\dagger\,|n\rangle &= \sqrt{n+1}\ \ |n+1\rangle\,. \end{aligned} \tag{2.22}$$

For calculations throughout this thesis, it should also be stated that the annihilation operator $\hat{a}$ acting on a vacuum state $|0\rangle$ destroys the vacuum state to number 0. The creation operator then is not creating a state anymore:

$$\begin{aligned} \hat{a}\,|0\rangle &= 0 \\ \hat{a}^\dagger 0\ &= 0. \end{aligned} \tag{2.23}$$

When now the nonlinear term in equation 2.21 is analyzed, it becomes clear that it describes two complementary processes: On the one hand, two particles in modes a and b can be annihilated to create a particle in mode c and on the other hand, a particle in mode c can be annihilated to create two particles in modes a and b. The first process is known as sum-frequency generation and the latter process as spontaneous parametric down-conversion or in a specific case as difference-frequency generation (see chapter 3.1). Whenever the nonlinear medium enables one process, the conditions for the other one are fulfilled as well. As we can see, this procedure provides a possibility to couple photons in three paths.

### 2.2.3 Sorkin Parameter in Nonlinear Optics

To find a realizable experiment, an implementation of equation 2.21 would be an obvious choice since the necessary components to realize the three-photon processes are well known and analyzed in nonlinear optics. A nonlinear description also adds more possibilities to go deeper in detail, since many geometrical aspects can be formulated in a straight forward way. We made use of a model derived in section 3.1.3 that results in three coupled differential equations, describing the behaviour of three fields interacting via $\chi^{(2)}$-processes. The equations are listed here and explained in detail throughout this thesis:

$$\frac{dA_1}{dz} = igA_3A_2^*e^{-i\Delta kz} \tag{2.24}$$

$$\frac{dA_2}{dz} = igA_3A_1^*e^{-i\Delta kz} \tag{2.25}$$

$$\frac{dA_3}{dz} = igA_1A_2e^{-i\Delta kz} \tag{2.26}$$

When an incident light beam is seen as an oscillating field, it can be described by its amplitude $A$ and an oscillating part. The amplitudes of three fields interacting by the processes described in the Hamiltonian in equation 2.21 are proportional to the number of photons in each light beam and also to the intensity of the three beams. The magnitude of each amplitude is therefore varying along a direction $z$ as the number of photons does, when they are converted within a nonlinear medium. Since in this work three beams are realized experimentally by laser light, they have a well-defined direction and known behaviour and they can be described in analogy to the experiment in figure 2.12 as three paths interacting by a nonlinear crystal.

The main point is that laser light can also be described as specific quantum states, so-called 'coherent states' as in section 3.3, and since we can make use of the nonlinear model in equations 2.24 - 2.26 to get more insight, the existence of third-order interference as defined in equation 2.11 was checked by this model. The material properties and wavelength-dependence of the process have first been ignored and it was just checked if the nonlinear coupling of the three paths allows for third-order interference. The tunable variable in this model is the relative intensity of the incident light beams. Choosing for instance two beams of the same frequency to be of intensity $I_{1,2} = 0.5\ (a.u.)$ and the third beam of intensity $I_3 = 0$ corresponds to term $I_{110}$ in equation 2.11 or $P_{110}$ from the triple-slit experiment from section 2.1.2. Due to convention, the beams will be called 'signal', 'idler' and 'pump'. The amplitude of beam 3 only increases if photons are generated via the $\chi^{(2)}$-process of sum-frequency generation. The result is plotted in figure 2.13 and shows clearly, how the intensity and therefore also the amplitude of the third beam (pump) increases. Due to energy conservation, signal and idler beam decrease simultaneously. This can be done similarly with the other necessary terms for obtaining the Sorkin parameter. A detailed discussion of these results is given in chapter 3.1. In figure 2.13 the obtained Sorkin parameter can be plotted over the propagation length along which the nonlinear processes are present. Here, the Sorkin parameter is assumed to be measured in the pump path, which has the role of the detector in figure 2.12 and the intensity of the non-blocked pump beam was taken equally to the other two beams as $I_3 = 0.5\ (a.u.)$. The result is shown in figure 2.14. It can be seen clearly that the configuration of three beams which are coupled by nonlinear interactions leads to a non-vanishing Sorkin parameter. This result gives a promising guideline to follow and to be realized experimentally. However, the resolution needed to detect third-order interference is unclear and the model must be adapted to simulate a more realistic scenario due to several effects which are ignored in this simple calculations.

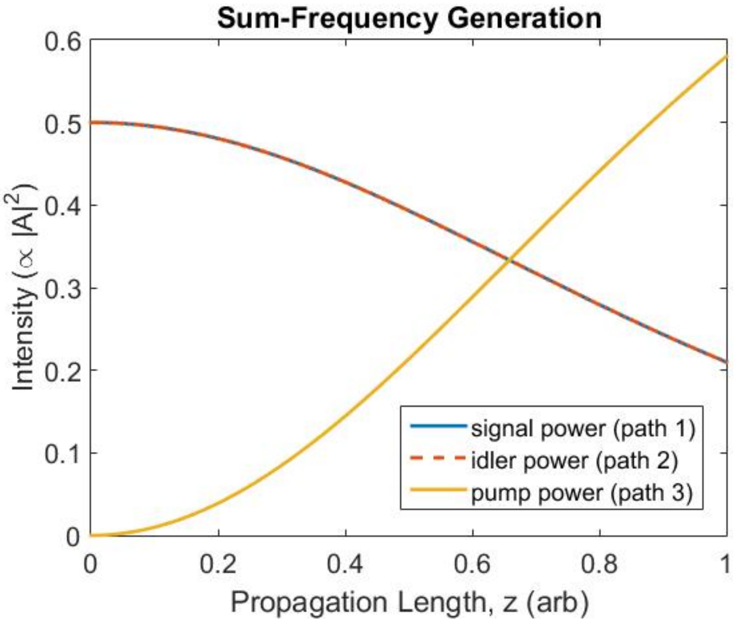

**Figure 2.13: The behaviour of the intensity-term $P_{110}$ in case of three light beams representing three defined paths.** It is identical to a basic sum-frequency generation scenario with two incoming beams generating a third one. Experimental imperfections have been ignored in this model.

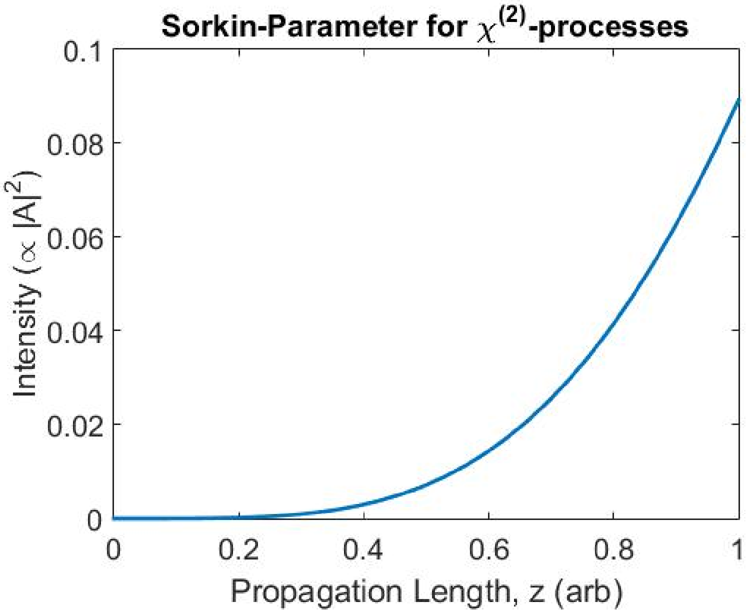

**Figure 2.14: The behaviour of the Sorkin parameter, representing third-order interference, in a scenario with equal input powers.** Determined by the model from the beginning of this section and determined via $\kappa = P_{ABC} - P_{AB} - P_{AC} - P_{PC} + P_A + P_B + P_C - P_0$. The presence of a non-vanishing Sorkin parameter over the length is clearly visible.

# 3 FOUNDATIONS

In this chapter we present the necessary foundations to understand and describe the physics behind our work in more detail. We start from nonlinear optics and show the well-known tools within this field that we use to build up a framework that allows for third-order interference. We gain a deeper understanding of the behaviour of the processes and components in our experiment, allowing us for a detailed theoretical description. We then show that interference and its reduction to only second-order terms is an idea that originates from classical physics and was already present in the classical interpretation of traditional interference experiments.

Furthermore, we show the foundations of quantum optics and the mathematical tools that we use to describe the system and get an approximation for the nonlinearity in the quantum optical description. By using quantum states, ladder operators and the Hamiltonian of the system, we obtain an intuition for our experiment in the quantum mechanical picture.

## 3.1 FOUNDATIONS OF NONLINEAR OPTICS

The processes of the interaction of photons in this experiment and their description can be described also within the field of Nonlinear Optics. To describe sum- and difference frequency generation and three-wave-mixing in general, we take a look at the behaviour of light in a so-called nonlinear medium:

### Polarization and Second Order Susceptibility

An electrical field of incident light **E** can induce an electrical dipole in a medium [22]. The dipole moment per unit volume is described by the polarization vector **P** and depends on the strength of the optical field. Usually, in a optical linear regime this can be described by the following approximation:

$$\mathbf{P}(t) = \epsilon_0 \chi^{(1)} \mathbf{E}(t) \tag{3.1}$$

Here, $\epsilon_0$ is the permittivity of vacuum and $\chi$ is the linear susceptibility, often just stated as susceptibility. However, in some materials nonlinear effects can be of significance when the magnitude of the electric field gets larger and larger, which can then be described by a nonlinear relation between the polarization **P** and the electric field **E**.

The intensity of those processes depends on the medium and the magnitude of the incident optical field. The polarization can then be described by the expansion

$$\begin{aligned}\mathbf{P}(t) &= \epsilon_0 \left[\, \chi^{(1)}\mathbf{E}(t) + \chi^{(2)}\mathbf{E}^2(t) + \chi^{(3)}\mathbf{E}^3(t) + \dots \,\right] && (3.2)\\ &= \mathbf{P}_0(t) + \mathbf{P}_{NL}(t) \text{ [4]}. && (3.3)\end{aligned}$$

$\mathbf{P}_0$ here represents the linear polarization from eq. 3.1 and $\mathbf{P}_{NL}$ combines the nonlinear terms. $\chi^{(2)}$ and $\chi^{(3)}$ are known as 'second- and third order nonlinear susceptibilities' and so on for higher-order terms.

In general, the susceptibility of order k is a (k+1)-order tensor. E.g., $\chi^{(2)}$ is a tensor of third order and will only be non-vanishing in the case of non-isotropic materials [4]. In this work we will mainly focus on processes depending on the $\chi^{(2)}$ susceptibility of a medium and neglect higher-order terms. For any class of crystal, the second-order susceptibility and further the characteristics of the crystal according to sum- and frequency generation processes (see chapter 3.1.3) can be described by equation 3.4, where the second-order susceptibility is described by a 3 x 6 Matrix[4].

$$\begin{bmatrix} P_x \\ P_y \\ P_c \end{bmatrix} = 2\epsilon_0 \underbrace{\begin{bmatrix} d_{11} & d_{12} & d_{13} & d_{14} & d_{15} & d_{16} \\ d_{21} & d_{22} & d_{23} & d_{24} & d_{25} & d_{26} \\ d_{31} & d_{32} & d_{33} & d_{34} & d_{35} & d_{36} \end{bmatrix}}_{\hat{d}} \begin{bmatrix} E_x^2 \\ E_y^2 \\ E_z^2 \\ 2E_yE_z \\ 2E_xE_z \\ 2E_xE_y \end{bmatrix} \tag{3.4}$$

The previously mentioned processes of sum- and difference-frequency generation and the role of the susceptibility are described in section 3.1.3.

### 3.1.1 Second-Order Susceptibility in Nonlinear crystal

In our case, a LBO-crystal with the chemical sum-formula of $LiB_3O_5$ is used. The crystal is an orthorhombic crystal of crystal class mm2 which means that, due to specific symmetries, various entries from the susceptibility written as matrix form in equation 3.4 vanish [4]. Specifically for a LBO-crystal used in this experiment, it reduces to [12]

$$\hat{d} = \begin{bmatrix} 0 & 0 & 0 & 0 & 0 & 0 \\ 0 & 0 & 0 & 0 & 0 & 0 \\ 1.05 & -0.98 & 0.05 & 0 & 0 & 0 \end{bmatrix}. \tag{3.5}$$

Since the nonlinear response of the polarization to a electromagnetic wave is only of significance if the intensity is high enough, the resulting effects are usually exploited with impinging powerful laser light. Depending on the relative orientation of the crystal axes to the incoming beam, the effective nonlinear coefficient $d_{eff}$ is resulting from corresponding entries in the previously shown matrix. A concrete evaluation of $d_{eff}$ is given in section 3.1.3.

### 3.1.2 Wave equation for light in nonlinear media

To describe the propagation of light in nonlinear media, a wave equation can be derived by starting at the Maxwell's equations.
The Maxwell's equations for isotropic media without free charges and currents have the form

$$\begin{aligned} \nabla \cdot \mathbf{D} &= 0 \\ \nabla \cdot \mathbf{B} &= 0 \\ \nabla \times \mathbf{E} &= -\frac{\partial \mathbf{B}}{\partial t} \\ \nabla \times \mathbf{H} &= \frac{\partial \mathbf{D}}{\partial t} \end{aligned} \tag{3.6}$$

where **D** is the electric displacement field, which can again be decomposed in its linear and nonlinear part:

$$\mathbf{D} = \epsilon_0 \mathbf{E} + \mathbf{P} \tag{3.7}$$

$$= \mathbf{D}^{(1)} + \mathbf{P}_{NL} \tag{3.8}$$

From equations 3.6 and 3.7 where $D^{(1)} = \epsilon_0 \mathbf{E} + \mathbf{P_0}$ the wave equation for light propagation in lossless, non-dissipative nonlinear media can be derived and has the form ([4])

$$\nabla^2 \mathbf{E} - \frac{n^2}{c_0^2} \frac{\partial^2 \mathbf{E}}{\partial t^2} = \frac{1}{\epsilon_0 c_0^2} \frac{\partial^2 \mathbf{P}_{NL}}{\partial t^2} \tag{3.9}$$

where $c_0$ is the speed of light in vacuum and $n$ is the refractive index of the nonlinear medium. To gain insights into the generation of new frequencies, one can rewrite it as in equations 3.10 and 3.11.

$$\nabla^2 \mathbf{E} - \frac{1}{c^2} \frac{\partial^2 \mathbf{E}}{\partial t^2} = -\mathbf{S} \tag{3.10}$$

$$\mathbf{S} = -\frac{1}{\epsilon_0 c_0^2} \frac{\partial^2 \mathbf{P}_{NL}}{\partial t^2} \tag{3.11}$$

This has the form of a wave equation with a source term **S** that is caused by the incident wave **E** [22]. One method to find a solution for this nonlinear differential equation is the so-called Born approximation:
It is assumed that an incident field $\mathbf{E_0}$ causes the source term $\mathbf{S_0}$ which then emits the field $E_1$. This would then create a source $\mathbf{S_1}$ that emits $\mathbf{E_2}$ and so forth. In our case it is sufficient to go up to $E_1$ which is known as the first Born approximation [22]. According

to this approximation, the incident field causes the source $\mathbf{S_0}$ to emit $\mathbf{E_1}$ which shares the same spectral components with $\mathbf{P_{NL}}$ as shown in equation 3.10. When reducing $\mathbf{P}_{NL}$ to second-order, meaning

$$\mathbf{P}_{NL} = \epsilon_0 \chi^{(2)} \mathbf{E}^2(t), \tag{3.12}$$

with incident light described by the complex field $\mathbf{E_C}$ and the identities

$$\mathbf{E}(t) = Re\{\mathbf{E}_C(\omega) exp(i\omega t)\} = \frac{1}{2}[\mathbf{E}_C(\omega) exp(i\omega t) + \mathbf{E}_C^*(\omega) exp(-i\omega t)] \tag{3.13}$$

the polarization can be expressed as

$$\mathbf{P}_{NL} = \frac{1}{2}\epsilon_0 \chi^{(2)} \mathbf{E}_C(\omega)\mathbf{E}_C^*(\omega) + Re\{\frac{1}{2}\epsilon_0 \chi^{(2)} \mathbf{E}_C^2(\omega) exp(i2\omega t)\} \tag{3.14}$$

$$= \frac{1}{2}\epsilon_0 \chi^{(2)} \mathbf{E}_C(\omega)\mathbf{E}_C^*(\omega) + Re\{\mathbf{P}_{NL,C}(2\omega) exp(i2\omega t)\}\ . \tag{3.15}$$

The nonlinear polarization and therefore the source term $S_0$ has a component at frequency $2\omega$, meaning that the emitted field contains a component at twice the frequency of the incident field. Assuming that the incident field only consists of a monochromatic frequency $\omega$ and the outcome field has the frequency $2\omega$, the process is known as Second-Harmonic generation, a special case of so-called Sum-Frequency Generation. Due to convenience it is usually seen within an energy level picture as explained in section 3.1.3. To exploit these processes efficiently, a suitable phase-matching has to be achieved as described in section 3.1.5.

### 3.1.3 Sum-Frequency Generation

One phenomenon of interaction of light in media based on the second-order susceptibility $\chi^{(2)}$ is the previously mentioned ‘Sum-frequency Generation’. Its principle is sketched in figure 3.1: Two incident light beams with angular frequency $\omega_1$ and $\omega_2$ impinge onto a nonlinear medium. Part of the incident beams is then converted into a beam with angular frequency $\omega_3 = \omega_1 + \omega_2$. In a quantum mechanical picture it can be

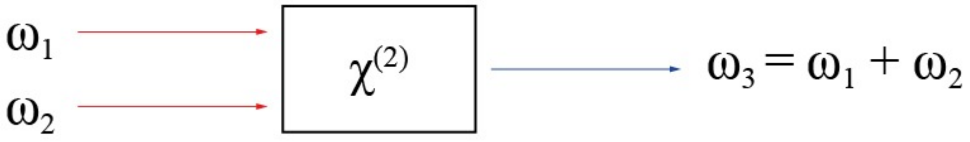

**Figure 3.1: Principle of sum-frequency generation.** Two incoming beams with $\omega_1$ and $\omega_2$ and a $\chi^{(2)}$-medium gives rise to the generation of a beam with $\omega_3 = \omega_1 + \omega_2$.

seen as two incoming photons with frequency $\omega_1$ and $\omega_2$ being converted to a photon of frequency $\omega_3$ as shown schematically in figure 3.1.

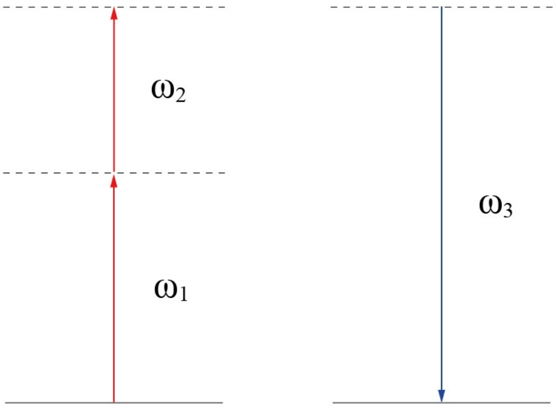

**Figure 3.2: Energy level description of a sum-frequency generation according to figure 3.1.**

In the special case of $\omega_1 = \omega_2$ meaning that the two photons are, for instance, originating from the same monochromatic beam, the process is known as 'second-harmonic generation'. More on that is described in chapter 6.
To describe this conversion of light beams and their interaction via this phenomenon, we take a closer look at the mathematical description. Equation 3.9 must be valid for each field component propagating in the medium and therefore also describes the generated beam with angular frequency $\omega_3$ from fundamental beams with $\omega_1$ and $\omega_2$. A solution for the wave equation considering a nonlinear polarization term up to the second order has the form

$$E(z,t) = A_3 e^{i(k_3 z - \omega_3 t)} + c.c.\ . \tag{3.16}$$

Here, z is the direction of propagation of the generated beam and $k_3 = \frac{n_3}{c_0}\omega_3$. Since the nonlinear source term is not too large, the amplitude factor in equation 3.16 is expected to be a slowly varying function of z. Physically this can be interpreted as a field growing along the crystal or in the quantum mechanical picture as more and more generated photons along z. For a fixed polarization direction of the light and fixed direction relative to the crystal, the nonlinear polarization term for sum-frequency generation is given by (see [4])

$$P(\omega_3) = 4\epsilon_0 d_{eff} E(\omega_1) E(\omega 2) \tag{3.17}$$

or for second-harmonic generation in the case of $\omega_1 = \omega_2$, respectively,

$$P(\omega_3) = 2\epsilon_0 d_{eff} E(\omega)^2. \tag{3.18}$$

As mentioned above, a good phase-matching configuration has to be achieved. To do so, we use the technique of 'angle tuning', which is based on birefringence in nonlinear crystals. This is described in more detail in section 3.1.6.

The corresponding value of $d_{eff}$ depends on the polarization of light and incident direction relative to the orientation of the birefringent crystal (see section 3.1.6). We assume, that the incident light beams have a polarization along the so-called ordinary axes of the crystal and the generated light is polarized along the extraordinary axis. Closer insight on this is given in chapter 3.1.5. In the case of the crystals used in this experiment, $d_{eff}$ can be determined by ([12])

$$d_{eff} = d_{32} cos\phi. \tag{3.19}$$

If both incident beams are assumed to be plane waves as reported in equation 3.16 and equations 3.16 and 3.17 are inserted into equation 3.11, the following differential equation can be derived, where the 'wave vector mismatch' $\Delta k$ is described by $\Delta k = k_1 + k_2 - k_3$:

$$\frac{d^2 A_3}{dz^2} + 2ik_3 \frac{dA_3}{dz} = \frac{-4 d_{eff} \omega_3^2}{dz} A_1 A_2 e^{i\Delta kz} \tag{3.20}$$

Usually, the amplitude $A_3$ can be assumed to vary much slower than a fraction of unity over a length equal to the wavelength of the propagating electromagnetic wave. Therefore the first term on the left side is negligible compared to the second term. This is also known as the slowly varying amplitude approximation [4]. The corresponding mathematical condition is:

$$\left| \frac{d^2 A_3}{dz^2} \right| \ll \left| k_3 \frac{dA_3}{dz} \right| \tag{3.21}$$

Assuming a slowly varying amplitude, equation 3.20 can be reduced to

$$\frac{dA_3}{dz} = \frac{2i d_{eff} \omega_3^2}{k_3 c^2} A_1 A_2 e^{i\Delta kz}. \tag{3.22}$$

Equation 3.22 shows how the amplitude of the generated field depends on the intensity and the frequency of the incoming beams and characteristics and orientation of the crystal. Equation 3.22 refers to the so-called undepleted pump approximation, where it is assumed the amplitudes A1 and A2 stay constant during the propagation within the crystal. In the case of a strong nonlinear interaction this does not hold anymore and one should consider the intensity of the incoming beams to decrease along the crystal. Moreover, after the sum-frequency generation, all three beams interact with each other. At that point, phenomena known as difference-frequency generation can take place as well during the nonlinear propagation of the 3 beams (See chapter 3.1.4). By doing the same derivation as above for the optical waves at frequencies $\omega_1$ and $\omega_2$, two additional coupled differential equations are obtained, describing how the two incoming beams behave along the crystal.

$$\frac{dA_1}{dz} = \frac{2id_{eff}\omega_1^2}{k_1c^2} A_3A_2^* \; e^{-i\Delta kz} \tag{3.23}$$

$$\frac{dA_2}{dz} = \frac{2id_{eff}\omega_2^2}{k_2c^2} A_3A_1^* \; e^{-i\Delta kz} \tag{3.24}$$

This model includes the assumptions of having a lossless medium, collinear propagation of the beams and a symmetry that gives the same $d_{eff}$-value in all three equations.

### 3.1.4 Difference-Frequency generation

As mentioned above, three-wave mixing describes the interaction of three electromagnetic waves propagating through a nonlinear medium with a non-vanishing second-order nonlinearity. The inverse process of sum-frequency generation is called 'difference-frequency' generation. It is another second-order nonlinear effect and is sketched in terms of energy in figure 3.3:

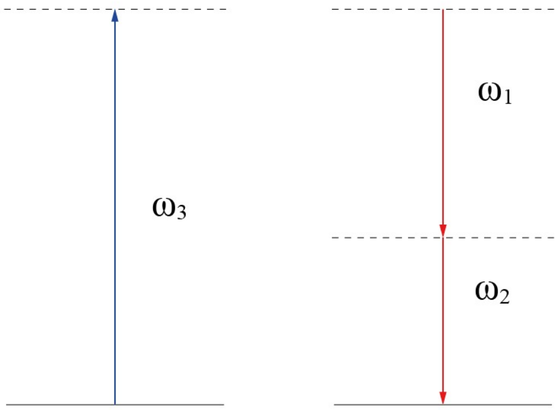

**Figure 3.3: Energy level description of a difference-frequency generation process.** Here, two photons of energy $\omega_3$ and $\omega_1$ create a photon of energy $\omega_2 = \omega_3 - \omega_1$. A generation of $\omega_1$ via $\omega_3 - \omega_2$ is also possible.

The beam with angular frequency $\omega_3 > \omega_{1,2}$ interacts with the beam of $\omega_1$ in a way, that light in the third beam with $\omega_2 = \omega_3 - \omega_1$ is generated. It should be noted that this process satisfies the same phase-matching condition of the inverse process, sum-frequency generation, where $\omega_3 = \omega_1 + \omega_2$. In general, providing the phase matching and spatial and temporal overlap, the three beams interact with each other by means of DFG and SFG while propagating through the nonlinear medium, known as 'Three-Wave

Mixing'.
A graphical evaluation of three-wave mixing and the coupled wave equations 3.22 - 3.24 is carried out in chapter 4.1.1.

### 3.1.5 Phase Matching

To see how the wave vector mismatch $\Delta k$ effects the outcome intensity in the undepleted approximation, where $A_1$ and $A_2$ are taken to be constant along the crystal, one needs to integrate equation 3.22 over the length $L$ of the crystal.

$$\begin{aligned} A_3(L) &= \frac{2id_{eff}\omega_3^2 A_1 A_2}{k_3 c^2} \int_0^L e^{i\Delta kz} dz \\ &= \frac{2id_{eff}\omega_3^2 A_1 A_2}{k_3 c^2} (\frac{e^{i\Delta kL}}{i\Delta k}) \end{aligned} \tag{3.25}$$

The intensity of the resulting field is proportional to the time-averaged Poynting vector and gives ([22]) a dependence of

$$I \propto |A_3|^2 \tag{3.26}$$

When equation 3.25 is inserted into equation 3.26 a resulting dependence is yielded as

$$I_3 \propto sinc^2(\frac{\Delta kL}{2}) \ . \tag{3.27}$$

The importance of $\Delta k$ can be obtained when looking at the derived relation by plotting the $sinc^2$-function from (3.27) versus its argument as in figure 3.4. It is evident, in order to gain the highest intensity of the outcome generated wave in a sum-frequency

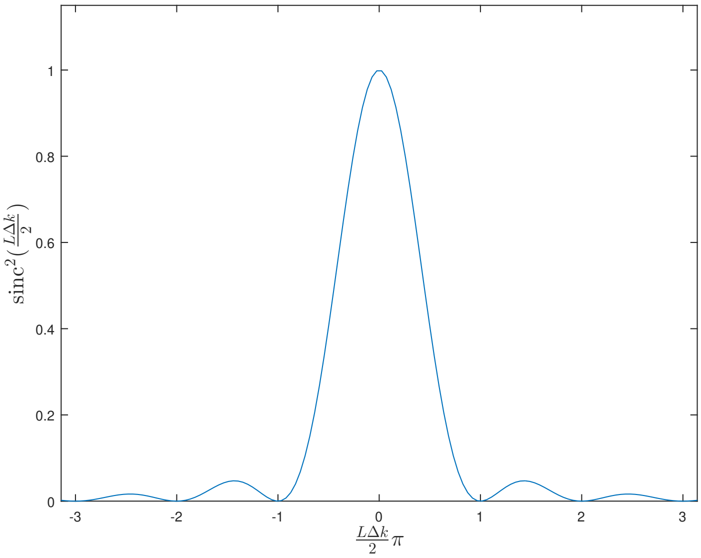

**Figure 3.4: Dependence of the intensity of the sum-frequency generation from equation 3.27 on the wave vector mismatch $\Delta k$.**

generation process the wave vector mismatch should vanish so that $\Delta k = 0$. The larger the wave vector mismatch $\Delta k$, the lower the intensity of the generated beam will be. Equation 3.27 is derived under the assumption that the conversion efficiency is only a very small fraction compared to the input beams and that the input amplitudes remain the same. This approximation is called the undepleted approximation, meaning that only a small part of the input beams is converted and we can assume that their intensity is not affected by the nonlinear interaction. In our experiment, this assumption is not valid anymore. However, the dependence of the conversion efficiency on the wave vector mismatch is similar to what is shown in figure 3.4 [4], in particular the perfect condition when $\Delta k = 0$ and the dramatical decrease with a slightly larger mismatch.

### *Phase matching and the dispersive refractive index*

From the previous section it could be seen that the most efficient generation of sum-frequency happens in the case of

$$\Delta k = k_3 - (k_1 + k_2) = 0 \tag{3.28}$$

When inserting the relation $k = \frac{n(\omega)\omega}{c_0}$ the condition can be written as

$$\frac{n(\omega_1)\omega_1}{c_0} + \frac{n(\omega_2)\omega_2}{c_0} = \frac{n(\omega_3)\omega_3}{c_0}. \tag{3.29}$$

However, materials in general have a finite dispersion [4]. The refractive index $n(\omega)$ of the material is then a function of frequency which usually increases with $\omega$ [4]. As a consequence, equation 3.29 can not be satisfied when $\omega_1 + \omega_2 = \omega_3$ and $n(\omega_1) < n(\omega_2) < n(\omega_3)$.

There are various techniques of getting a perfect phase-matching within experimental constraints. One possibility is to make use of the birefringent characteristics of the nonlinear crystal. This technique is used in our experiment. It is described in detail in chapter 3.1.6.

### 3.1.6 Birefringence in a Nonlinear Crystal

In the case of equation 3.29 an efficient exploitation of the nonlinear processes can only be obtained if the refractive indices of the involved beams are equal which can not be achieved without further processing due to dispersion, as described previously. One technique to achieve equal refractive indices in a birefringent crystal is the so-called 'Angular Tuning'. To describe the phase matching technique of angular tuning, we first look at the refractive index of a nonlinear crystal.

#### *Uniaxial Crystals*

The simplest case is a so-called uniaxial crystal: It is defined by an optic axis, also known as z axis of the crystal [4]. If the incoming beam is polarized perpendicular to the optic axis, it experiences the ordinary refractive index $n_o$, for instance if the beam propagates parallel to the optical axis. This is sufficient but not necessary: For any other propagation direction there is a linear polarization that is also oriented perpendicular to the optic axis and this beam experiences the ordinary refractive index $n_o$ as well. A beam that experiences $n_o$ is known as ordinary ray. For any other beam with an angle $\theta$ between the propagation direction and the optic axis, the polarization can be decomposed into two modes where one experiences $n_o$ and the other one experiences a different, direction-dependent refractive index $n(\theta)$ which depends on the angle $\theta$ between **k** and the z-axis as in equation 3.30. This mode is called the extraordinary ray [22].

$$\frac{1}{n(\theta)^2} = \frac{sin^2(\theta)}{n_e^2} + \frac{cos^2(\theta)}{n_o^2} \tag{3.30}$$

In the case of $\theta = 90°$ the beam propagation is governed by the extraordinary refractive index $n_e$. In the experiment here reported, the polarization of the generated beam is orthogonal compared to the incoming beams. This process is known as type-I Sum-Frequency Generation [19]. To get an efficient nonlinear process, the crystal has to be oriented so that the beams meet the refractive indices in a way that $\Delta k = 0$. In a so-called positive uniaxial crystal, $n_e > n_o$ leading to the conclusion that the generated beam with the frequency $2\omega$ should face the ordinary index and the incoming waves to face an extraordinary index so that $n_e(\omega, \theta) = n_o(2\omega)$ which is adjusted by the angle $\theta$, as demonstrated in figure 3.5. This shows, that by changing the orientation of the crystal relative to the incoming beams, optimal phase-matching can be achieved. In our experiment we tune the orientation of a LBO-crystal which is a positive biaxial crystal [12].

### *Index Ellipse*

The concept of the different refractive indices of a uniaxial birefringent crystal can be visualized by the index ellipse as shown in figure 3.5. In the case for example of type-I second harmonic generation (particular case of sum-frequency generation), assuming a positive uniaxial crystal, meaning $n_e > n_o$, the polarization scheme is e-e-o: When the fundamental beam with $\omega$ is polarized extraordinarily, there is one angle $\theta$ where an intersection of the refractive index of $2\omega$ and $\omega$ is present, which is then the refractive index experienced by both beams and therefore the perfect phase matching condition from equation 3.29 is fulfilled.

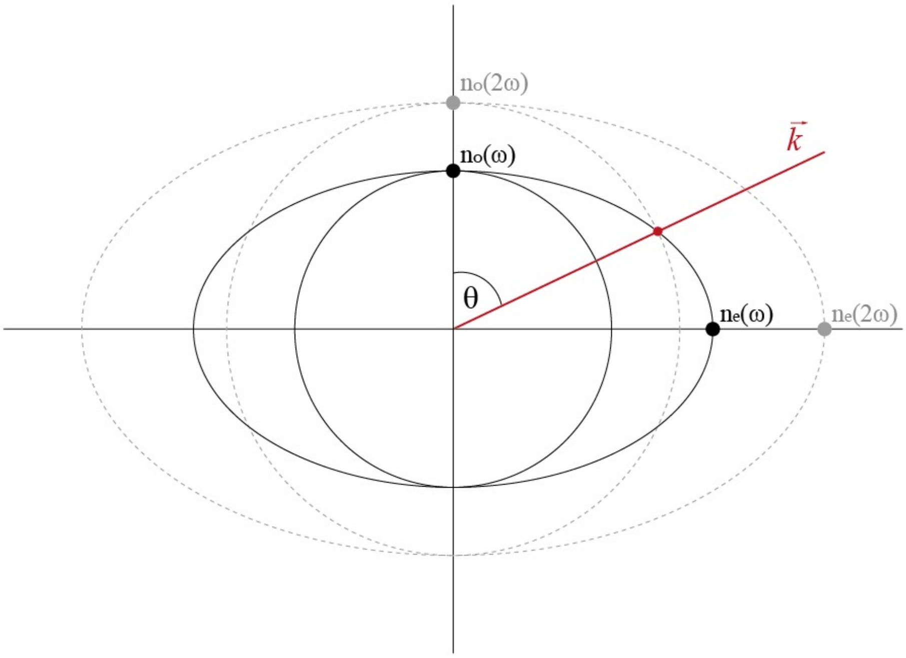

**Figure 3.5: Index ellipse for a positive uniaxial crystal.** The extraordinary index for a given frequency is bigger then the ordinary index. Therefore the polarization of the generated beam is ordinary and the fundamental one extraordinary. For a given frequency and a given angle $\theta$ between the wave vector and the ordinary axis, a common refractive index for the ordinary and the extraordinary beam can be found.

### *Biaxial Crystals*

In a biaxial crystal, the optical system is characterized by three refractive indexes. When the principle axes and their corresponding refractive indexes $n_1$, $n_2$ and $n_3$ are drawn as in figure 3.6, the so-called index ellipsoid is obtained. By inserting **k** of the propagating wave and drawing a plain perpendicular to it and through the origin, one can determine the refractive indices $n_a$ and $n_b$. By recalling that at higher frequencies for typical nonlinear effects the refractive index increases, a beam with frequency $2\omega$ would then correspond to a slightly bigger ellipsoid. By changing the orientation, a common refractive index can be obtained for the fundamental and the generated beam.

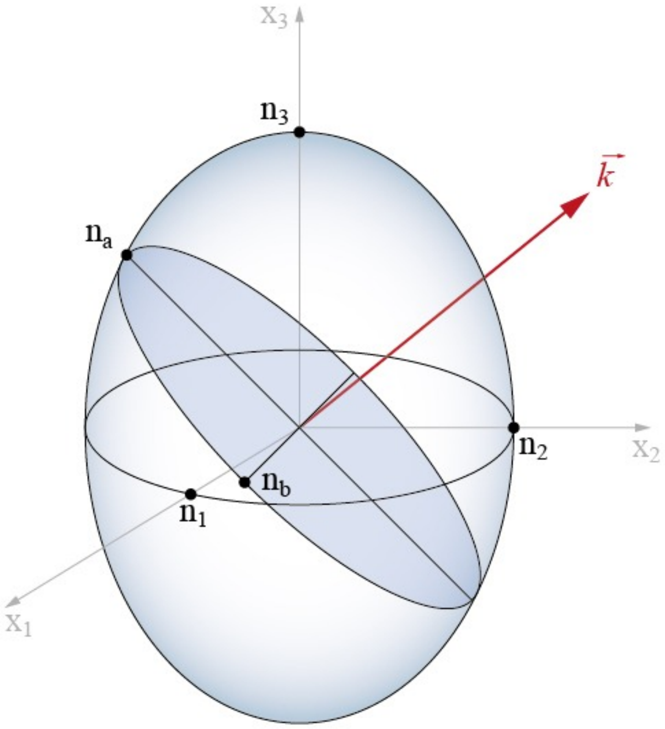

**Figure 3.6: Indexellipsoid to determine characteristic refractive indices for incoming wave with wave vector k.**

The fact that different refractive indexes are present, gives rise to perfect phase matching experimentally by changing the orientation of the crystal in analogy to section 3.1.6.

### 3.1.7 Walk-Off Effects

#### *Spatial Walk-Off*

The main limiting factor for obtaining efficient nonlinear optical generation over the whole length of a crystal is that the three waves do not propagate collinearly to each other within the crystal when phase matching based on birefringence is exploited. Therefore, only across a specific length within the crystal, second-order nonlinear processes can occur. The angle between the beams is known as the 'walk-off angle' [11] and is a direct consequence of the birefringence of nonlinear crystals and the polarizations of the beams: When a type-I SHG process with an ordinarily polarized fundamental beam is assumed, the generated beam has an extraordinary polarization.
Typically, the direction of the orientation of the wave fronts of a beam, which is indicated by the direction of the wave vector **k** is identical with the direction of the Poynting Vector **S** [22] defined as

$$\mathbf{S} = \mathbf{E} \times \mathbf{B}, \tag{3.31}$$

which describes the propagation of the energy of a beam. The wave vector **k** is normal to the electric displacement field **D**. Assuming an isotropic, nondispersive material, the electric displacement field can be written as $\mathbf{D} = \epsilon \mathbf{E}$ with $\epsilon$ being a scalar value and therefore independent of the direction within the material [22]. However, in non-isotropic materials $\epsilon$ is a tensor that can cause a difference between the direction of **E** and **D** of the beam. In an anisotropic displacement the wave fronts are then generally not oriented normally to the propagation direction, but can be tilted as seen in figure 3.8 [22]. The wave vectors of the fundamental and the generated beam then still overlap, but the Poynting vectors then differ by the walk-off angle $\rho$. This angle is described by

$$\tan \rho = -\frac{1}{n(\theta)} \frac{\partial n(\theta)}{\partial \theta} \tag{3.32}$$

showing the dependence on the extraordinary refractive index $n(\theta)$ [25]. As described in chapter 3.1.6, the walk-off only affects the extraordinary beam due to the dependence of $n(\theta)$ on $\theta$. The angle $\rho$ is normally given in mrad and lies within the range of a few mrad for the most crystals [11].

Effective three-wave mixing only happens as long the beams overlap spatially, which is then limited by the walk-off angle and the diameter of the beam. Since a smaller diameter means higher intensity per area, nonlinear effects can be enhanced by tightening the beam waist. However, then the spatial walk-off becomes even more crucial. This means, it is an interplay of walk-off and beam waist which is referred to in chapter 4 in more detail. It now becomes clear, why a an oscillating nonlinear generation behaviour as predicted by the simple model along the crystal as in chapter 4.1.1 is experimentally not observable as stringent limiting factors play an important role. The model of the three coupled-wave equations is only valid for a very small distance and ideal conditions within the crystal.

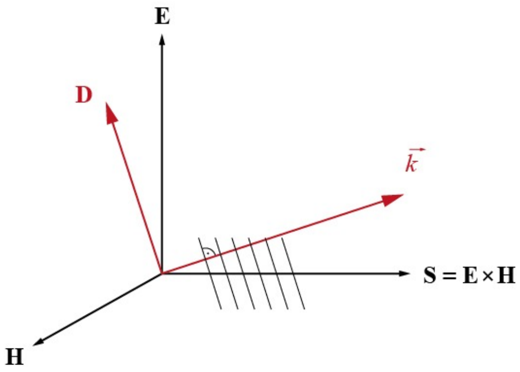

**Figure 3.7: Possible geometrical arrangement of the Poynting vector and the wave vector.** The direction of the electromagnetic wave, represented by the Poynting vector **S**, can differ from the direction of the energy flow represented by **k**, when **D** points towards a different direction than **E**. The wave fronts are indicated here by the grey colored lines oriented normally to **k**.

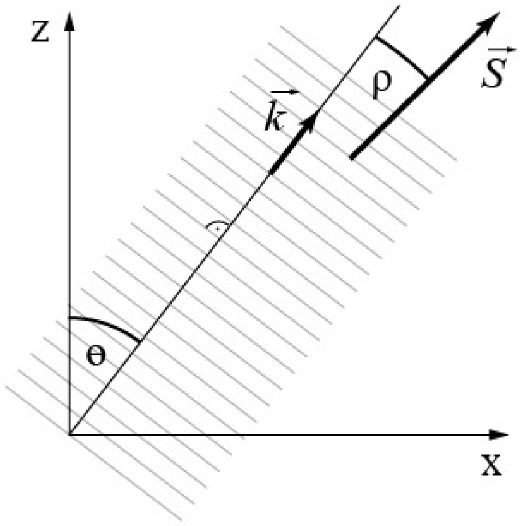

**Figure 3.8: Different alignment of the Poynting vector and the wave vector.** In a birefringent crystal the direction of the beam propagation, represented by the Poynting vector **S**, and the orientation of the wave fronts, represented by the wave vector **k**, do not have to overlap.

### *Temporal Walk-Off*

Spatial Walk-Off is not the only effect that limits the efficiency of the nonlinear processes. As mentioned before, $\chi^{(2)}$ of a medium is very much smaller than the first-order susceptibility and nonlinear effects usually only become significant when the intensity of the incoming beams is high enough. To gain high input intensities, usually pulsed laser light is used. As a consequence, not only the incident beam is pulsed, but also the generated one. When light propagates within media, the enveloping shape of the wave propagates with a different velocity than the phase fronts. While the phase fronts move with the phase velocity $v_p = \frac{\omega}{k}$ the beam envelope propagates with the group velocity

$$v_g = \frac{d\omega}{dk}. \tag{3.33}$$

The derivative term in equation 3.33 demonstrates that a dispersive medium leads to a different group velocity of the two frequency components and therefore a spatial separation along the propagation direction. In the case of a non dispersive medium, such as air, $\omega = c \cdot k$ and the phase velocity equals the group velocity. A more insightful description is given in section 4.1.1.

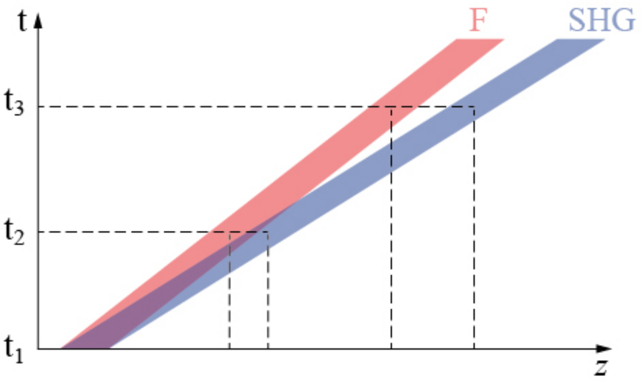

**Figure 3.9: Temporal walk-off effect.** Different frequency components face different refractive indexes within a dispersive material and therefore the fundamental and generated beam propagate with different velocities within the crystal. The common point of the dashed lines represent the center of the gaussian intensity distributions of the beams. It can be seen how the maxima separate in space over time. At $t_1$ the beams are overlapping while at $t_2$ a separation can be already be noticed. At $t_3$ the beams have separated clearly.

As seen in figure 3.9, the two pulses separate along the crystal due to different velocities. This effect is known as ‘Temporal Walk-Off’. Since for obtaining a nonlinear process, the beams have to overlap, both walk-off effects have to be considered in an experiment with pulsed laser light.

In addition, treating the pulses as single frequency pulses is just an approximation. In fact, a pulsed beam consists of different frequency components close to each other. Every frequency component of the pulse can be associated with a slightly different refractive index and therefore velocity, meaning that in reality also the pulses are broadening along the crystal. This is known as ‘Group Velocity Dispersion’. However, in common ones experiments this is typically negligibly small (see [11]) and is not taken into account in this work.

### 3.1.8 Pulsed Laser Light

To increase the power of the input light, special techniques in laser physics have to be applied. Since nonlinear optical processes need high powers, continuous wave (CW) light is not sufficient. CW light exits a laser with continuous power and is created by standard atomic processes in the medium within the cavity of a laser. Since this is not of special interest for this thesis, this is only explained briefly but can be looked up in any book about laser physics [10]. Usually, coherent light is being generated and reflected back and forth within the cavity and transmitted by the output coupler with a certain probability. This leads to a continuous generation and output of laser light. The technique to create pulses of laser light shorter than nanoseconds is called modelocking. It has the advantage that pulses of higher and higher intensities are built up inside the cavity and are transmitted through the output coupler. This happens via a intensity dependent optical component, in the case of our laser it is a Kerr lens. This focuses the light that has reached an intensity threshold onto a slit that is aligned to match the focal point spatially. With this procedure, only light with high intensities forms a stable mode in the cavity. This is a pulsed mode. A sketch of the envelope of the power of a pulsed beam can be seen in figure 6.5.

### 3.1.9 Geometrical Arrangements of Sum- and Difference-Frequency Generation

By making use of the conservation of momentum, interesting geometrical arrangements can be realized when working with three-photon processes. In the case of sum-frequency generation of two photons with collinear wave vectors as, for instance, present in second-harmonic generation, the generated photon will also propagate in the same direction. The walk-off angle is neglected here but technically it would be present, similar to figure 3.1. However, when the two incoming photons are tilted with respect to each other, momentum conservation leads to a situation as in figure 3.10.

When the two incoming beams share a common angle with reference to an axis normally to the surface of the medium, the generated photons propagate along this axis. While

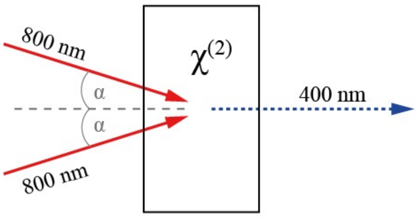

**Figure 3.10: Intuitive arrangement of SFG.** In the sketched situation the two incoming beams with $\lambda = 800$ nm have the same incident angle $\alpha$ with an axis normally to the medium surface. This geometry leads to generated photons propagating normally to the surface due to the sum of the two wave vectors and therefore a cancelling out-situation of the income angles.

this is a more or less intuitive picture, the situation even gets more interesting in the case of difference-frequency generation where the phase matching condition and the wave-vector behaviour can be expressed as $k_3 - k_1 = k_2$ when the photon with $k_2$ is generated and vice versa when $k_1$ being generated. This leads to the generation of photons along a direction symmetrical to the income direction. The two geometries in figure 3.3 represent this phenomenon and are used in the experiment as described in chapter 6. It should be noted, as mentioned above, that the extraordinary beam still faces spatial walk off as described in section 3.1.7. However, since the walk-off angle is smaller then the incident angles in our setup and due to simplicity, this was neglected in this description.

(a)

(b)

**Figure 3.11: Possible arrangements for DFG.** In the case of difference-frequency generation the wave vectors of the incoming beams get subtracted as in $k_3 - k_1 = k_2$. This leads to a counter-intuitive situation: Generated photons propagate along a direction with the same angle to the incident axis symmetrically to the incoming beam with higher wavelength. (a) the upper photon is being generated. (b) The lower photon is being generated.

## 3.2 INTERFERENCE

Interference is a phenomenon present in every common wave theory. It appears as soon as two waves interact according to the superposition principle. In classical mechanics, it is well-known that two waves with the same frequency and the same phase interfere constructively and two waves with the same frequency and a path difference of $\Delta d = n\frac{\lambda}{2}$, where n is any integer number, interfere destructively.

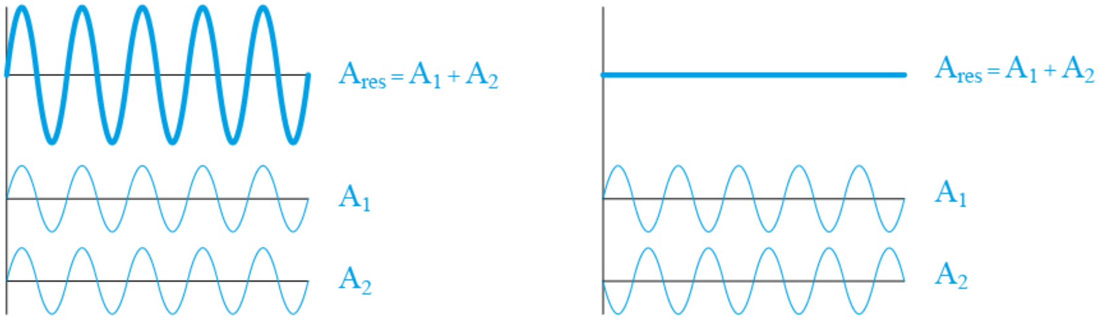

**(a)** Constructive Interference

**(b)** Destructive Interference

**Figure 3.12: Two waves with the same frequency $\nu$ interfere according to the superposition principle.** In (**a**) the path difference of the waves equals zero or a multiple of the wavelength and in (**b**) the path difference is a multiple of half the wavelength, $d = n\frac{1}{2}\lambda$.

In figure 3.12 (**a**) two waves with the same angular frequency $\omega$, amplitude $A$ and no path difference interfere constructively. In 3.12 (**b**) the waves interfere with a path difference of $\Delta d = \frac{1}{2}\lambda$ which results in a phase difference of $\phi = \frac{1}{2}\pi$ and lead to destructive interference. In general two waves with the same amplitude, the same frequency and a specific path difference can be described as

$$A_1(x,t) = A_0 \sin\left(kx - \omega t + \phi_1\right) \tag{3.34}$$
$$A_2(x,t) = A_0 \sin\left(kx - \omega t + \phi_2\right) \tag{3.35}$$

Since the resulting wave is described by $A_{res}(x,t) = A_1(x,t) + A_2(x,t)$, it can be shown that in this case it has the form of

$$A_{res}(x,t) = 2A_0 \cos\left(\frac{\Delta\phi}{2}\right) \sin\left(kx - \omega t + \frac{\Delta\phi}{2}\right) \tag{3.36}$$

with $\Delta\phi = \phi_1 - \phi_2$ [28]. If both waves have the same phase or $\Delta\phi = n \cdot 2\pi$, with n being a random integer, the cosine-term equals 1 and they interfere constructively and if $\Delta\phi = n \cdot \pi$ the cosine-term vanishes and they interfere destructively with $A_{res} = 0$. Due to energy conservation it is not possible to, for instance, let two beams overlap so that only destructive interference happens. Instead, patterns with destructive and constructive interference are observed.

In every common wave theory there is a square relation between the amplitude and the intensity of a wave, $I \propto A_0^2$. The intensity is known as the power per area and is given in the three-dimensional case as $[W/m^2]$. This always leads to a second-order dependence of the interference term on the amplitudes.
In a general case, if two waves with the complex amplitude $A_1$ and $A_2$ superpose, this means that the intensity shows a behaviour of

$$I_{12} = |A_1|^2 + A_1^* A_2 + A_1 A_2^* + |A_2|^2 , \tag{3.37}$$

where the amplitudes are not expressed explicitly. It is now evident that the intensity of the wave generated by the superposition of two incoming waves is not equal to the sum of the individual intensities of the incoming waves but differ by the $A_1^{(*)} A_2^{(*)}$-terms. We will name those terms interference-terms and the phenomenon as interference itself, equivalent to interference in the double-slit experiment described in section 2.

### 3.2.1 Binomial Theorem and Second-Order Interference

The sum of two terms to the power of any integer number is generally described by the binomial theorem [3]:

$$(a+b)^n = \sum_{k=0}^{n} \binom{n}{k} a^{n-k} b^k \tag{3.38}$$

Since for a square-relation $n = 2$ any order bigger than 2 is restricted and any interference terms in all wave theories with a square-relation are reducible to second-order.

### 3.2.2 Intensity and Fields in Electrodynamics

As mentioned previously, the electrical field of light can be described as in equation 3.16 as $E(z,t) = E_0 e^{i(kx-\omega t)} + c.c.$. Also in electrodynamics there is a square-relation between the amplitude of the field and the intensity of the electromagnetic wave. In case of a monochromatic wave it reduces to the absolute value of the amplitude of the wave [22]:

$$I = \left| E_0(x) \right|^2 \tag{3.39}$$

Since the superposition principle also applies in electrodynamics, a case as in equation 3.37 can be evaluated. When substituting

$$\begin{aligned} E_1 &= \sqrt{I_1} e^{i\phi_1} \quad \text{and} \\ E_2 &= \sqrt{I_2} e^{i\phi_2} \end{aligned} \tag{3.40}$$

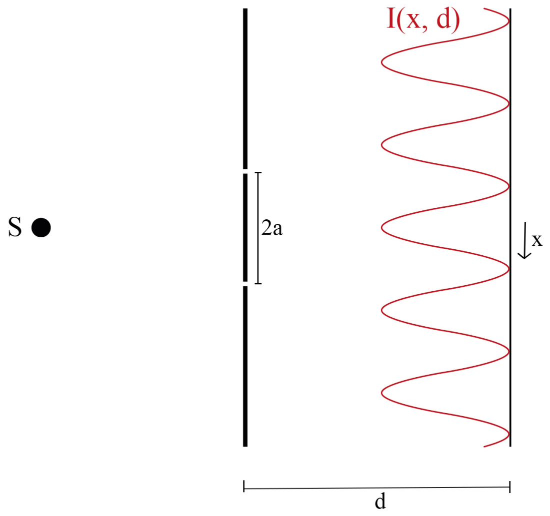

**Figure 3.13: Interference pattern of the double-slit experiment.** Spherical light is sent onto a mask with two pinholes or slits, respectively, and further the waves coming from each slit produce a periodic pattern on a detecting screen by interfering with each other.

into equation 3.37, a relation for the intensity $I_{int}$ resulting wave can be obtained [22]:

$$I_{int} = I_1 + I_2 + 2\sqrt{I_1 I_2} \cos(\Delta\phi) \tag{3.41}$$

In the case of no phase shift between the waves ($\Delta\phi = 0$), $2\sqrt{I_1 I_2}$ has the role of the interference term. It can be seen, that this is analogous to the interference terms in the double-slit experiments from chapter 2.

### 3.2.3 The Double-Slit Experiment and Classical Interference

When spherical waves fall onto a mask with two pinholes or slits and the waves are assumed to be of equal intensity, equation 3.37 can be evaluated as

$$I(x, d) \approx 2I_0(1 + \cos(\frac{2\pi\Theta}{\lambda})), \tag{3.42}$$

with $\Theta \approx \frac{2a}{d}$ being the angle between the two straight paths from each slit towards the specific position on the screen [22]. It can be seen that the superposition of waves in slit experiments leads to an infinitely long periodic intensity pattern. In reality, the finite width of the slits causes the envelope of the intensity pattern as in figure 2.1. However, this is due to diffraction and not due to interference itself. As the slit width gets smaller, the envelope becomes wider. Another limiting factor for an interference pattern along the detection screen in a real experiment is the coherence length of the light source. As the path difference between the light from each path becomes larger along the screen, the light still has to be able to interfere to observe the double-slit pattern. When this path difference gets close to and larger than the coherence length of the light source, the interference pattern gradually vanishes along the screen [29].

### 3.2.4 Generalization of the Number of Slits

Any number M of slits or pinholes, respectively, will still lead to a periodic intensity pattern due to the superposition of the individual waves. In the case of aligned phase relations $\Delta\phi$ between all the waves, the intensity pattern can be expressed as [22]

$$I = I_0 \frac{\sin^2(M\phi/2)}{\sin^2(\phi/2)} \tag{3.43}$$

with ([6])

$$\phi = \frac{2\pi}{\lambda} 2a\, sin(\Theta). \tag{3.44}$$

Here, the angle $\Theta$ can be approximated to be the same for the slits since the distance between the mask and the detecting screen is usually much bigger than the interslit distance.

As mentioned previously, the intensity pattern always results from the superposition principle and the square-relation between intensity and amplitude.

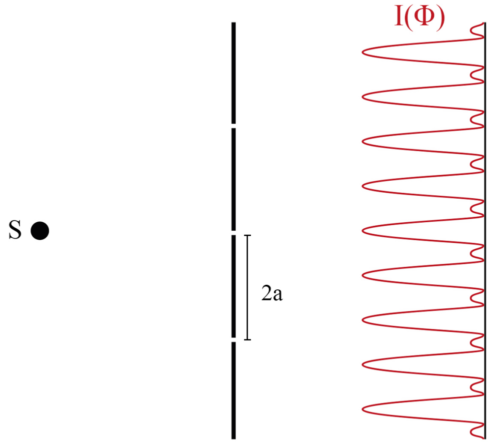

**Figure 3.14: Interference pattern of the triple-slit experiment.** Without diffraction an infinite long intensity patter is obtained as in equation 3.43.

This chapter has shown that the phenomenon of second-order interference was not introduced by quantum mechanics but was already well-known from classical mechanics via the superposition principle and the square-relation between amplitude and intensity.

## 3.3 FOUNDATIONS OF QUANTUM OPTICS

To calculate second-order nonlinear processes occurring in our system within the framework of quantum optics, the following mathematical descriptions and identities have been used. Basically, the input laser light can be described as so-called 'coherent states' and is acted on by a Hamiltonian. As previously mentioned, the system in this experiment can be described by the Hamiltonian from equation 2.21.

$$\hat{H} = \hbar\omega\ \hat{a}\hat{a}^{\dagger} + \hbar\omega\ \hat{b}\hat{b}^{\dagger} + \hbar\omega\ \hat{c}\hat{c}^{\dagger} + i\hbar\chi^{(2)}(\hat{a}\hat{b}\hat{c}^{\dagger} - \hat{a}^{\dagger}\hat{b}^{\dagger}\hat{c})$$

The role of the ladder-operators $\hat{a}$ and $\hat{a}^{\dagger}$ is described in section 2.2.2, showing how the ladder-operators act on simple Fock states. A coherent state $|\alpha\rangle$ is mathematically expressed by

$$|\alpha\rangle = e^{-|\alpha|^2/2} \sum_{n=0}^{\infty} \frac{\alpha^n}{\sqrt{n!}} |n\rangle \,. \tag{3.45}$$

Here, n is equal to the photons in the assigned Fock state $|n\rangle$. $|\alpha|^2$ equals the mean photon number $\bar{n}$ in the coherent state [9]. This means that a coherent state is a superposition of prefactor-weighted Fock states. The mean photon number would be determined by

$$\bar{n} = \langle\alpha|\, \hat{n}\, |\alpha\rangle \,, \tag{3.46}$$

where $\hat{n} = \hat{a}^{\dagger}\hat{a}$ is the so-called number operator. It can be seen from the formulation of a coherent state, that the number of photons in a state follows a Poisson-distribution. Due to the quantum behaviour, the number of photons is set according to this distribution and is collapsed to a specific value upon a measurement. It is also directly proportional to the intensity of the beam.

### *Baker-Campbell-Hausdorff Formula*

In general, a common expansion in quantum optics is the 'Baker-Campbell-Hausdorff'-formula [9],

$$e^{s}\hat{X}\hat{Y}e^{-s\hat{X}} = \sum_{m=0}^{\infty} \frac{s^m}{m!}[X,Y]_m, \tag{3.47}$$

with

$$\begin{aligned} [X,Y]_m &= [X,[X,Y]_{m-1}] \\ [X,Y]_0 &= Y \end{aligned} \tag{3.48}$$

and $[X,Y] = XY - YX$ being the commutator of the operators X and Y. A concrete expansion is given by

$$e^{s\hat{X}}\hat{Y}e^{-s\hat{X}} = \hat{Y} + s[\hat{X},\hat{Y}] + \frac{s^2}{2}[\hat{X},[\hat{X},\hat{Y}]] + ... \tag{3.49}$$

Since this expansion is very often useful in combination with the ladder operators, it is extremely important for quantum optics. In chapter 5, a direct example is given to determine the efficiency of a sum-frequency generation process.

### *Important Identities*

For the calculation in chapter 5 we made use of basic commutation relations and 'normal order'-identities for the ladder operators [18], namely:

$$[a_i, a_j^\dagger] = \delta_{i,j}; \tag{3.50}$$

$$[a, a] = 0; \tag{3.51}$$

$$[a^\dagger, a^\dagger] = 0 \tag{3.52}$$

and

$$a_1 a_1^\dagger \Rightarrow 1 + a_1^\dagger a_1 \tag{3.53}$$

$$a_2 a_2^\dagger a_1 a_1^\dagger \Rightarrow 1 + a_1^\dagger a_1 + a_2^\dagger a_2 + a_1^\dagger a_1 a_2^\dagger a_2 \tag{3.54}$$

$$a_1^2 a_1^{\dagger 2} \Rightarrow 2 + 4a_1^\dagger a_1 + a_1^{\dagger 2} a_1^2 \tag{3.55}$$

$$a_1^2 a_3^\dagger a_1^{\dagger 2} a_2 \Rightarrow 2a_2 a_3^\dagger + 4a_1^\dagger a_1 a_2 a_3^\dagger + a_1^{\dagger 2} a_1^2 a_3^\dagger \tag{3.56}$$

The technique of normal ordering is used to bring the annihilation operators $\hat{a}$ on the right side, so that in case there is a vacuum state, it acts first on the vacuum state $|0\rangle$ and destroys it and no matter what operators are following, this term will always stay number 0, e.g.

$$\hat{a}^{\dagger 2} \hat{a} |0\rangle = 0. \tag{3.57}$$

With equation 3.57 it becomes clear, why $\hat{a}^{\dagger 2} \hat{a} |0\rangle$ is not equal to $\hat{a}^\dagger \hat{a} \hat{a}^\dagger |0\rangle$ because this would act as

$$\hat{a}^\dagger \hat{a} \hat{a}^\dagger |0\rangle = |1\rangle . \tag{3.58}$$

Therefore, the identities from equations 3.54-3.56 are useful to speed-up a calculation including vacuum states. One example of a calculation to demonstrate the identities resulting not in 0 but in a Fock state, would be using identity 3.55 and letting both formulations act on e.g. Fock state $|2\rangle$:

$$a_1^2 a_1^{\dagger 2} |2\rangle = 12 |2\rangle \tag{3.59}$$

and

$$(2 + 4a_1^\dagger a_1 + a_1^{\dagger 2} a_1^2) |2\rangle = 12 |2\rangle \tag{3.60}$$

As we see, both forms are equal.
In our calculations in chapter 5 we make direct use of normal ordering of the ladder operator, their behaviour and coherent states.

# 4 THEORETICAL EVALUATION AND RESULTS

In this chapter we show how we made use of the nonlinear optical foundations from section 3.1 and a model from Wang H. and Weiner A. (2004) [11] to derive a more detailed model of the experimental arrangement and the nonlinear processes in our setup. By this we include more realistic parameters like the walk-off effects, interaction length of the light beams, the group velocity mismatch, a Gaussian description of the beams and basic optical parameters. From there we get a more realistic description of the observable third-order interference in our arrangement.

### 4.1.1 Evaluation of Coupled Wave Equations

In section 3.1.3, a mathematical description of sum-frequency and difference-frequency generation was obtained in form of three coupled wave equations. A simplified version of the coupled wave equations can be written as

$$\frac{dA_1}{dz} = igA_3A_2^* e^{-i\Delta kz} \tag{4.1}$$

$$\frac{dA_2}{dz} = igA_3A_1^* e^{-i\Delta kz} \tag{4.2}$$

$$\frac{dA_3}{dz} = igA_1A_2 e^{-i\Delta kz} \tag{4.3}$$

with $g_i = \frac{2d_{eff}\omega_i^2}{k_i c^2}$. To give a basic picture of how the intensity of the waves evolves within the crystal, we assume $g = 1$ for all three waves and to have a perfect phase-matching condition $\Delta k = 0$. This can be achieved experimentally by optimizing the nonlinear processes efficiency by tilting the crystal, as mentioned in chapter 3.1.6.

The equations are solved numerically and plotted in 'Matlab' for an idealized crystal with length 1. The two fundamental beams are named 'signal' and 'idler' as this is a historical convention and the second-harmonic generation beam is labelled as 'pump' beam in our case. The signal and idler beams have an incident field of $E_{1,2} = 1/2$ (a.u.) and the pump beam a field of $E_3(0) = 1/\sqrt(2)$. With these choices, the intensities are normalized as $\left|E_1(0)\right|^2 + \left|E_2(0)\right|^2 + \left|E_3(0)\right|^2 = 1$. The original intention was to vary the input powers of signal, idler and the pump beam to optimize the Sorkin parameter with the model of the coupled wave equations. Although we later realized that they may not provide an accurate model, we still present it here for demonstration and as motivation to find a more accurate description.

The coupled differential equations are evaluated for hundred equidistant points along the crystal and the intensities for each point are plotted versus the crystal length in figure 4.1. This is the completed analysis complementary to figure 2.13 from the introductory section 2.2.3. In the case of sum-frequency generation the field of the pump beam was set to be $E_3 = 0$ at the beginning of the crystal and in case of the difference-frequency generation the field of the idler beam was set to be $E_2 = 0$ and so forth. In figure 4.1, the individual processes are shown. While each individual plot agrees with the expected behaviour, a Sorkin parameter can be obtained when measuring in all three paths as shown in figure 4.2. Figure 4.2 reveals the advantage in magnitude of the parameter measured in the pump path. Hence, in order to maximize the signal-to-noise ratio related to the estimation of the Sorkin parameter, the intensities are measured in the pump path. Again, the Sorkin parameter can become negative, if due to $\chi^{(2)}$-processes more energy is taken out of the specific path and generated in the other paths than generated in that path. The unit mW here represents the contribution of the whole power that ends up in third-order interference. The negative sign hereby does not indicate a negative power itself, but only a negative Sorkin parameter as described above.

When the crystal length is increased, an oscillating three-wave mixing behaviour is observed. In the case when a beam is generated by difference-frequency generation, its field grows along the crystal and its probability to interact with one of the other beams increases which leads to sum-frequency generation and a decrease of these fields. The same happens to the the other beams involved in the nonlinear wave mixing. The case of difference-frequency generation over a longer medium (still arbitrary units) is shown in figure 4.3. As already discussed in chapter 3.1, walk-off effects limit the nonlinear efficiency and the nonlinear oscillations in figure 4.3 are not observed experimentally.

Figure 4.2 also shows that we have decided for assigning the Sorkin-parameter with the units of mW in our experiment and that it can also take negative values. We chose mW because that way we describe the portions of the light beams that are interfering in third-order. If we want to have the Sorkin parameter dimensionless as in the experiments from chapter 2 we would have to normalize $\kappa$ by the total intensity of the input light to get the proportional contribution. However, in our case we want to observe any component that interferes as third-order term and therefore go with mW. That $\kappa$ can also take negative values comes from its definition as in equation 2.9. If, for instance, in our experiment the DFG-terms $P_{13}$ and $P_{23}$ are big and more light is taken out of the mode 3 towards other paths then the other paths generate in mode 3, $\kappa$ can also become negative in that path. Of course, this also corresponds to the other paths and specific configurations if more light is taken out of a path than generated in that path.

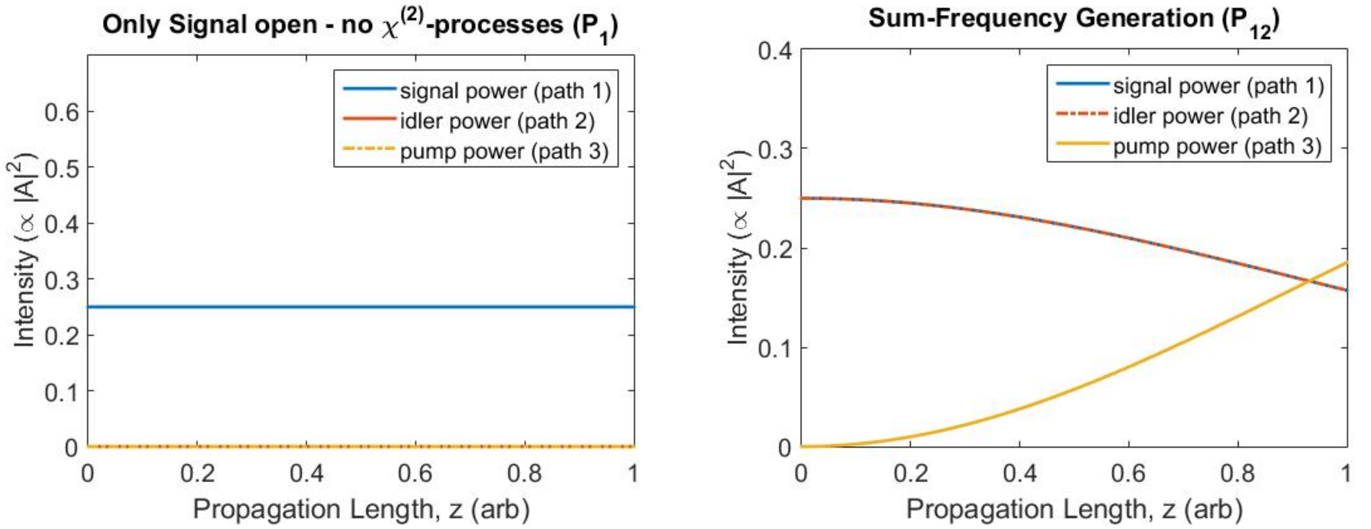

**(a)** $P_1$ **(b)** $P_{12}$

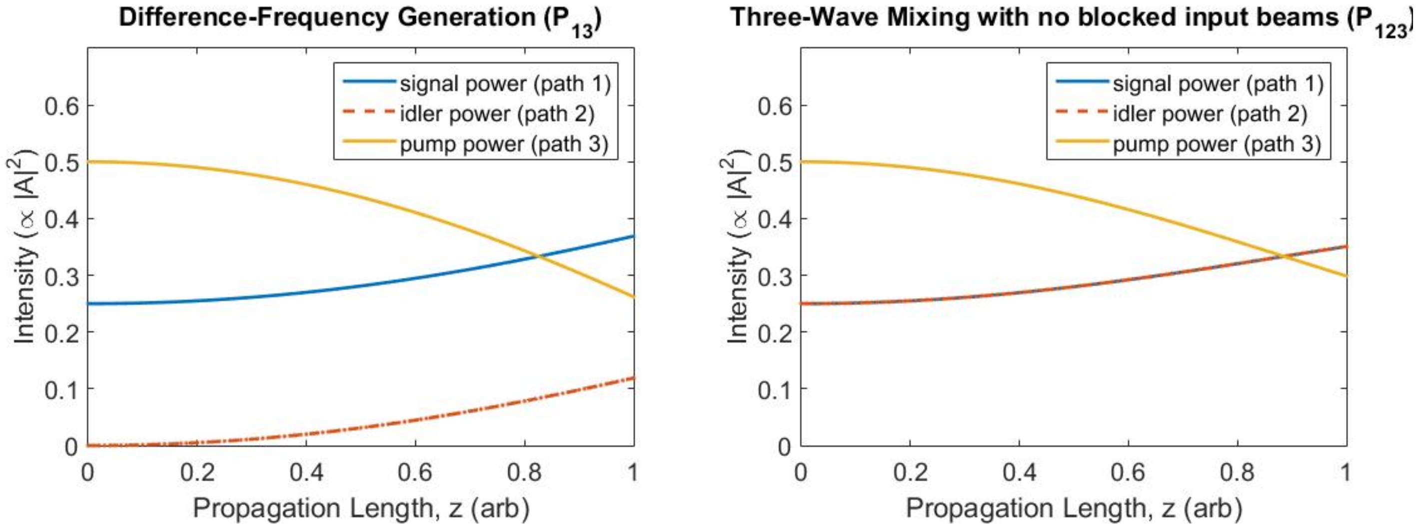

**(c)** $P_{13}$ **(d)** $P_{123}$

**Figure 4.1: Visualising of the processes used to determine the Sorkin parameter.** (a): If only one beam is open, no nonlinear process is present. The shown behaviour of the signal beam ($P_1$) is identical to the other two one-beam configurations ($P_2$ and $P_3$). (b): Sum-frequency generation of the pump beam initialized by presence of signal and idler. The intensity measurement of this configuration would be labelled as $P_{12}$. (c): Difference-Frequency Generation: The idler beam is generated by the presence of the signal and pump beam ($P_{13}$). The behaviour is also valid for a blocked signal and open idler beam ($P_{23}$). (d): Full three-wave-mixing when all three beams are open.

### *Experimental Parameters and Three-Wave Mixing*

As a first step towards a more realistic treatment of the $\chi^{(2)}$-processes, we determine the constants $g_i$ of equations 4.1 - 4.3 with $g_i = \frac{2d_{eff}\omega_i^2}{k_i c^2}$. Since our laser (tunable mode-locked femtosecond Ti:sapphire laser from Coherent) emits light in the visible range, we set $\lambda_{s,i} = 800$ nm for the signal and idler beams. This means that the generated light

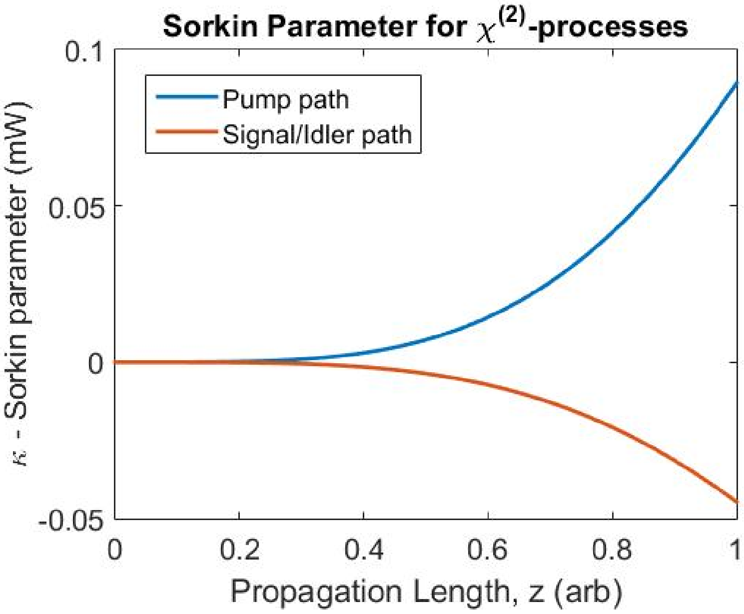

**Figure 4.2: The Sorkin parameter evolving along the crystal.** At $z = 1$ it can be seen that the Sorkin parameter of path 3 and the parameter of the signal or idler path differ in magnitude.

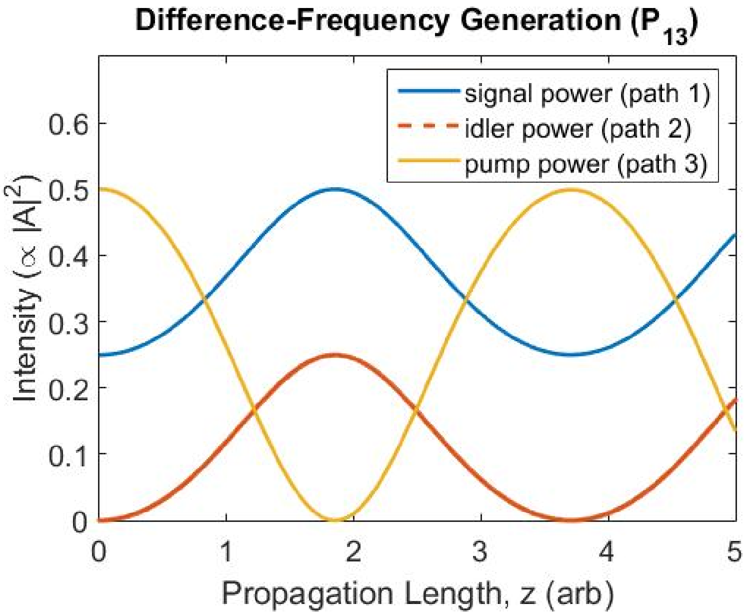

**Figure 4.3: Difference-frequency process in analogy to figure 4.1 bit with increased crystal length.** An oscillating behaviour can be observed due to the presence of all three-photon processes.

in the pump mode will have a wavelength of $\lambda_p = 400$ nm when created by second-harmonic generation. All three beams will then be within the visible spectrum for the human eye which is of experimental convenience. This leads to $\omega_{s,i} = 2.3546 \cdot 10^{15}$ s$^{-1}$ and $k_{s,i} = 1.2566 \cdot 10^7$ m$^{-1}$ for the signal and idler beams - also referred to as red beams. For the pump beam the magnitudes are $\omega_{s,i} = 4.7091 \cdot 10^{15}$ s$^{-1}$ and $k_{s,i} = 2.5133 \cdot 10^7$ m$^{-1}$, also referred to as blue beam. The effective nonlinear strength $d_{eff}$

is determined for the used crystals made by the company 'CASTECH INC'. From the provided data of the reduced susceptibility matrix in equation 3.5 and the relation of equation 3.19 [12] we obtain a value of $d_{eff} = -0.86$ pm/V. Furthermore, the real crystal length of $l = 3$ mm and realistic powers can be included. The first approach is to distribute them in a ratio signal/idler $\frac{1}{4} : \frac{1}{2}$ pump similar to the simple model. To go further, in section 3.1.7 walk-off effects were described and especially the spatial walk-off effects limits the length over which the $\chi^{(2)}$-processes take place, meaning one can not assume to take the crystal length as an interaction length of the three beams. To get a more realistic interpretation of the interaction length, we follow part of the work 'Efficiency of Short-Pulse Type-I Second-Harmonic Generation With Simultaneous Spatial Walk-Off, Temporal Walk-Off, and Pump Depletion' by Wang H., and Weiner A. (2004) [11] where a model for a realistic scenario of type-I second-harmonic generation in a nonlinear crystal is derived. We follow their procedure and gain insights into realistic magnitudes for the combined spatial and temporal walk-off $l_{ST}$. The generalized walk-off length, $l_{ST}$, represents an effective length over which efficient nonlinear optical processes happen. While following their model, the following equations will be slightly adapted to our configuration. They start from a basic relation for the amplitudes of a fundamental and generated light beam in the case of continuous wave (no pulsed input) and plane waves similar to equation 3.22,

$$A_2(L) = -i\kappa \int_0^L A_1^2(z') exp(i\Delta k z') dz' \ , \tag{4.4}$$

with $\kappa = \frac{\omega_1 d_{eff}}{n_2 c}$ and the subscripts 1 (2) refer to the fundamental (generated) wave. The fact that energy propagates from a source point (x', y', z') to the observer point (x, y, L) along the Poynting vector allows them to find basic geometrical relations between the source and the observer point:

$$\begin{aligned} x' &= x - \rho L + \rho z' && (4.5) \\ y' &= y && (4.6) \\ z &= L && (4.7) \end{aligned}$$

The last relation $z = L$ means that the observer is directly at the end of the crystal which is also the maximum length, over which the processes could take place. To distinguish from a continuous wavelength (CW) light and our pulsed light, a time dependence is introduced by

$$t' = t - \frac{L - z'}{V_2}, \tag{4.8}$$

where $V_2$ is the group velocity of the second-harmonic wave. The assumption that the wave forms do not change along the crystal results in a vanishing group velocity dispersion (GVD) and is valid for the femto-second pulses that are provided by our laser

[11][5]. This supports the relation between source and observer by using equations 4.5 - 4.8:

$$\begin{aligned} A_2(x,y,L,t) &= -i\kappa \int_0^L A_1^2(x',y',z',t') exp(i\Delta k z') dz' \\ &= -i\kappa \int_0^L A_1^2(x-\rho_L+\rho z', y, z', t-\frac{L}{V_2}+\frac{z'}{V_2})\ exp(i\Delta k z') dz' \end{aligned} \tag{4.9}$$

This procedure is now applied to a Gaussian beam. Assuming the incoming beam to have a Gaussian distribution both temporally and spatially, the initial description of the fundamental wave has to be modified. Assuming no chirp of the laser beam (as in the case of the laser used in this experiment [5]) the fundamental beam can be described by

$$\begin{aligned} A_1(x',y',z',t') = &\frac{A_0}{\sqrt{(1-i\tau_x(z'))(1-i\tau_y(z'))}} \\ &\cdot exp(-\frac{x'^2}{w_{0x}^2(1-i\tau_x(z'))} \\ &\cdot exp(-\frac{y'^2}{w_{0y}^2(1-i\tau_y(z'))} \\ &\cdot exp(-\frac{2\ ln2(t'-\frac{z'}{V_1})^2}{2t_p^2}) \end{aligned} \tag{4.10}$$

with

$$\begin{aligned} \tau_x(z') &= \frac{2(z'-z_{0x)}}{b_x}, \\ \tau_y(z') &= \frac{2(z'-z_{0y)}}{b_y}. \end{aligned} \tag{4.11}$$

Here, $z_{0x}$ and $z_{0y}$ are the offset coordinates from the middle of the crystal to where the beam passes thorugh the nonlinear crystal in the x- and y-direction and $b_{x,y} = 2\pi n_1 \frac{w_{0x,y}^2}{\lambda}$ and $w_{0x,y}$ are the confocal parameter and the beam waist in the x- and y-direction. By applying the relation of equation 4.9 to the case of the Gaussian beam, the propagation of the amplitude can be described by

$$\begin{aligned} A_2(x,y,L,t) = &\frac{-i\kappa A_0^2}{\sqrt{(1-\tau_x(L))(1-i\tau_y(L))}} exp(-\frac{2y^2}{w_{0y}^2(1-i\tau_y(L))}) \\ &\int_0^L \frac{exp(i\Delta kz)}{\sqrt{(1-i\tau_x(z'))(1-\tau_y(z'))}} exp(-\frac{2(x-\rho L+\rho z')^2}{w_{0x}^2(1-i\tau_x(L))}) \\ &exp(-\frac{4\ ln2(t-\frac{L}{V_2}+\beta z')^2}{t_p^2})\ dz'. \end{aligned} \tag{4.12}$$

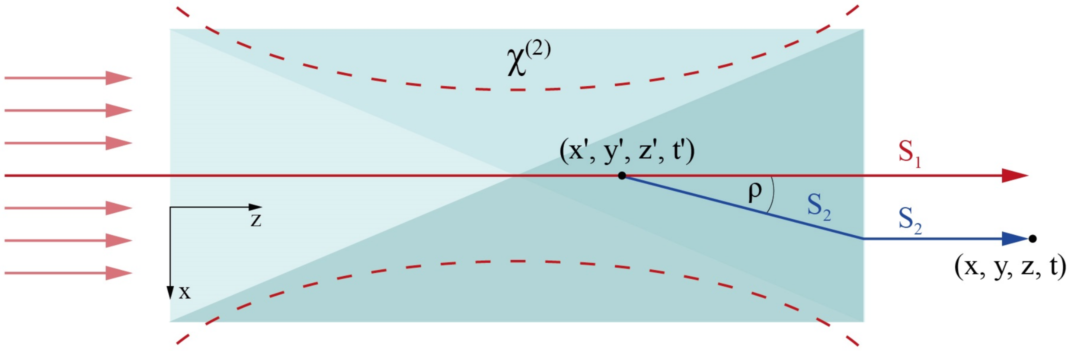

**Figure 4.4: Geometry of second-harmonic generation in a nonlinear crystal.** The incoming beam is partly converted inside the crystal at a source point (x',y',z',t'). The SHG light propagates from the source point by a walk-off angle $\rho$ with respect to the fundamental beam towards the end of the crystal. After leaving the crystal the propagation directions and therefore the Poynting vectors $S_1$ and $S_2$ are collinear.

By squaring the amplitude in equation 4.12 and therefore evaluating the energy of the second-harmonic generated wave, Wang and Weiner could extract a term describing the combined spatial and temporal walk-off. The generalized walk-off length,

$$l_{ST} = (\frac{\rho^2}{w_{0x}^2} + \frac{16\ \beta^2\ ln2}{8\ t_p^2})^{-1/2}, \tag{4.13}$$

describes an effective length over which the fundamental and the generated beam overlap in space and time [11]. Here $w_{0x}$ is the beam waist in the x-direction, $\rho$ is the walk-off angle, $t_p$ is the pulse duration of a laser pulse and $\beta$ is the mismatch between the group velocities $\beta = \frac{1}{V_2} - \frac{1}{V_1}$. Since the derivation up to this point matches the situation in our experiment, $l_{ST}$ is taken to be the new length over which the processes are assumed to be present if $l_{ST} < l_c$ instead of the crystal length $l_c$. The derivation followed from [11] is extended by the assumption that the so-called chirp-factor of the laser light is $\alpha = 0$ [5]. Furthermore, we assume the beam waist to be centro-symmetric and just name it $w_0$.

For our laser light at 800 nm the beam waist has been calculated by means of knife-edge measurements to be $w_0 = 27\ \mu$m.

When a non-collinear nonlinear wave mixing is considered, as in figure 3.10, the effective angle $\rho$ between the pump and the signal beam is dominated by the geometrical angle, which is larger than the walk-off angle, since this is the dominating angle. Because the configuration is assumed to be fully symmetrical, the angle is taken to be equal to the one between the pump and the idler beam. The angle $\rho$ was measured in the lab for the crystal to be $\rho = 1.5°$ after evaluating the distances in free space. Considering the Snell's Law of $sin(\rho) = sin(\rho_c) \cdot n_c$ and the refractive index of $n_c = 1.61$ for the LBO crystal [1], we obtain an angle of $\rho_C = 0.93°$ inside the crystal. For the SFG-term

$P_{12}$ and the three-wave mixing term $P_{123}$ we take $2 \cdot \rho_C$ as the dominating angle due to the geometrical configuration (see figures 3.10 and 3.11). For the sake of a quick evaluation, within this thesis the error associated to the angle measurement has not been propagated. However, when this model is used in the future to compare measured results to calculated values, the model should be evaluated with its error bars to give a regime rather than ideal points.

For the group velocities we make use of the group velocity indices for the different wavelengths. Since the group velocity index $n_g$ differs from the refractive index for pulses and describes how fast the pulse envelopes propagate, the mismatch is described by $\beta = \frac{1}{V_2} - \frac{1}{V1}$. The indices are taken from [11] and we obtain $\beta = 1.6315/c - 1.6686/c = -1.2375 \cdot 10^{-10}\ \frac{\mathrm{s}}{\mathrm{m}}$ with c being the speed of light in vacuum. The pulse duration is $t_p = 200 \cdot 10^{-15}$ s at FWHM [5].

With this data an effective walk-off length is obtained to be

$$l_{ST,1} = 3.98 \cdot 10^{-4}\ \mathrm{m} \tag{4.14}$$

for the two difference frequency generation terms and

$$l_{ST,2} = 2.04 \cdot 10^{-4}\ \mathrm{m} \tag{4.15}$$

for three-wave mixing and sum frequency-generation, meaning that efficient nonlinear interaction happens along a length of about one order of magnitude smaller than the crystal length $l_c = 3$ mm. After we have defined a reasonable expression for the interaction length of the beams, a precise description for the amplitude can be extracted from the power of the light pulses. Therefore one has to calculate the amplitudes from the laser power first. Usually the power of the incoming laser light is known and the the field or the amplitudes can be calculated, respectively. To determine the amplitudes, a relation from the supplementary information of [16] is taken:

$$A(\omega) = 4\ (\frac{ln\ 2}{\pi})^{3/4} \sqrt{\frac{P(\omega)}{f\ t_p\ w_0^2\ n\ \epsilon_0\ c}} \tag{4.16}$$

Here, $f$ is the repetition rate of the laser pulses, $t_p$ the pulse duration at FWHM and $w_0$ the beam waist. For the laser used in our experiment, the repetition rate is $f = 76.2\ \cdot 10^6\ \frac{1}{s}$.

By having a more realistic description of the walk-off length and the amplitude of the electric field, the model of the equations 3.23 - 3.22 can be applied with the combined walk-off length $l_{ST}$ and the amplitudes determined from the laser power as in equation 4.16.

Using an input power ratio of signal/idler $\frac{1}{4} : \frac{1}{2}$ pump, which was determined from the simple coupled wave equation-model to give a high Sorkin parameter, and a total input power of 3 W, the model was evaluated.

The plotted results of sum frequency- and difference frequency-generation are shown in figure 4.5. It can be seen that, in principle, the processes can still be quite efficient over

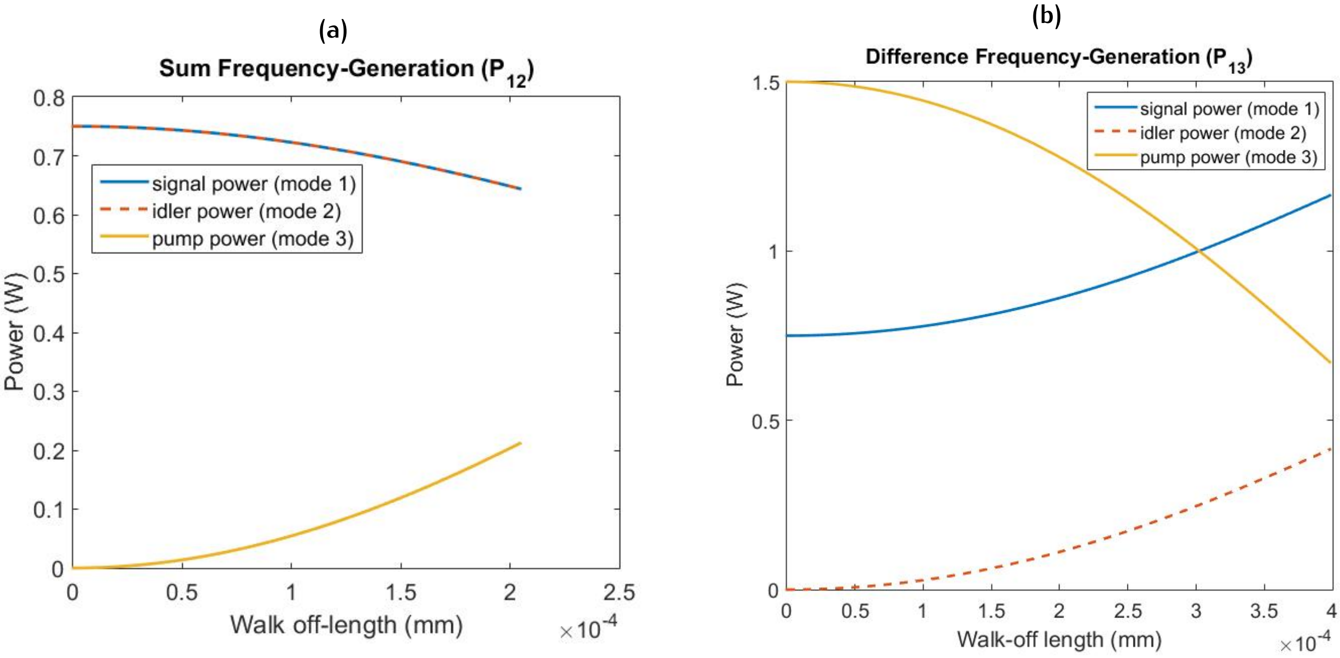

**Figure 4.5: Sum Frequency-Generation (a) and Difference Frequency-Generation (b) of the coupled wave equations-model limited to the length $l_{ST,1}$ and $l_{ST,2}$, respectively, and the amplitudes taken from the input powers via the relation in equation 4.16. a**: SFG referring to the $P_{12}$-term in the Sorkin parameter. **b**: DFG referring to the $P_{13}$-term. The evolution of the $P_{23}$-term is identical when the input powers are identical.

the combined walk-off length. To gain more insights, the efficiencies of the processes are plotted along the interaction length in figure 4.6.

Since the main goal is to obtain third order interference as a consequence of the coupling of the three laser beams via nonlinear interactions, the Sorkin parameter is plotted versus the efficiency of the SFG-process ($P_{12}$) and as previously with the predicted parameters along the interaction length in figure 4.7.

Even though in figure 4.7 identical behaviour is seen in both plots, the insights are given by the abscissa. It can be seen, that the presence of third-order interference is dependent on nonlinear processes.

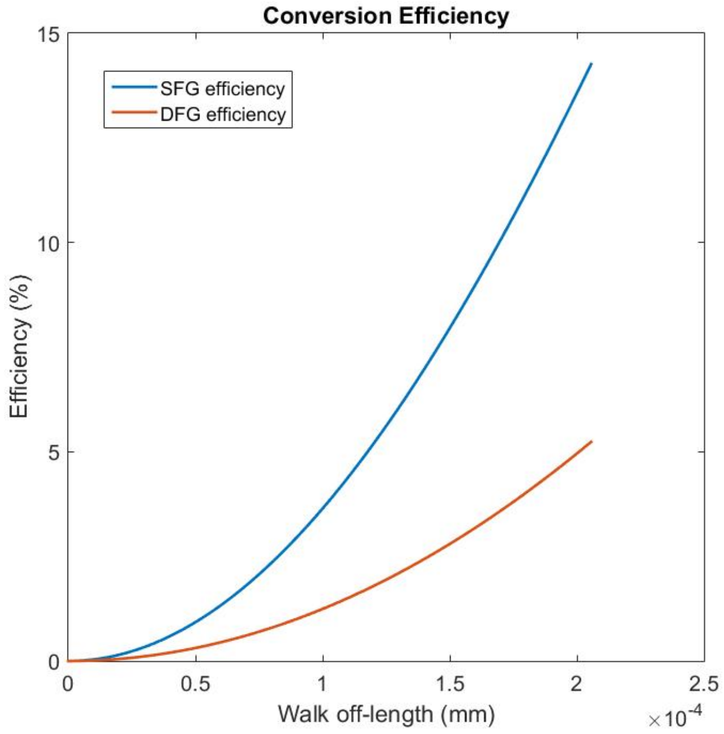

**Figure 4.6: The efficiencies of the $\chi^{(2)}$-processes along the interaction length.** The blue line shows the efficiency of the SFG-process from figure 4.5 (a) and the red line shows the efficiency of the DFG-process from 4.5 (b).

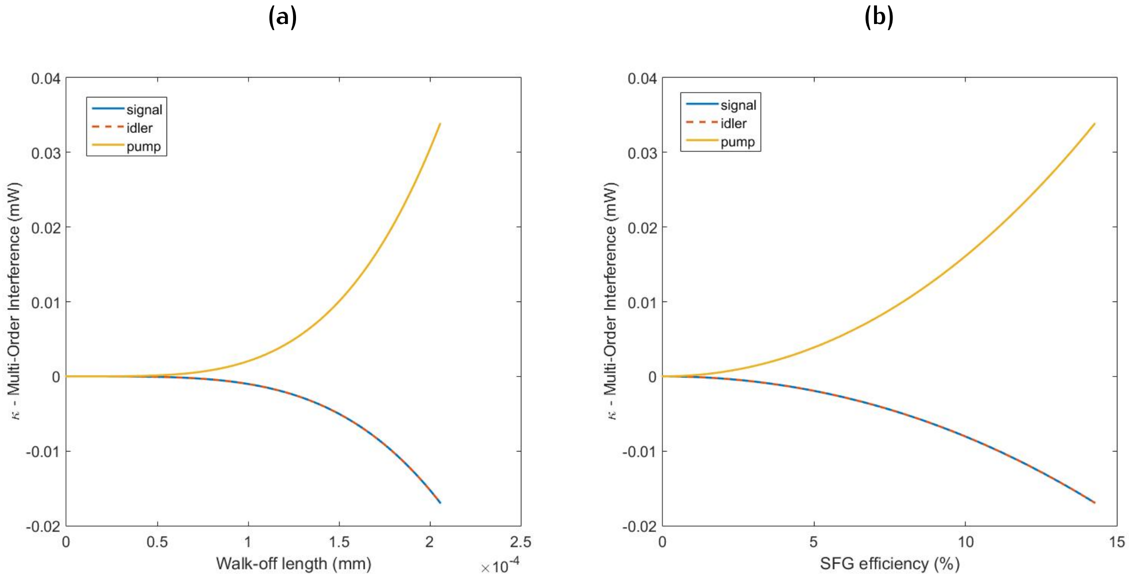

**Figure 4.7: Sorkin parameter as a function of the interaction length (a) and the efficiency of the SFG-process (b).** The behaviour is identical since the efficiencies of the $\chi^{(2)}$-processes increase along the interaction length.

# 5 THEORETICAL CALCULATION IN THE FRAMEWORK OF QUANTUM MECHANICS

In this chapter we provide a full quantum optical description of our system and an approximation for the second-order susceptibility in the Hamiltonian. Since in the literature there is no straight-forward relation between $\chi^{(2)}$ in quantum optical and in classical units, usually further assumptions on the system are made. We used the evolution of a vacuum state to obtain an explicit form. This formis then expanded by a Baker-Campbell-Hausdorff expansion and the expansion parameter was fit to our experimental data. By that we could associate the efficiency of the sum-frequency process with a nonlinearity in the quantum optical picture. This model and the mathematical treatment can be easliy adapted to the other experimental configurations to eventually assign a nonlinearity to all the terms of the Sorkin parameter.

We have done a theoretical calculation of our experimental scenario in a quantum optical framework in the case of sum-frequency generation in the program 'Mathematica'. The starting point is the Hamiltonian of the three-wave mixing of photons as in equation 2.21 formulated in natural units:

$$\hat{H} = (\omega a_1^\dagger a_1 + \omega a_2^\dagger a_2 + 2\omega a_1^\dagger a_1) + i\chi^{(2)}(a_1 a_2 a_3^\dagger - a_1^\dagger a_2^\dagger a_3) \tag{5.1}$$

The challenge is that the second-order susceptibility $\chi^{(2)}$ is commonly of units $\frac{\mathrm{m}}{\mathrm{V}}$ when expressed in SI-units. However, in quantum mechanics the Hamilton operator usually gives the energies of the system and therefore is of energy units when applied onto a wave function. However, physically the same magnitude is meant since it describes the strength of the processes. In literature there is no common relation between the expression in quantum optical and in nonlinear optical units without further assumptions on the quantum mechanical system. Therefore, to give a description of the processes and later of the Sorkin parameter from experimental data, a mathematical model had to be found to connect experimental data to the nonlinearity in the Hamiltonian of the system. In equation 5.1, the left parts in the brackets represent the energy in each mode with the constraint that photons in mode three are of half the wavelength and, therefore, double the energy as the photons in modes 1 and 2. The nonlinear term then represents the $\chi^{(2)}$ processes as described in chapter 2.

When we assume, for instance, a SFG scenario as in $P_{12}$ and want to obtain the number of the generated photons in mode 3 to get the nonlinearity of the process, it makes sense to assume an incoming vacuum state $|0\rangle$ in mode 3 and calculate the expectation value of the number operator $\hat{n}_3 = \hat{a}_3^\dagger \hat{a}$ in the outcome mode. The evolution of a state in general is given by $|f\rangle = e^{i\hat{H}t}|i\rangle$ with $|i\rangle$ being the initial state and $|f\rangle$ being the final state. When now the average number of photons of the final state should be obtained, it can be done as

$$\langle \hat{a}^\dagger \hat{a} \rangle_f = \langle f | \, \hat{a}^\dagger \hat{a} \, | f \rangle \,. \tag{5.2}$$

In our case, when vacuum is assumed to be the input state in mode 3 and the system is described with the Hamiltonian $\hat{H}$ from equation 5.1, this leads to

$$\langle \hat{a}_3^\dagger \hat{a}_3 \rangle_3 = \langle 0 | \underbrace{e^{-i\hat{H}\tau} \hat{a}_3^\dagger \hat{a}_3 e^{i\hat{H}\tau}}_{\Rightarrow BCH} | 0 \rangle \,. \tag{5.3}$$

To get an approximation for the numbers of photons that are generated in the pump mode via sum-frequency generation between signal and idler, we can now make direct use of the Baker-Campbell-Hausdorff expansion of the underbraced term in equation 5.3, $e^{-i\tau\hat{H}} \hat{n}_3 e^{-i\tau\hat{H}}$, where $\hat{n}_3 = \hat{a}_3^\dagger \hat{a}_3$ is the number operator that gives the number of photons in the specific mode as mentioned previously. The expansion here is done up to the 6th order to obtain a reasonable approximation compared to experimental data. This was found by iterative comparing of the outcome with the measured data. The validity of the approximation can be seen in figure 5.1. The following result is shortened for simplicity while the full calculation can be seen in the appendix:

$$\begin{aligned}
O(1) &= \tau\chi \quad (a_1 \cdot a_2 \cdot a_3^\dagger + a_1^\dagger \cdot a_2^\dagger \cdot a_3 \ ) \\
O(2) &= \tau^2\chi^2 \ (-a_3^\dagger \cdot a_3 + a_1^\dagger \cdot a_1 \cdot a_2^\dagger \cdot a_2 - a_1^\dagger \cdot a_1 \cdot a_3^\dagger \cdot a_3 - a_2^\dagger \cdot a_2 \cdot a_3^\dagger \cdot a_3 \ ) \\
O(3) &= \tau^3\chi^3 \ (-\frac{1}{3} 2 a_1 \cdot a_2 \cdot a_3^\dagger - \ \ldots \ - \frac{2}{3} a_1^{\dagger 2} \cdot a_1 \cdot a_2^\dagger \cdot a_3 \ ) \\
O(4) &= \tau^4\chi^4 \ (\frac{1}{3} a_3^\dagger \cdot a_3 - \ \ldots \ + 2 a_1^\dagger \cdot a_1 \cdot a_2^\dagger \cdot a_2 \cdot a_3^\dagger \cdot a_3 \ ) \\
O(5) &= \tau^5\chi^5 \ (\frac{2}{15} a_1 \cdot a_2 \cdot a_3^\dagger + \ \ldots \ + \frac{13}{15} a_1^{\dagger 2} \cdot a_1 \cdot a_2^{\dagger 2} \cdot a_2 \cdot a_3 \ ) \\
O(6) &= \tau^6\chi^6 \ (-\frac{21}{45} a_3^\dagger \cdot a_3 + \ \ldots \ - \frac{58}{45} a_1^{\dagger 2} \cdot a_1^2 \cdot a_2^\dagger \cdot a_2 \cdot a_3^\dagger \cdot a_3 \ )
\end{aligned} \tag{5.4}$$

where

$$e^{-i\tau\hat{H}} \hat{n}_3 e^{-i\tau\hat{H}} = O(1) + O(2) + O(3) + O(4) + O(5) + O(6) \quad (+ \ldots) \tag{5.5}$$

For simplicity we left out the ‘Hat’-notation of the ladder operators in the expansion. Now it can be seen, why the normal order identities from equations 3.54 - 3.56 and equation 2.23 make sense to be applied, since as described in section 2.2.2, $\hat{a}_3$ can be set to 0 when it is applied onto vacuum. The same is valid for $\langle 0 | \, a_3^\dagger = 0$. Since the

ladder operators of the different modes commute, after normal ordering, this form can be achieved to all of the terms with $a_3^\dagger$.
Equation 5.4 is simplified to

$$\begin{aligned}
O(1) &= 0 \\
O(2) &= \tau^2\chi^2 \; (a_1^\dagger \cdot a_1 \cdot a_2^\dagger \cdot a_2) \\
O(3) &= 0 \\
O(4) &= \tau^4\chi^4 \; (-\frac{1}{3}a_1^\dagger \cdot a_1 \cdot a_2^\dagger \cdot a_2 - \frac{1}{3}a_1^{\dagger 2} \cdot a_1^2 \cdot a_2^\dagger \cdot a_2 - \frac{1}{3}a_1^\dagger \cdot a_1 \cdot a_2^{\dagger 2} \cdot a_2^2 \\
O(5) &= 0 \\
O(6) &= \tau^6\chi^6 \; (\frac{2}{45}a_1^\dagger \cdot a_1 \cdot a_2^\dagger \cdot a_2 + \frac{2}{15}a_1^{\dagger 2} \cdot a_1^2 \cdot a_2^\dagger \cdot a_2 + \frac{2}{45}a_1^{\dagger 3} \cdot a_1^3 \cdot a_2^\dagger \cdot a_2 \\
&\quad + \frac{2}{15}a_1^\dagger \cdot a_1 \cdot a_2^{\dagger 2} \cdot a_2^2 + \frac{13}{45}a_1^{\dagger 2} \cdot a_1^2 \cdot a_2^{\dagger 2} \cdot a_2^2 + \frac{2}{45}a_1^\dagger \cdot a_1 \cdot a_2^{\dagger 3} \cdot a_2^3).
\end{aligned} \tag{5.6}$$

Since the input modes for mode 1 and mode 2 are assumed to be coherent states, they can be associated with their amplitudes $\sqrt{n_1}$ and $\sqrt{n_2}$ when assumed to be acting on a coherent state due to their action as $\hat{a}\,|\alpha\rangle = \alpha\,|\alpha\rangle$. The ladder operators can be replaced as $a_i = \sqrt{n_i}$ and $a_i^\dagger = \sqrt{n_i}e$ [9]. Equation 5.6 then transforms to

$$\begin{aligned}
e^{-i\tau\hat{H}}\hat{n}_3 e^{-i\tau\hat{H}} &= \tau^2\chi^2 n_1 n_2 + \tau^4\chi^4(-\frac{1}{3}n_1 n_2 - \frac{1}{3}n_1^2 n_2 - \frac{1}{3}n_1 n_2^2) \\
+ \tau^6\chi^6(\frac{2}{45}n_1 n_2 &+ \frac{2}{15}n_1^2 n_2 + \frac{2}{45}n_1^3 n_2 + \frac{2}{15}n_1 n_2^2 + \frac{13}{45}n_1^2 n_2^2 + \frac{2}{45}n_1 n_2^3)
\end{aligned} \tag{5.7}$$

We have measured a series of input power vs. generated light in the lab and from there we could convert the powers to photon numbers. To convert a measured power in the units of mW to photon numbers, we used the formula

$$n = \underbrace{\frac{\text{average power}}{f_{rep}}}_{\textit{energy per pulse}} \cdot \frac{1}{\text{energy per photon}}. \tag{5.8}$$

To give the energy per pulse, we devide the power measured (average power) by the repetition rate $f_{rep} = 76 \cdot 10^9$ MHz and assume, that the power is not pulsed but in the shape of a periodic step function and we calculate the photons created and annihilated within a pulse. When the energy per pulse is divided by the energy of a photon, we get n, the number of photons per pulse.
For simplicity and to stay in a numerical precise regime, $\kappa = 10^6 \cdot \tau\chi$ was introduced. When now the difference between the measured photon numbers and the predicted photon numbers , also known as residual, is formulated, we obtain

$$\begin{aligned}
f(\kappa) &= 2970.13 - 5565.39 \cdot \kappa^2 + 2777.69 \cdot \kappa^4 - 157.73 \cdot \kappa^6 \\
&\quad + 6.22285 \cdot \kappa^8 - 0.120633 \cdot \kappa^{10} + 0.00158976 \cdot \kappa^{12}.
\end{aligned} \tag{5.9}$$

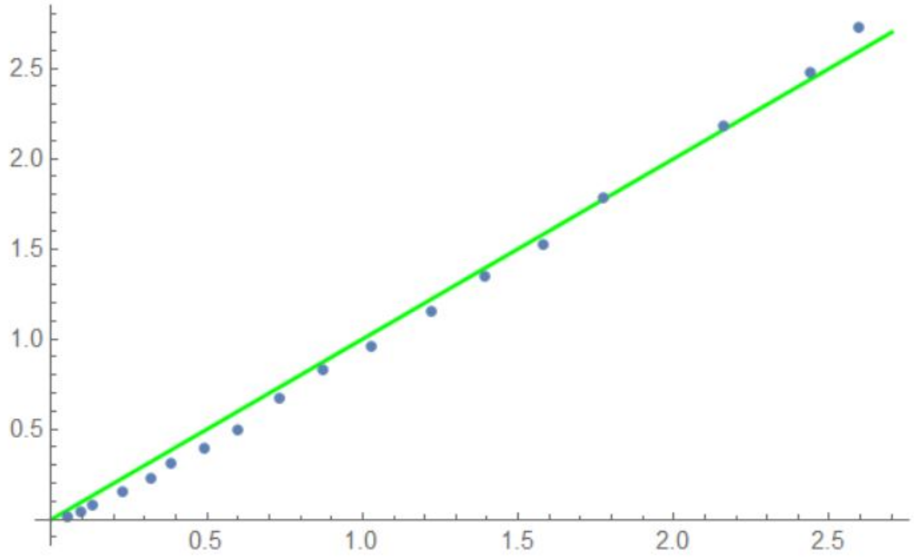

**Figure 5.1: The accuracy of the obtained approximation with the measured data.** The green line represents the function $f(x) = x$. The blue dots are representing the calculated value with the obtained approximation by plotting the calculated value versus the measured value. In an ideal case, the blue dots agree with the green line which is the case up to small boundaries.

When $f(\kappa)$ is minimized with respect to $\kappa$, the approximation is being optimized with respect to the measured data. The minimized value we obtain is $\kappa = 1.04827$. In figure 5.1 the green line represents a plot of $f(x)$ vs. $x$ which is in principle a linear function with a slope of $k = 1$ to compare with. The blue dots represent the calculated data versus the measured data. It can be seen, that the approximated values agree with the measured values quite well. If the values would not agree well, the order of the expansion may be increased. However, via trial and error, an expansion up to the 6th order was shown to be sufficient.

With the model obtained and explained in this chapter, a nonlinearity for measured intensities can be calculated and therefore a Sorkin parameter can be expressed within a quantum mechanical picture by changing the input and output states and the associated ladder operators for the respective $\chi^{(2)}$-processes.

# 6 EXPERIMENT

In this chapter we show the experimental realization of the scenarios explained in the previous chapters. In section 6.1 we explain how we set the experiment up and give insights into the challenges we faced, such as unequal intensities in the red beams, finding the spatial and temporal overlaps, etc. In section 6.2 we present the measurement results. In section 6.2.1 we show the results of the Sorkin parameter in a static configuration, meaning that the distance between the LBO crystal and the lens before is constant. In section 6.2.2 we present the results of a measurement method where this distance was varied to move the crystal in and out of the common focal point to measure the Sorkin parameter in the presence and absence of the nonlinear processes. Although we have some noisy and fluctuating results that prevent us from quantifying the third-order interference precisely, we are confident that we have already observed a non-vanishing Sorkin parameter.

## 6.1 EXPERIMENTAL SETUP

Experimentally, the three light beams that interact by nonlinear processes are obtained with a single pulsed laser and a nonlinear crystal. The setup is sketched in figure 6.1. By modelocking and adjusting the laser, we set the output wavelength at $\lambda = 800$ nm, with a repetition rate of $f = 76$ MHz and a pulse duration of $t_p = 200$ fs (see section 3.1.8). The characteristics of the used laser light are shown in table 6.1.

**Table 6.1:** Characteristics of the pulsed laser light in our experiment. (Values taken from Ref. [5].)

| | |
|---|---|
| Wavelength $\lambda$ | 800 nm |
| Repetition Rate $f$ | 76 MHz |
| Pulse Duration $t_p$ | 200 fs |
| Pulse Energy Variation | 0.1 % |
| Spectral Bandwidth | 10 nm |

Since the laser was also used for another series of experiments, a half-wave plate and a polarized beam splitter (PBS) were placed directly in front of the laser output to further direct the light. The light is transmitted if the polarization is horizontal and reflected if the polarization is vertical. If it is a superposition of both, it is partly transmitted

and partly reflected depending on the probability of having a vertical or a horizontal polarized light. With that we could assign the light to the specific experiment. This also adds a phase shift to the reflected photons, but this is negligible for this experiment. The light is then directed via several mirrors onto a polarizer that filters out the remaining H polarized light that leaks from the PBS. The light that passed the polarizer was then assumed to have one polarization. It is then focused by a $f_1 = 50$ mm focal length lens ($L_1$) onto a nonlinear LBO crystal ($LBO_1$), with a length of $l_{LBO_1} = 3$ mm. Before inserting the LBO crystal, the incoming beam was collimated with a second lens ($L_2$) with the same focal length $f_2 = f_1$. When inserting the first LBO crystal, its position and tilt have to be carefully optimized to meet the phase-matching condition $\Delta k = 0$, as explained in section 3.1.5. From equation 3.25 it can be seen, that a quadratic behaviour between the intensity of the second-harmonic generation and the intensity of the incoming light should be obtained. This was actually tested in section 6.1.2.
To separate the fundamental and the generated SHG beam from each other, a dichroic mirror (DM) was used. This specific dichroic mirror is a long-pass filter, where light with $\lambda = 800$ nm is transmitted and light with $\lambda = 400$ nm is reflected. The characteristics of the dichroic mirror and the dispersive transmission and reflection data are sketched and plotted in figure 6.2. It can be seen that the component works properly for our wavelengths of 400 nm and 800 nm. Since the dichroic mirror shows experimental deviations from the ideal behaviour, two bandpass filters were used to guarantee, within the experimental imperfections, that in each path only the desired light is present. With pinholes and beam-walking techniques, the same spatial height of the three beams is guaranteed throughout the alignment.

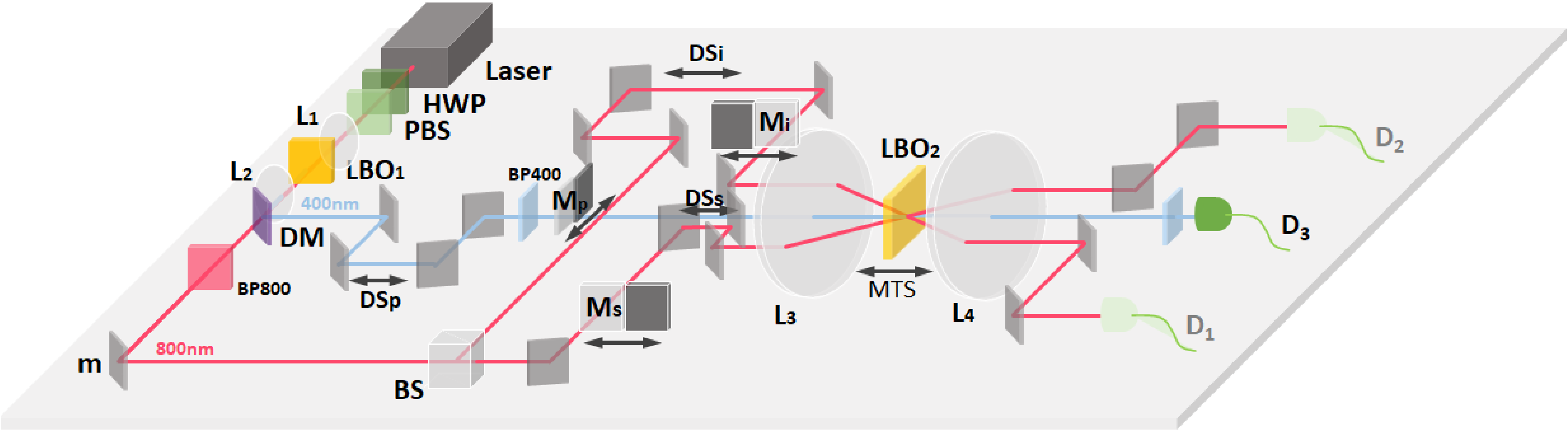

**Figure 6.1: A sketch of the main experimental setup.** An 76 MHz Laser provides 200 fs pulses at 800 nm when modelocked. After some mirrors and pinholes that are not shown, the light is focused and afterwards collimated onto the $LBO_1$-crystal by the lenses $L_1$ and $L_2$, respectively, to generate SHG light. A dichroic mirror (DM) then splits the fundamental and SHG light into two different paths. The light is further filtered by bandpass filters $BP800$ and $BP400$. Three delay stages $DS_p, DS_s$ and $DS_i$ provide the required path length tunability to ensure time overlap. The three beams are then sent to the lens $L_3$ to be focused onto the $LBO_2$-crystal. Via the motors $M_s$, $M_p$ and $M_i$ the individual configurations for obtaining the Sorkin parameter are set. $L_4$ then collimates the beams, a bandpass filter guarantees no leakage from the other paths and a detector measures the beam power. The motorized translation stage was further programmed to change the position of the $LBO_2$-crystal in and out of the focal point of the three intercepting beams.

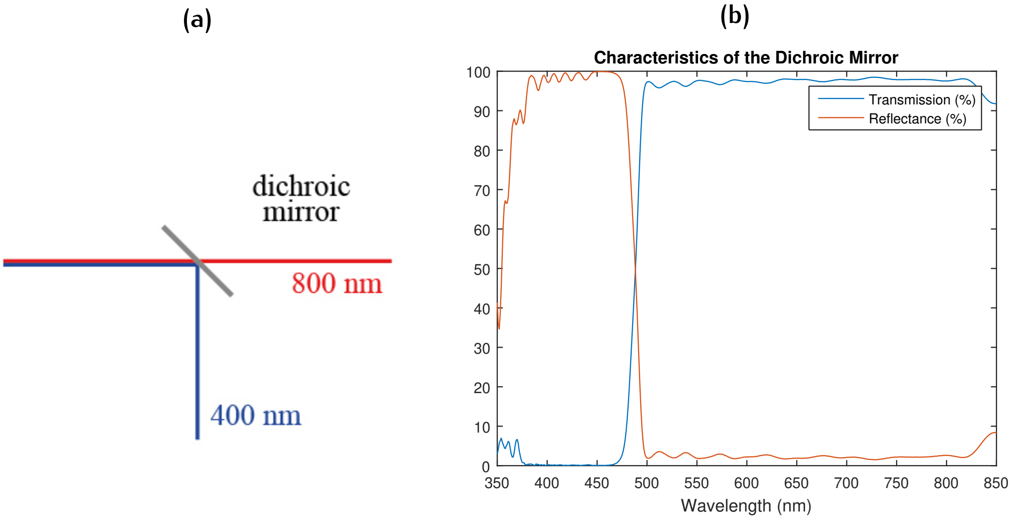

**Figure 6.2: Functioning of the dichroic mirror.** (**a**): the dichroic mirror works as a long-pass filter with the cut-off wavelength at 490 nm. Light above that wavelength is being transmitted and light with a lower wavelength is reflected. (**b**): Transmission and reflection data for the dichroic mirror 'DMLP490T' by 'ThorLabs Inc.' (ThorLabs), which was used in this experiment [13]. It can be seen that around $\lambda = 490$ nm the intersection between reflectance and transmission behaviour is found.

To create three paths and let them interact in the nonlinear crystal $LBO_2$, we split the red beam into two beams with a 50:50 beam splitter. This component ideally just transmits half of the power of a beam and reflects the other half as shown in figure 6.3. In reality, the behaviour deviates significantly from the ideal characteristics, as shown in figure 6.4, where the relevant regime is plotted. The used beam splitter was produced by ThorLabs and labelled 'BS011', which is produced to work in a regime of $700 - 1000$ nm.

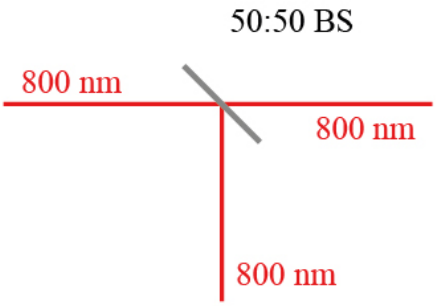

**Figure 6.3: The principle of a 50:50 beam splitter.** Half of the incident beam is reflected and the other half is transmitted. In reality a not ideal behaviour is obtained as shown in figure 6.4.

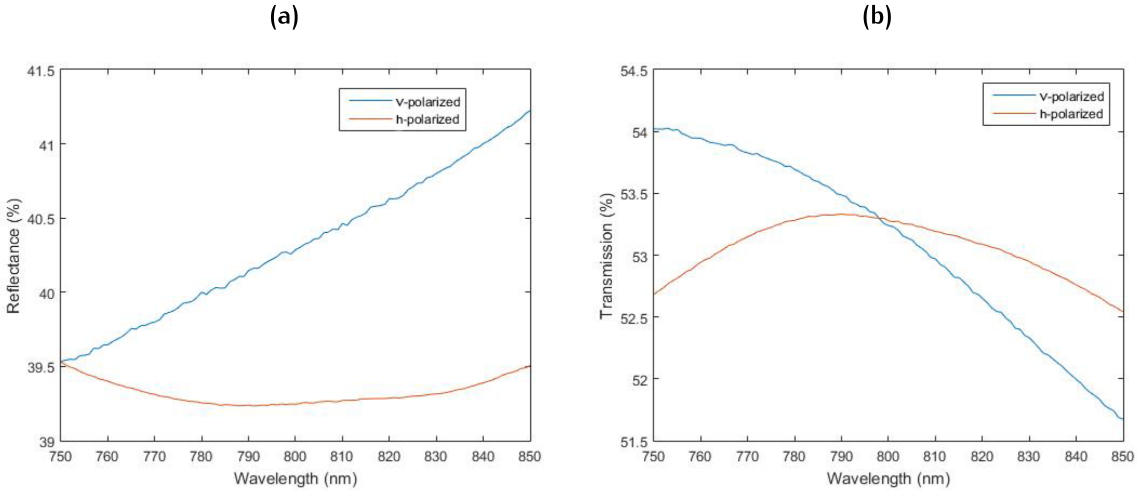

**Figure 6.4: Functioning of the 50:50 beam splitter.** (**a**): the reflectance of the beam splitter for H- and V-polarization in a wavelength regime of 750 - 850 nm. (**b**): The transmission data for H- and V-polarized light.
The data is provided by ThorLabs, which is the producer of the 'BS011' [14].

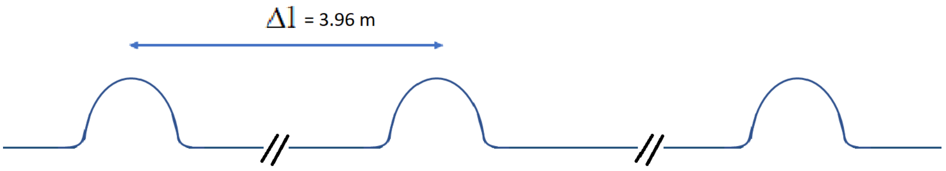

**Figure 6.5: Pulsed laser beams.** Due to the pulsed laser light and the repetition rate, a distance of about 4 m is present between the centers of the power envelopes of the pulses. This introduces the necessity to match the positions of the three pulsed beams.

In figure 6.4 it can be seen that by using a beam splitter, an unequal power distribution between the splitted beams is obtained. In this case, the difference in the two polarization directions can be neglected. According to the provided data, the difference in intensity is about 13 % between the two beams. As ThorLabs states, the total intensity loss is less than 20 % within the working regime of the beam splitter [14]. In reality, the intensities of the two red beams have been measured for 10 seconds each and the results are shown in section 6.1.3.
After the three beams are generated via nonlinear processes and separated by a dichroic mirror and a 50:50 beam splitter, the beams are sent to interact in the $LBO_2$ crystal in a geometric setting similar to the one shown in figure 6.6. At this point it should be mentioned that due to convention and as already described in chapter 2, the two red beams were labelled as 'signal' and 'idler' and the blue beam as 'pump'.

Before interacting in the $LBO_2$ crystal, the three beams are then sent onto individual translation stages. The translation stages behave as delay lines, allowing to change the

path lengths of the individual beams. When it is aligned properly, neither the direction nor the height of the beams are changed when the translation stages are moved. The delay lines are necessary due to the pulsed nature of the used laser light:
Since the laser works with a repetition rate of $f = 76$ MHz, the center of the individual pulses are separated by $\Delta l = 3.96$ m, as shown in figure 6.5. This is much larger than the pulse duration of $t_p = 200$ fs (FWHM), which is equal to a distance of $l_p = 60$ $\mu$m. To generate three photon-processes, the pulses of the individual beams have to overlap in both space and time. This is guaranteed by the correct adjustment of the translation stages.
To interact in the second LBO-crystal ($LBO_2$), we focused the three beams onto the crystal by a lens ($L_3$) with focal length $f_3 = 25$ mm. In the alignment procedure, we checked the red beams first: They were sent symmetrically onto the lens and thereby focused onto the crystal. The common focal point was checked first by eye and then the translation stages were adjusted back and forth carefully. On the other side of the crystal, when both a spatial and temporal overlap was found, a SFG signal could be observed between the red beams.
Due to the beam waist of about $w_0 = 30$ $\mu$m and the pulsed intensity, there is a very specific configuration of the translation stages where the generated sum-frequency pump light is present. This highlights also the necessity of a precise alignment of the translation stages. Otherwise, the beams would lose their spatial overlap and common focal point inside the crystal when adjusting the path lengths. In figure 6.7 a photograph of the SFG signal generated by the red beams is shown. This presents what the generation of $P_{12}$ looks like in reality: When the two red beams share a common focal point inside the crystal and the two pulses meet in time, the blue beam is generated. The blue light in this picture is about 2 mW, while the incident red beams have more than 100 mW each. This was also the reason to start with the blue beam generated by the signal and idler beam. Apart from the different response of the crystal at different processes, the blue beam is more visible by the human eye compared to the red one at the same power. After the blue beam was detected, the optimization procedure consisted of slightly changing the wavelength, adjusting the incidence angle of the red beams onto the $LBO_2$ crystal and finding the most efficient position of the crystal with respect to $L_3$.

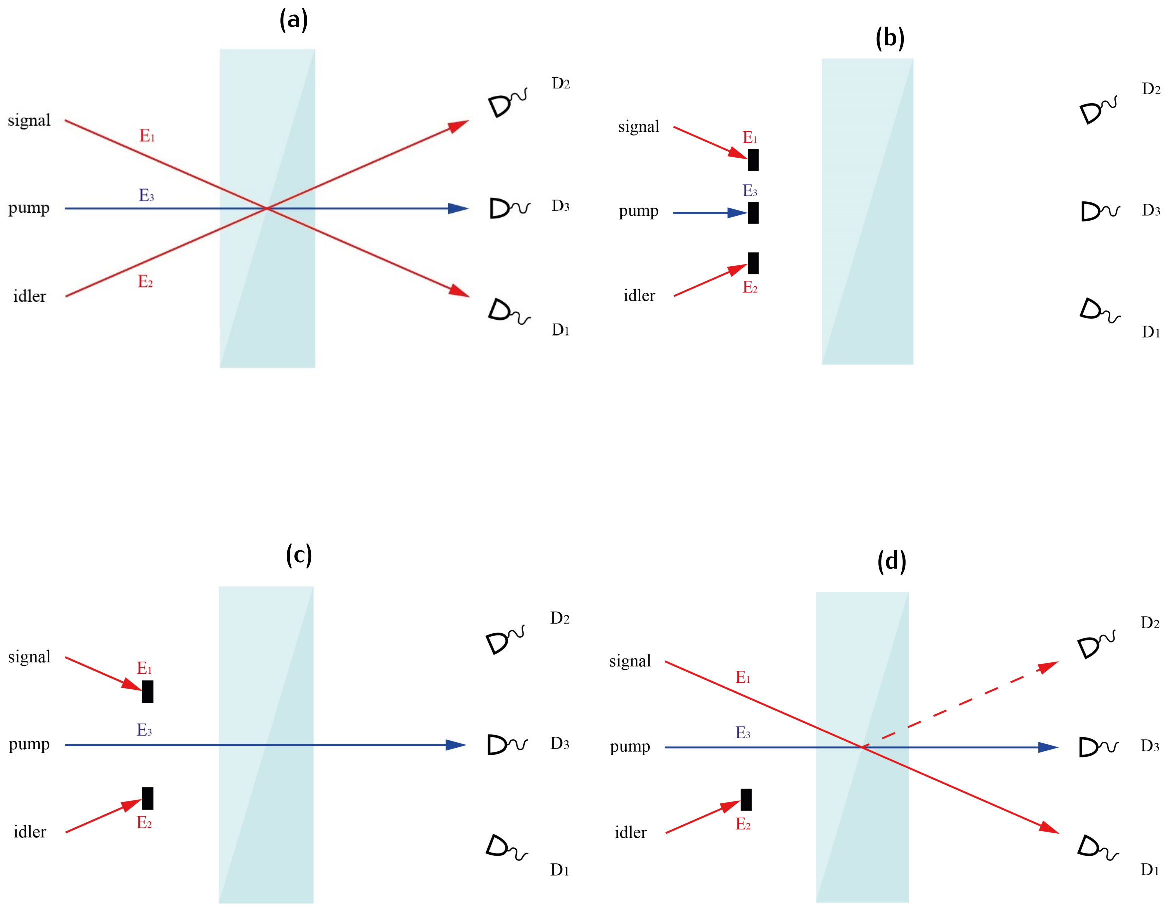

**Figure 6.6: Geometrical arrangement of the laser beams.** The three beams interacting within the nonlinear crystal via $\chi^{(2)}$-processes. The beams are individually opened or blocked depending on the component of the Sorkin parameter that is measured.
(**a**) $P_{123}$ term, with all three beams open.
(**b**) $P_0$ term, which represents the background noise.
(**c**) $P_3$, where light from the signal and the idler path is blocked.
(**d**) $P_{13}$ term, which shows a DFG-process between the signal and pump beam, where light is generated in the idler path. This is equivalent to $P_{23}$ with the signal beam blocked and DFG-processes happening between idler and pump beams. If only the pump path was blocked, signal and idler would generate light in the pump path (path 3) which would represent $P_{12}$.

An interesting insight was given by changing the wavelength of the main pump laser: When this was varied between 790 nm and 805 nm, the various intensities and efficiencies of the $\chi^{(2)}$-processes dropped immediately. (This was often the case when sharing the laser light with other experiments.)
After the wavelength was changed, we tried to align the $LBO_1$ crystal so that the same SHG efficiency as before was obtained. When the alignment of the $LBO_2$ crystal was then optimized for the SFG- and DFG-processes, approximately the same intensities as with other wavelengths in this range could be obtained. A different wavelength leads to a change in the phase-matching angle and the orientation of the crystal axes to the beams for the perfect phase matching condition. This leads to a different walk-off angle and propagation directions within the crystal.
Since the efficiency did not increase by changing the input wavelength and realigning, we decided to stay at 800 nm. Because most of the optical elements were produced to work optimally at 780 nm or 800 nm there was no reason to shift to longer wavelengths. Lower wavelengths would result a the SFG signal in the ultraviolet region and make it harder to be detected by the human eye and the detectors. After the overlap of the red beams was found, the same was done with each red beam and the blue beam as input, and the complementary DFG red beam as an output. (See figure 6.6 (d).)
In fact, experimentally, the spatial and temporal overlap of the DFG-process turned out to be much harder to find. One possible reason for that was found while doing a 'z-scan' as described in section 6.2.2: It could be seen that the optimal efficiency of the DFG-processes is present within a much smaller spatial range than at the SFG processes. Originally, assuming that the DFG-processes tend to be present over a similar length as the SFG-processes, an alignment was obtained where all three processes were present simultaneously after optimizing the SFG signal.

When measuring individual powers, we could clearly see the wavelength dependence of a photodiode power sensor as it is plotted in figure 6.8. Since the powermeter calculates the power of the incident light by measuring the responsivity of the sensor and adjusting this value by the given wavelength, it is important to ensure that the collected power is monochromatic. While blue leakage did not have high influence on the measured power, red light distorted the measured power to a significant percentage; higher than the expected third-order interference component. Especially the non-perfect behaviour of the dichroic mirror had an influence on the powers and therefore bandpass filters were placed to prevent the undesired light to propagate along the wrong path.
In the output paths of the signal and idler beams a small percentage of light was also converted to blue light. Even though it was in the range of $\mu$W, this was still visible by the human eye. This also led to the need of filters.

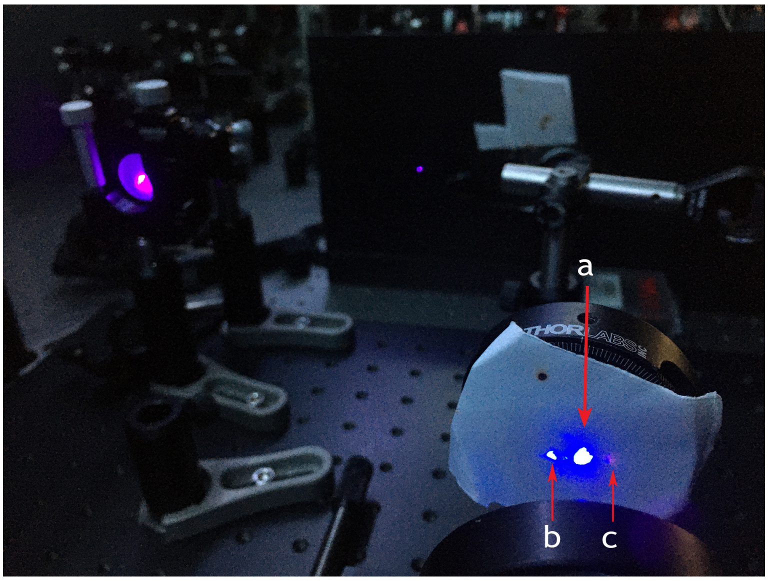

**Figure 6.7: A photograph of the SFG light.** The three beams after the two red beams are sent onto the second crystal and the sum-frequency signal (blue/UV - light) is generated. Due to similar behaviour of the camera ('Apple iPhone 6S') with the human eye, blue light is being captured far more intense than red light. Indeed, in this picture only about 2 mW of blue light are present, while the red light is more than 100 mW strong. a: weak SFG; b: signal (with tiny amount of SHG); c: idler

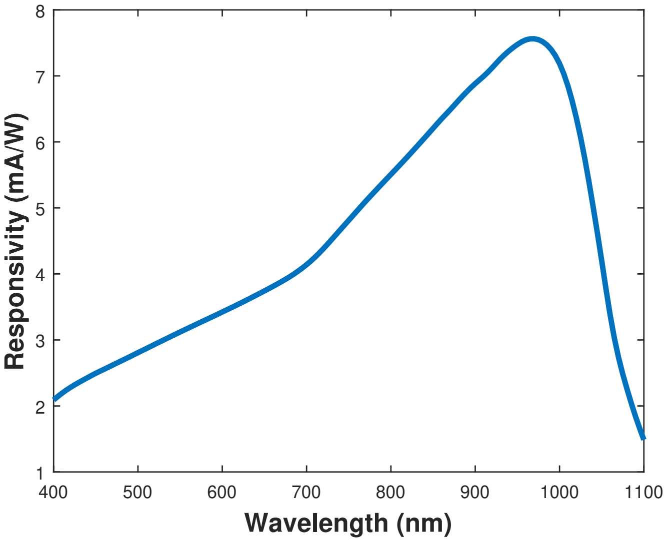

**Figure 6.8: Responsivity of the photodiode power sensor 'S120C' by ThorLabs.** The y-axis shows the internal response of the sensor to the wavelength (x-axis). It can be seen that the behaviour is highly dispersive. The data is provided by ThorLabs [15].

### 6.1.1 Preparation for the measurements

The efficiencies of the processes were sensitive to internal and environmental influences. Thus, the measurements were prepared to run automatically. The vibrations caused by

the placement of the beam blocks into the paths already affected the nonlinear processes and that is why motors were installed to open and close the paths.
Due to availability, the motorized rotation mounts 'PRM1/MZ8' were used, where the aperture was partly blocked by a light-blocking material so that the path could be opened and blocked automatically. The measurement itself is described in chapter 6.2. As a side note, it should be mentioned that the required drivers and the systematic implementation of the shutters was coded based on a Python-library which was implemented by us, which can be easily be adapted for other experiments.

### 6.1.2 Characteristics of the First Crystal

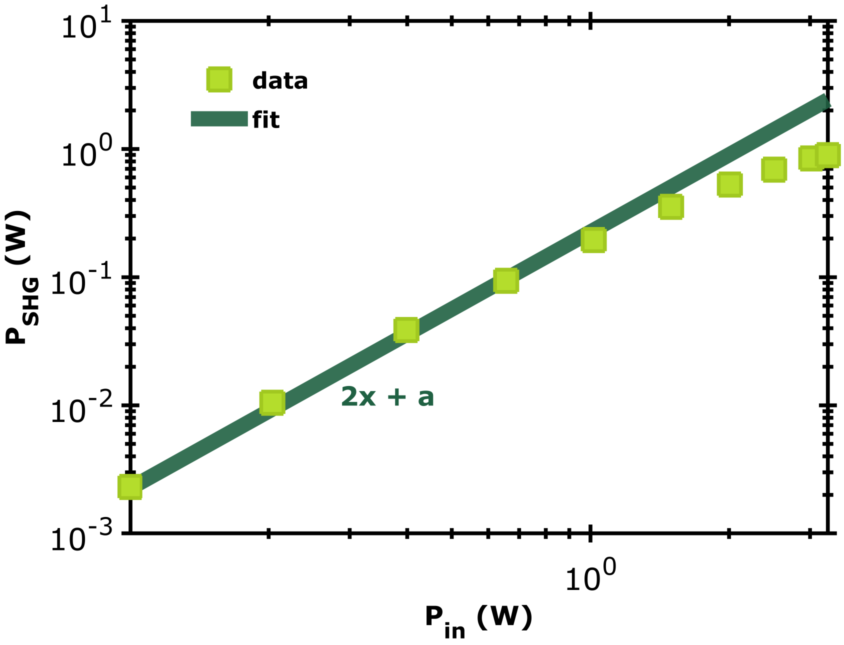

**Figure 6.9: Intensity of the incoming versus the generated light of the crystal used to generate a beam with** $\lambda = 400$ nm **from** $\lambda = 800$ nm. It is plotted on a semi-logarithmic scale to check for the expected quadratic behaviour. The continuous line represents the quadratic fit which is of the form $f(x) = 2x + a$ on the logarithmic scale. The data points have been taken from powers that were measured 30 seconds each. The errors are smaller than the graphical extent of the green squares and therefore do not affect the interpretation in any way.

To check the proper quadratic dependence of the SHG of the $LBO_1$ crystal, the output intensity was measured as a function of the input intensity. While the input intensity was measured before the focal lens $L_1$, the intensity of the blue beam was measured after the dichroic mirror (DM) and the bandpass filter. The measurements were conducted with a thermal power sensor 'S370C' by ThorLabs.
The data is plotted in figure 6.9. It can be seen that the expected quadratic behaviour from equations 3.25 and 3.26 is approximately achieved up to an input power of 1 W.

Although for higher input powers a slowly saturating behaviour sets in, the intensity of the generated beam reaches the required powers for the experiment.

### 6.1.3 The intensity of the red beams

The theoretical calculations from section 4.1.1 showed that the third-order interference component increases with the efficiency of the nonlinear processes. As shown in the provided data in section 6.1, the 50:50 beam splitter tends to deviate from a perfect behaviour as it does not split the power of the beams uniformly. Since the efficiency of the nonlinear processes shows a square dependence on the input power, high intensities are desired. To gain insights into the behaviour of the beam splitter and the influence of other optical elements in the optical path of each beam, the intensities of the signal and idler beams were measured. The histogram of the measured data points is shown in figure 6.10.

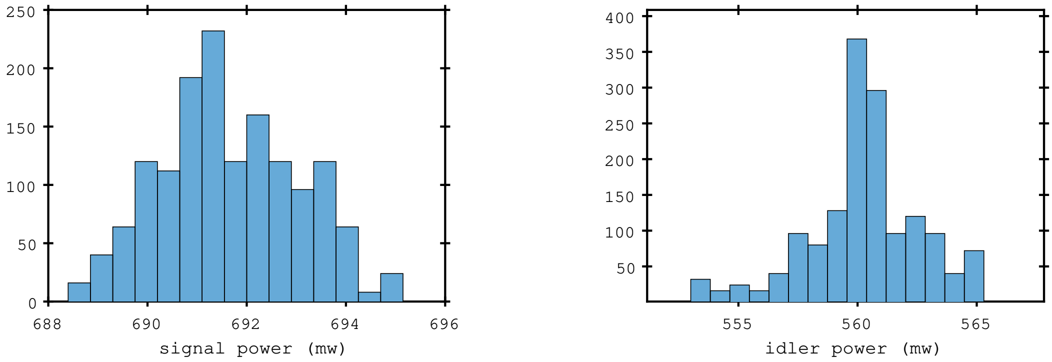

**Figure 6.10: Input powers of signal and idler beams before propagating towards the second LBO-crystal.** The data was taken over 10 seconds each and plotted as a histogram. **Left**: power of the signal beam. **Right**: Power of the idler beam.

Each measurement was acquired for over 10 seconds and the obtained power results are:

$$P_{\text{signal}} = (692 \pm 2)\ \text{mW}$$
$$P_{\text{idler}} = (560 \pm 5)\ \text{mW}$$

The errors were chosen so that the uncertainty interval around the mean value is of 98 % for the signal and 96 % for the idler beam. For a Gaussian distribution, the common error would be determined so that $\bar{x} + \Delta x$ contains about 68.3 % of the measured values and $\bar{x} + 2\Delta x$ contain 95.4 %.

The data shows that the power difference between the signal and the idler beam in this measurement is about $(19\ \pm 1)$ %.

### 6.1.4 Characteristics of the second crystal

To check the behaviour of the system around the $LBO_2$ crystal, the efficiencies of each two-beam scenario was measured as in the terms $P_{12}$, $P_{13}$ and $P_{23}$. Since these processes correspond to SFG and DFG, the same quadratic dependence as described in equation 3.26 is expected between the input power and the power of the generated beam. In the case of the term $P_{12}$ of the Sorkin parameter, this corresponds to a SFG and the obtained power-dependence measurement is plotted in figure 6.11.

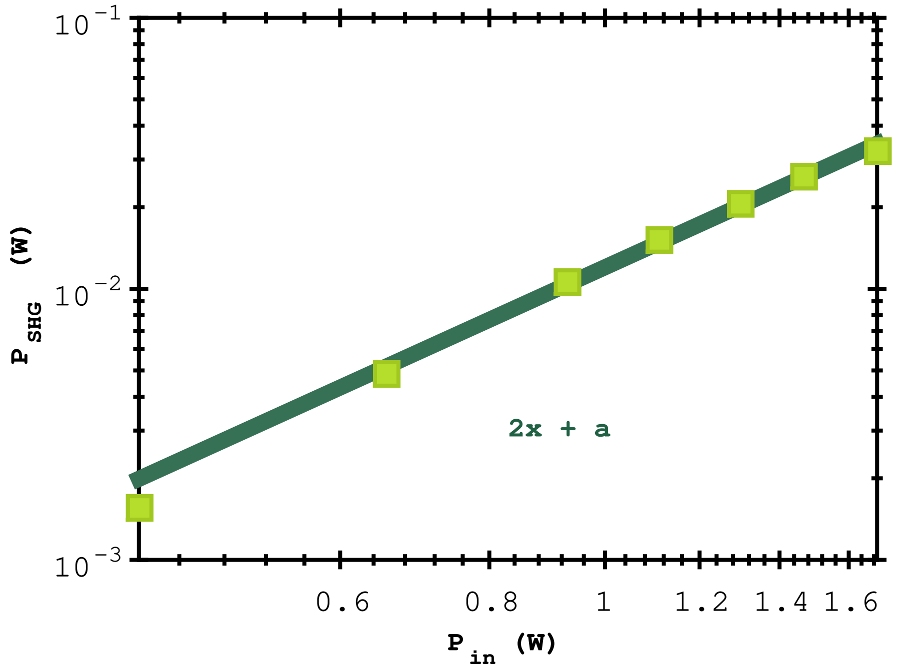

**Figure 6.11: Efficiency of the sum-frequency generation in the $LBO_2$ crystal.** The input power is provided by two different beams, as in the term $P_{12}$. The linear fit to the function $f(x) = 2x + a$ on the logarithmic scale represents a quadratic behaviour. The two experimental data points with the lowest powers were not taken into account in the fit due to the power fluctuations at low input powers. The x-axis represents the input power sent onto the second crystal from the signal and idler beam summed up. The y-axis represents the power of the outcome sum-frequency generation. Each data point was taken over 5 seconds and the error bars were smaller then the graphical points and therefore negligible in this case.

The straight line represents the fit of the function $f(x) = 2x + a$ on the logarithmic scale to the data points and clearly shows the expected quadratic behaviour. The two points at the lowest powers were not taken. Due to the low powers, the processes were not obtained properly.

However, it can be seen that the expected quadratic dependence is observed over the whole input power regime. Due to the lower input powers, compared to the $LBO_1$ crystal, a saturation behaviour cannot be seen. This also makes it clear, that the efficiencies of the process seem to be the limiting factors when it comes to finding third-order interference.

The same measurements were done for the DFG-processes. As shown in figure 6.6 (d), the nonlinear process is observed when the signal or idler and the pump beams are present. Again, a square-behaviour between the input and the output power is expected and actually obtained, which is shown by the dark green fitting line in figure 6.12 (a). Due to the same reasons of inconsistency, as in the SFG-case, the two data points with the lowest powers were ignored while fitting.

The configuration between idler and pump beams seems to be a bit less stable at smaller input powers. Furthermore, as mentioned in section 6.1.3, the idler beam is noticeably weaker compared to the signal beam, which affects the execution of the full experiment. Although the characterization of each process was done independently, when all the terms of the Sorkin parameter were measured, all the processes were simultaneously aligned.

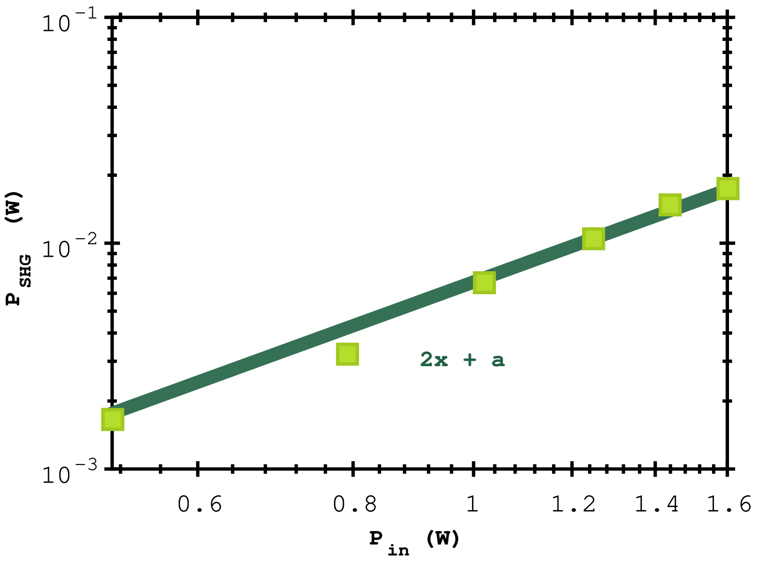

**(a)** Difference-frequency generation between the signal and the pump beam in the second crystal.

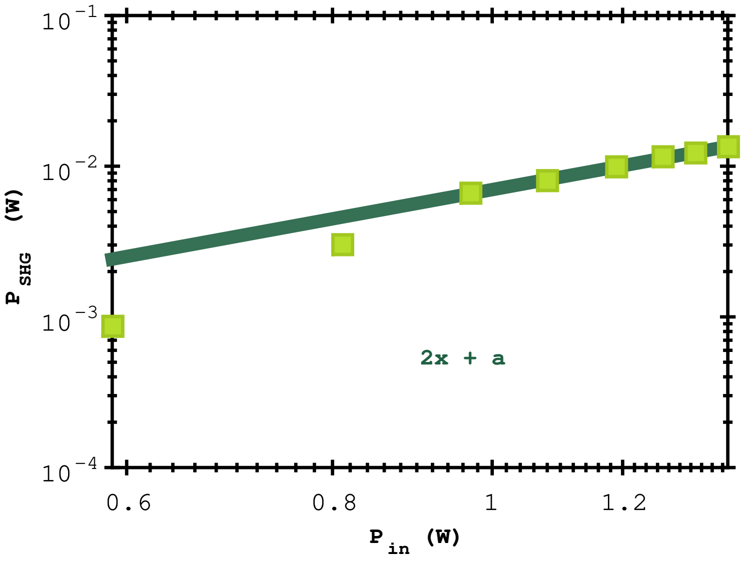

**(b)** Difference-frequency generation between the idler and the pump beam in the second crystal.

**Figure 6.12: Efficiency of the difference-frequency generation processes between the signal/idler and the pump beam in the $LBO_2$ crystal measured as shown in figure 6.6 (d).** The linear fit is again given by the function $f(x) = 2x + a$ and the two experimental data points with the lowest powers were not taken into account in the fit. The x-axis represents the input power sent onto the second crystal from the signal/idler and pump beam summed up. The y-axis represents the power of the generated DFG in the path of the complementary idler/signal mode. Each data point was taken over 5 seconds and the error bars were smaller than the graphical points and therefore negligible for interpreting the behaviour of the nonlinear process.

## 6.2 MEASUREMENTS AND RESULTS

For measuring the Sorkin parameter, each individual term in equation 2.9 has to be obtained; that is $P_{123}$, $P_{12}$, $P_{13}$, $P_{23}$, $P_1$, $P_2$, $P_3$ and $P_0$. Again, this is referring to configurations where $P_{ij}$ coresponds to the paths $i$ and $j$ being open, with $i, j \in [1, 2, 3]$. $P_0$ describes a configuration where all incoming paths are blocked, which represents the background noise. To automatize the measurement, we wrote a program that controls the motors and the measurement time of the powermeter. The motorized mounts open and close the paths, so that the mentioned terms can be measured. After that, the Sorkin parameter was calculated from each data set and was analyzed by to determine the stability and significance.

In this section we introduce two different measurement methods. The 'static measurements' were done with a fixed distance between $L_3$ and $LBO_2$ with an original intention to measure a Sorkin parameter for different input powers and relate them to each other. Instabilities of the individual power terms over time motivated us to introduce a second measurement method, termed as 'z-scans'. With this method we can provide a connection between third-order interference and the nonlinearity of the processes, which is associated with the relative position of $LBO_2$ to $L_3$.

### 6.2.1 Static Measurements

The efficiency of the SFG-generation turned out to be constant over a certain distance between the lens $L_3$ and the crystal $LBO_2$ which agrees with the calculations from section 4.1.1, that the interaction length is significantly smaller than the crystal. After the sum-frequency generation was optimized, the DFG-processes were obtained since the ideal configuration of the phase-matching axis should apply to all three processes simultaneously. As shown in the simulations from section 4, the Sorkin parameter in path 3 seems to be the highest so we decided to measure the power in that path by using the detector position $D_3$ from figure 6.1. The thermal powermeter 'S401C' by ThorLabs was used for the measurements to obtain significant data.

The measured Sorkin parameter shown in figure 6.14 was evaluated from the terms plotted in figure 6.13. Although, the histogram of the Sorkin parameter $\kappa$ looks reasonable, the shape of the terms in figure 6.13 needs further discussion: When looking at the individual terms, one would expect a Gaussian shape for each term when the powers are constant. However, the shape of several terms are not fully Gaussian, which is an indicator of a power drift or a change in efficiency of the nonlinear process.

The mean value of the data of the measurement shown in figure 6.13 is $\bar{\kappa} = 5.47$ mW with the standard deviation of $\sigma_\kappa = 1.49$ mW. Unfortunately, this would only be fully valid as a general statement if all individual terms would be more stable over time and when $\kappa$ would not vary from measurement to measurement. A broadening of the collected data can be caused by the pulse energy variation of the laser. According to [5] the energy of the pulses varies by about 0.1%. When looking at the simple case of

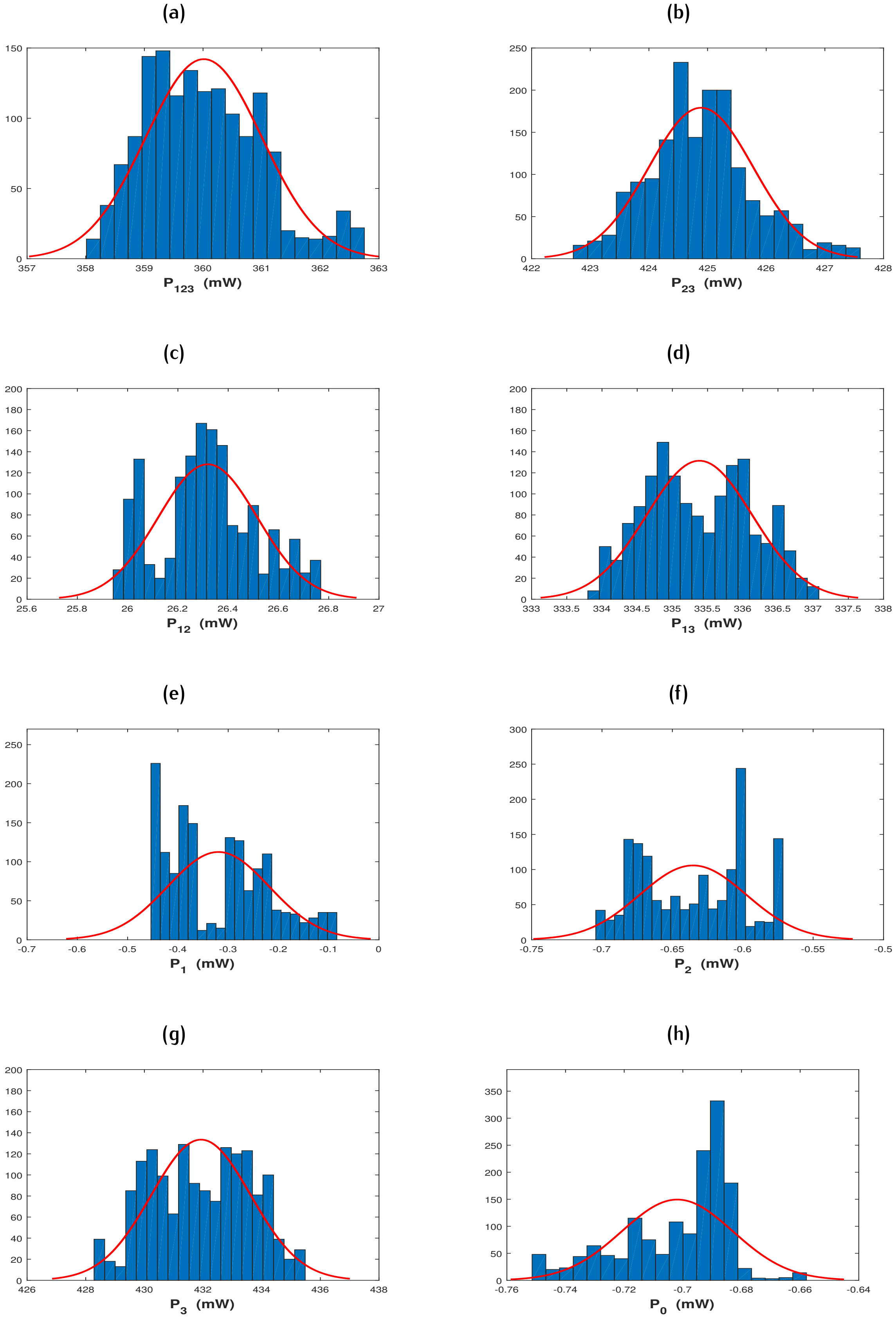

**Figure 6.13: Static Measurement of the individual terms of the Sorkin parameter plotted as histograms.** Each configuration was measured for 7 seconds with a thermal powermeter after adjusting motors and letting the thermal powermeter stabilize for a few seconds.
(**a**): $P_{123}$, (**b**): $P_{23}$, (**c**): $P_{12}$, (**d**): $P_{13}$, (**e**): $P_1$, (**f**): $P_2$, (**g**): $P_3$, (**h**): $P_0$

SHG, the output power of the second-order nonlinear process, $P_{out} \propto (\chi^{(2)})^2 P_{in}^2$, is of the form $f = a \cdot A^b$. The standard deviation on $f$ is given by ([27])

$$\sigma_f = \left| f \cdot b \cdot \frac{\sigma_A}{A} \right| . \tag{6.1}$$

Since $\frac{\sigma_f}{f}$ represents the normalized standard deviation on the output power and $\frac{\sigma_A}{A}$ represents an uncertainty of the input pulse energies of 0.1 %, an uncertainty of 0.2 % can be obtained. In the case of $P_{23}$ with a measured mean value of (26.3 ± 0.2) mW we get a calculated uncertainty due to variation in pulse energy of 0.05 mW. This is in agreement with the collected data and we see that a considerable contribution of the broadening of the collected data can be explained by the pulse energy variation.

When trying different alignments, fairly stable configurations as here were found, but the powers and $\kappa$ were never fully constant over time and several measurements. In section 6.2.2 this instability was further studied, where we measured different Sorkin parameters as a function of the $LBO_2$ crystal position with respect to the lens $L_3$ and observe the evolution of the nonlinear processes as time passes by. These measurements over a longer time period further highlighted that the drift in efficiencies is a limiting factor of fully extracting and quantifying the Sorkin parameter at this point.

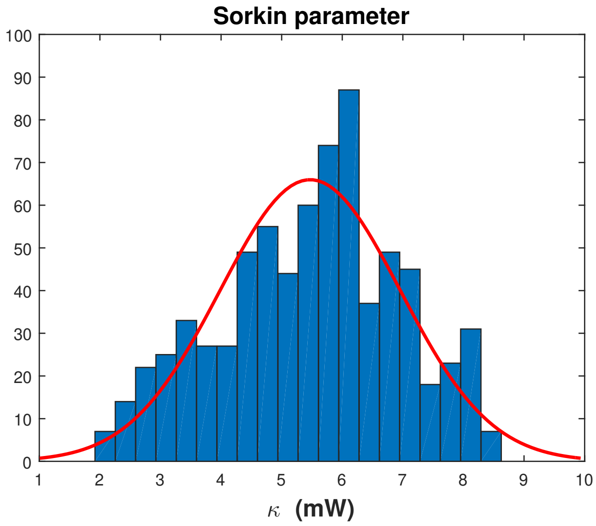

**Figure 6.14: Evaluation of the Sorkin parameter from the data shown in figure 6.13.**

One can understand the influence of the power drift as follows: When looking at the definition of the Sorkin parameter,

$$\kappa = P_{123} - P_{12} - P_{13} - P_{23} + P_1 + P_2 + P_3 - P_0,$$

it becomes clear that instabilities in the setup cause an artificial shift in the Sorkin parameter. For instance, if the SFG processes were present more intensely while measuring $P_{123}$ but the efficiency decreased over time, this leads to an artificial shift of the Sorkin parameter when measuring $P_{12}$ of exactly the change in the power.

Although the obtained data from figure 6.14 looks reasonable, the fluctuations over time and from measurement to measurement are the reason why the obtained Sorkin parameter can not fully be quantified at this point. However, since this data still looks appropriate, we are confident that the obtained third-order interference is a direct consequence of the optical nonlinearities, as predicted.

### 6.2.2 Measurement via a Motorized Translation Stage

We have tried several different adjustments of the setup, such as trying out filters, installing an optical isolator, modifying the laser, etc., to find a fully stable system. Since no modification led to a fully significant and constant result of the Sorkin parameter in the static measurements, a different measurement procedure was tried: To associate third-order interference with the nonlinear coupling of the beams, we decided to measure the individual power terms while moving the crystal in and out of the intersection point of the three beams. Hence, we compare the value of the Sorkin parameter in and out of this point. The motorised translation stage 'MT1-Z6' by ThorLabs was installed ('MTS' in figure 6.1). We also integrated this in our internal library and the program that ran the measurements automatically.
Instead of recording the power at a constant position of the $LBO_2$ crystal with respect to the focal point (static measurement), in this type of measurement the distance between $L_3$ and $LBO_2$ was varied by moving the crystal back and forth, while the power was measured. We referred to these dynamic measurements as 'z-scans'. An interesting insight that was gained by varying the z-positions was the dependence between the position of the $LBO_2$ crystal and the efficiency of the DFG-processes. Other than the SFG-processes, which are present over a relatively long distance, the DFG-processes were shown to be extremely dependent on this relative position between $L_3$ and $LBO_2$. After finding a suitable position of the crystal to optimize the three processes, the z-scan was executed, where the step size and acquisition time per measurement point were carefully chosen to optimize the signal to noise ratio. The idea of this type of measurement is to observe a non-zero Sorkin parameter in the region, where all three nonlinear processes occur.
The results of the measured individual Sorkin terms are plotted in figure 6.15. It is easy to see that in the case of $P_{123}$, where all three processes are present, the maximum nonlinear activities are found somewhere in the range of $z = [-0.6, -0.8]$ mm. As mentioned previously in this chapter, the SFG seems to have a higher tolerance on the crystal position in contrast to the DFG-processes. While the sum-frequency generation has its peak around $z = -0.8$ mm, it is still present to a significant level till $z = -0.2$ mm or even below. However, both difference-frequency generation processes seem to have a discrete peak somewhere in the range of $z = [-0.7, -0.6]$ mm. In the $P_{123}$-term it can be seen, that the input power still fluctuates within the individual regions, meaning that this has to be taken into account when analyzing the Sorkin parameter. In the DFG-terms $P_{13}$ and $P_{23}$ it can be seen that the DFG-processes

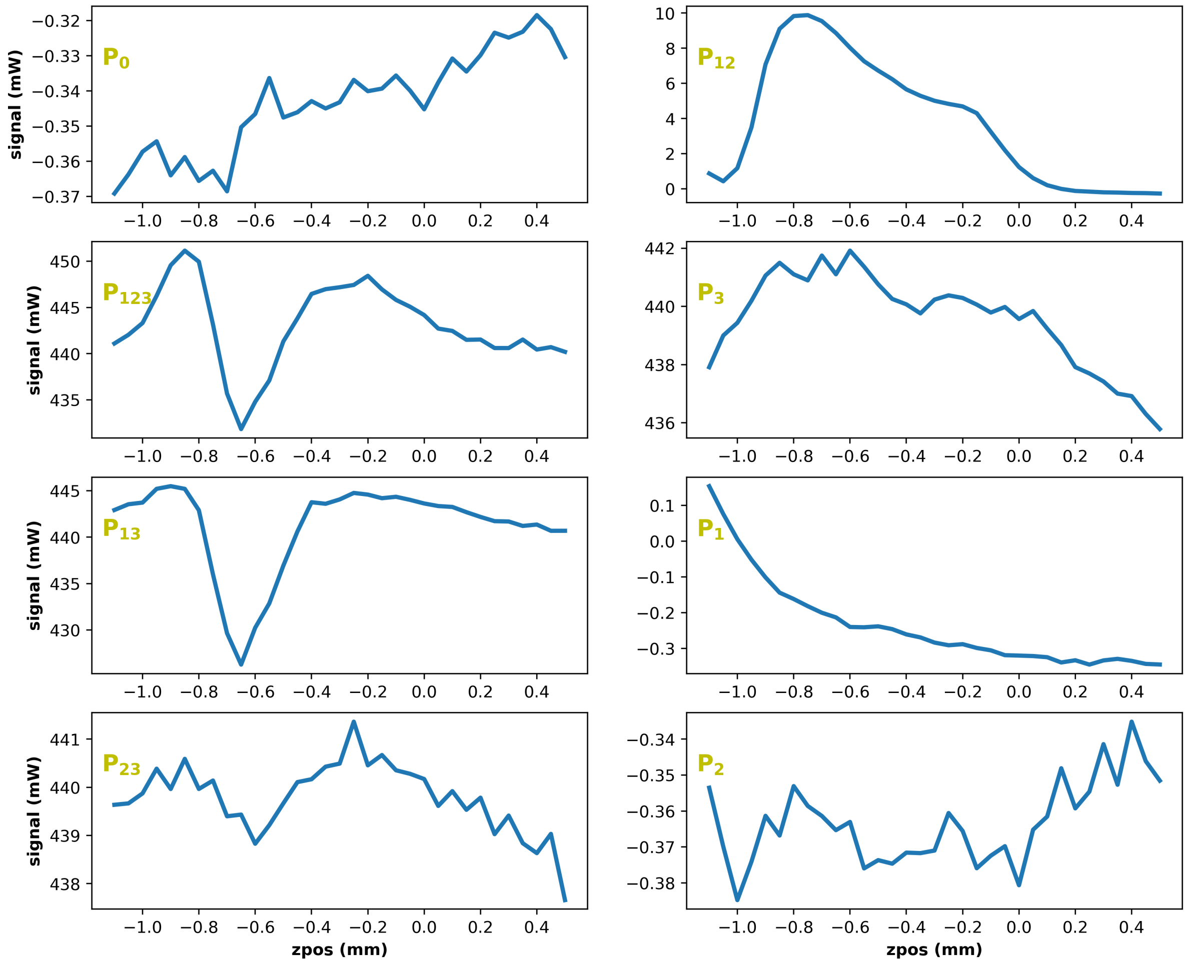

**Figure 6.15: Measuring the individual power configurations by a z-scan.** The x-axis represents the position of the crystal relatively to $L_3$ in mm and the y-axis the measured output power in mW. The stepsize was 50 $\mu$m and the integration time 3 seconds. While the SFG term shows a more continuous behaviour, the DFG powers are clearly maximized around a single peak.

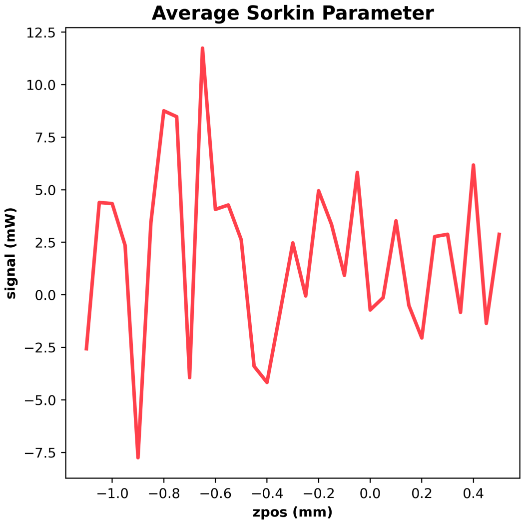

**Figure 6.16: The evaluated Sorkin parameter from the individual measurements shown in figure 6.15.**

cause a drop in the intensity since, as described previously, a certain amount of power is taken out of this path and light is generated in the other paths.
Indeed, the Sorkin parameter was evaluated for each point in the z-scan and the result is shown in figure 6.16. There is a high activity of the Sorkin parameter around the crystal positions at which all the nonlinear processes occur strongest, which makes us confident that there is a non-vanishing third-order interference in this region. However, the fluctuations are too big to make a quantitative claim about the Sorkin parameter from there. Negative values in the individual terms in the zscan as well as in the static measurements are caused by calibration of the powermeter and a slight drift in power over time. Similar to the static measurements, here we also observed that the outcome of the measured Sorkin parameter varies in time. We believe that this is due to the power fluctuations in the system, which are further enhanced due to the nonlinear dependence of the processes on this input power. Nevertheless, we wanted to further study the behaviour over time. To do so, we repeat the same measurement along the z-direction in a loop. The results are shown in figure 6.17 (a) and (b) for the SFG and DFG, respectively. It can be seen that the efficiencies of the process decrease each time the scan is performed. This can be caused by a slight dealignment or directional drift in the laser system over time. The time frame for all the measurements was about 60 minutes.

The Sorkin parameters for the different loops are shown in figure 6.18. It can be seen that the highest values are obtained around the peak of the DFG-processes, where all three processes are present, which confirms the theoretical predictions. The data indicates clearly, that third-order interference is present when the nonlinear processes are present. However, the fluctuations are still too big to fully quantify the definite size of the Sorkin parameter.

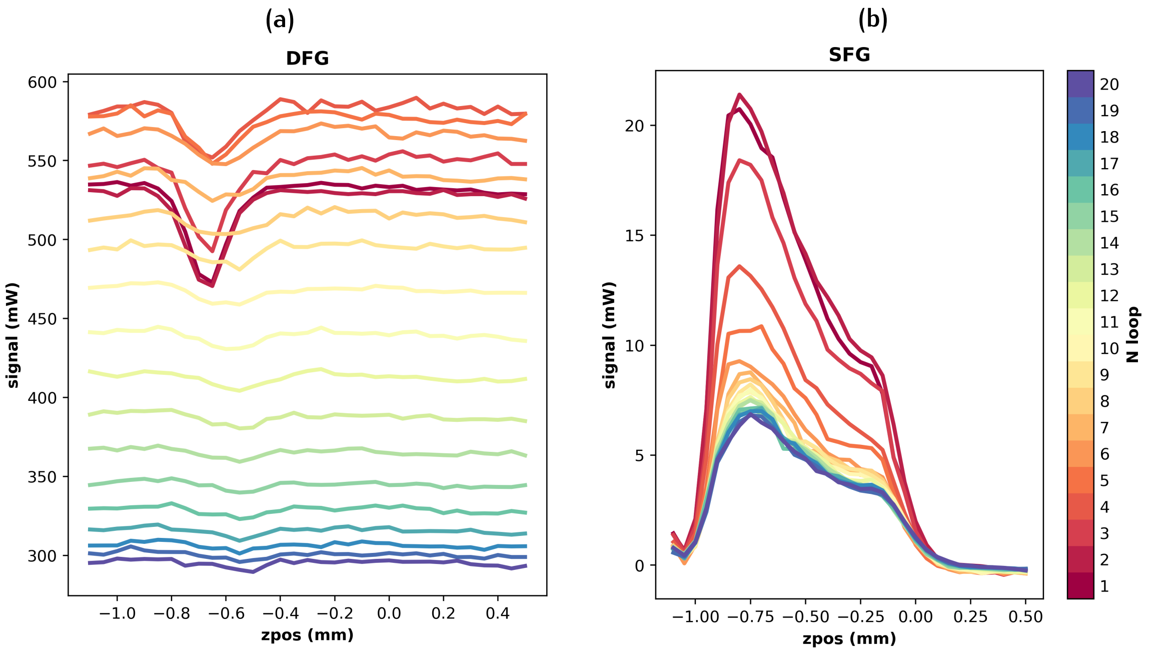

**Figure 6.17: Z-scan measurements over time.** The number of the loop indicates the order in which the measurement was carried out. The results of twenty consecutive loops of the DFG-term $P_{13}$ (**a**) and SFG-term $P_{12}$ (**b**) are shown. In (**a**) there is an increase at the input powers over the first loops. Otherwise the input intensities as well as the efficiencies decrease over time in both processes.

Nevertheless, we are confident that this data confirms the presence of third-order interference in our setup due to the nonlinear optical coupling of the beams.

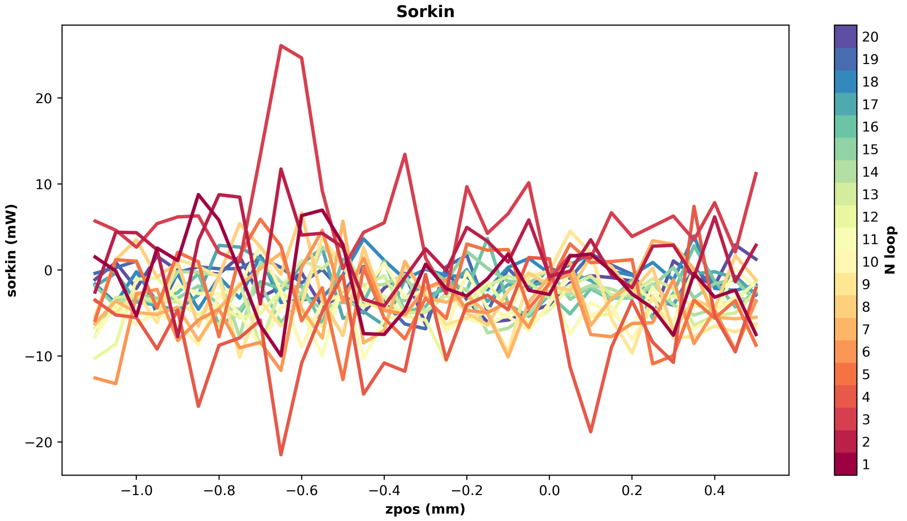

**Figure 6.18: The obtained Sorkin parameters from the different loops shown in figure 6.17.**

# 7 SUMMARY

The aim of this work is to show a new approach to obtain higher-order interference in quantum mechanics and provide the associated quantum mechanical and nonlinear optical descriptions. We could provide nonlinear optical calculations that predict the presence of third-order interference in a system of three laser beams interacting in a $\chi^{(2)}$-medium. The scenario was chosen due to the well-known quantum mechanical Hamiltonian of the system. Although the second-order susceptibility plays the same role in the nonlinear and the quantum descriptions, a general relation between the units used in classical optics and the units in quantum optics was not found in literature. Usually, when associating a quantum mechanical $\chi^{(2)}$ value with an experimental realization, individual assumptions for each system are taken. To circumvent this, a model was obtained successfully from the Hamiltonian and the quantum mechanical description of the input states to describe the occurring processes in the quantum framework and fit to our experimental data. Additionally, we set up an experimental realization of the model. The results of the experiment indicate the presence of third-order interference as predicted by the nonlinear optical calculations. However, the system still showed instabilities and fluctuations in the result that prevented us from completely quantifying the outcome. Our quantum mechanical model and the mathematical treatment can be adapted straight-forward to associate any quantitative measurement of third-order interference with the nonlinearity of the interactions.

By taking a recent description of interference, higher-order interference was shown to be achievable up to an arbitrarily high order by a various number of paths and nonlinear interactions between the paths. We could find a system that is realizable by common elements of nonlinear optics. The basic idea can be broken down to three laser beams interacting in a nonlinear medium. From a well-known description of three-wave mixing in nonlinear optics and newer insights from literature we could show that third-order interference should be present in our setup. This was done by extending the common model to include effects that are usually neglected in simple cases.
We decided for this specific system due to the also well-known description in quantum mechanics.

Since the Hamiltonian and the input states of the system are known, we could come up with a mathematical description to find the $\chi^{(2)}$ value in units matching the Hamiltonian and associate the nonlinearity of our quantum mechanical model to the nonlinearity of the sum-frequency generation processes with experimentally measured data. We did this by formulating the evolution of a quantum state, where a vacuum state is put into a system. The time evolution, expressed by the exponential formulation of the Hamiltonian, then leads to a form where we could perform a Baker-Campbell-Hausdorff expansion. This led to an expansion parameter that could be associated with the nonlinearity of the SHG by fitting it to experimental data. The expansion was shown to be valid when done up to the sixth order. Since the Hamiltonian describes sum-frequency generation as well as difference-frequency generation and therefore also full three-wave mixing, by changing the input states, the nonlinearity of all processes is obtainable by applying the same mathematical treatment. This will be useful when describing a full significant set of measurements that leads to the quantification of higher-order interference within the framework of quantum optics. The obtained third-order interference can then be directly connected to the nonlinearity of the system.

We have also provided an experimental setup that shows third-order interference. The obtained data already indicates the presence of non-vanishing third-order interference very well. However, the instability of the nonlinear process efficiencies and the fluctuations from measurement to measurement have prevented us from quantifying a value of the Sorkin parameter. We are thus optimistic and believe that third-order interference can be fully quantified in the near future by applying the measurement methods that we have provided and automatized.

In addition, the outcome emphasizes that even though a well-established assumption in a specific community is established, such as the reduction of interference to second-order, it does not mean that there is no need for further investigation and extension of that theory.

Since I built the experiment from scratch, I faced many challenges that were new to both me and my colleagues. I also carried out the calculations described in this thesis, with some input from my colleagues (discussed Acknowledgements). This opened up an exciting and challenging path for me, and increased the knowledge and experimental capabilities of our group.

# 8 APPENDIX

### 8.1.1 The setup

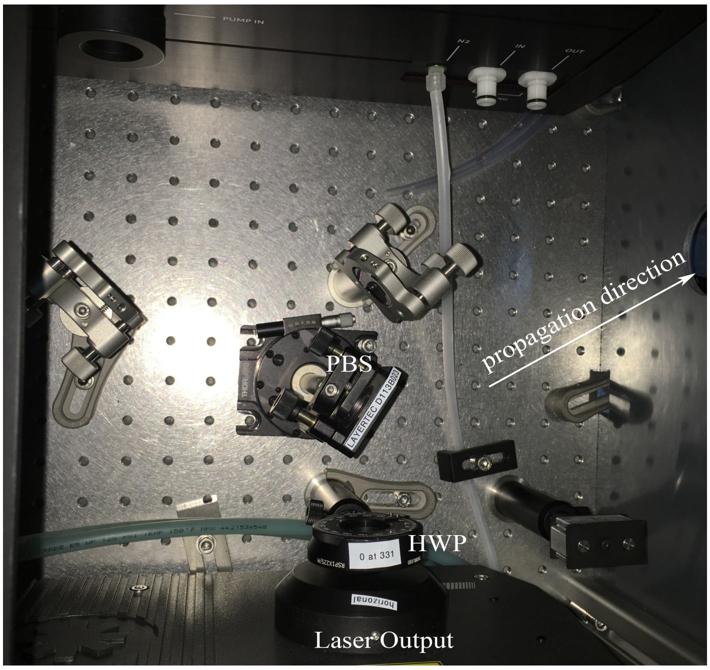

**Figure 8.1: Starting point of the setup.** The output beam of the laser light is sent onto a HWP. By adjusting the HWP the polarization of the light beam can be adjusted. The beam is then propagating towards a PBS and reflected along the direction of our setup when the polarization is horizontally.

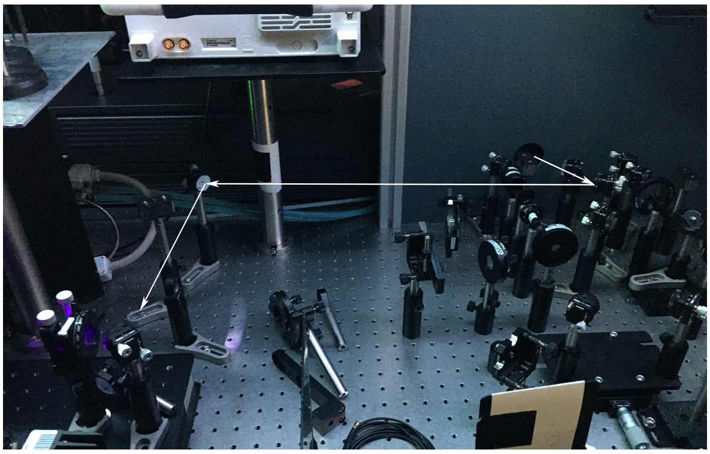

**Figure 8.2: The light beam is sent towards the main component of the setup.**

**Figure 8.3: The main part of the setup.** Red light is sent onto the crystal $LBO_1$. A part of the beam is converted into blue light. By a dichroic mirror, the blue light is then spatially separated from the red light. The red beam is then splitted by a 50:50-beam splitter into two beams. Via three translation stages, a spatial and temporal overlap of the three beams inside the $LBO_2$-crystal can be obtained. The three motors $M_s$, $M_i$ and $M_p$ can open or block the specific parts. The crystal is moved back and forth by a motorized translation stage that conducts the z-scans. A thermal powermeter $D_3$ measures the intensities. The whole movement of the motors and the measurements are controlled by a computer program.

### 8.1.2 Full algebraic expression of the BCH-expansion from chapter 5

$$
\begin{aligned}
O(1) =& \tau\chi\ (a_1 \cdot a_2 \cdot a_3^{\dagger} + a_1^{\dagger} \cdot a_2^{\dagger} \cdot a_3\ )\\
O(2) =& \tau^2\chi^2\ (-a_3^{\dagger} \cdot a_3 + a_1^{\dagger} \cdot a_1 \cdot a_2^{\dagger} \cdot a_2 - a_1^{\dagger} \cdot a_1 \cdot a_3^{\dagger} \cdot a_3 - a_2^{\dagger} \cdot a_2 \cdot a_3^{\dagger} \cdot a_3\ )\\
O(3) =& \tau^3\chi^3\ (-\frac{1}{3}2a_1 \cdot a_2 \cdot a_3^{\dagger} - \frac{2}{3}a_1^{\dagger} \cdot a_2^{\dagger} \cdot a_3 + \frac{2}{3}a_1 \cdot a_2 \cdot a_3^{\dagger 2} \cdot a_3 - \frac{2}{3}a_1 \cdot a_2^{\dagger} \cdot a_2^{2} \cdot a_3^{\dagger}\\
& - \frac{2}{3}a_1^{\dagger} \cdot a_1^{2} \cdot a_2 \cdot a_3^{\dagger} + \frac{2}{3}a_1^{\dagger} \cdot a_2^{\dagger} \cdot a_3^{\dagger} \cdot a_3^{2} - \frac{2}{3}a_1^{\dagger} \cdot a_2^{\dagger 2} \cdot a_2 \cdot a_3 - \frac{2}{3}a_1^{\dagger 2} \cdot a_1 \cdot a_2^{\dagger} \cdot a_3)\\
O(4) =& \tau^4\chi^4\ (\frac{a_3^{\dagger} \cdot a_3}{3} - \frac{1}{3}a_3^{\dagger 2} \cdot a_3^{2} + \frac{1}{2}a_1^{2} \cdot a_2^{2} \cdot a_3^{\dagger 2} + \frac{1}{2}a_1^{\dagger 2} \cdot a_2^{\dagger 2} \cdot a_3^{2} - \frac{1}{3}a_1^{\dagger} \cdot a_1 \cdot a_2^{\dagger} \cdot a_2\\
& - \frac{1}{3}a_1^{\dagger} \cdot a_1 \cdot a_2^{\dagger 2} \cdot a_2^{2} + a_1^{\dagger} \cdot a_1 \cdot a_3^{\dagger} \cdot a_3 - \frac{1}{3}a_1^{\dagger} \cdot a_1 \cdot a_3^{\dagger 2} \cdot a_3^{2} - \frac{1}{3}a_1^{\dagger 2} \cdot a_1^{2} \cdot a_2^{\dagger} \cdot a_2\\
& + \frac{1}{3}a_1^{\dagger 2} \cdot a_1^{2} \cdot a_3^{\dagger} \cdot a_3 + a_2^{\dagger} \cdot a_2 \cdot a_3^{\dagger} \cdot a_3 - \frac{1}{3}a_2^{\dagger} \cdot a_2 \cdot a_3^{\dagger 2} \cdot a_3^{2} + \frac{1}{3}a_2^{\dagger 2} \cdot a_2^{2} \cdot a_3^{\dagger} \cdot a_3\\
& + 2a_1^{\dagger} \cdot a_1 \cdot a_2^{\dagger} \cdot a_2 \cdot a_3^{\dagger} \cdot a_3)\\
O(5) =& \tau^5\chi^5\ (\frac{2}{15}a_1 \cdot a_2 \cdot a_3^{\dagger} + \frac{2}{15}a_1^{\dagger} \cdot a_2^{\dagger} \cdot a_3 - \frac{4}{3}a_1 \cdot a_2 \cdot a_3^{\dagger 2} \cdot a_3 + \frac{2}{15}a_1 \cdot a_2 \cdot a_3^{\dagger 3} \cdot a_3^{2}\\
& + \frac{2}{5}a_1 \cdot a_2^{\dagger} \cdot a_2^{2} \cdot a_3^{\dagger} + \frac{2}{15}a_1 \cdot a_2^{\dagger 2} \cdot a_2^{3} \cdot a_3^{\dagger} + \frac{2}{5}a_1^{\dagger} \cdot a_1^{2} \cdot a_2 \cdot a_3^{\dagger}\\
& - \frac{4}{3}a_1^{\dagger} \cdot a_2^{\dagger} \cdot a_3^{\dagger} \cdot a_3^{2} + \frac{2}{15}a_1^{\dagger} \cdot a_2^{\dagger} \cdot a_3^{\dagger 2} \cdot a_3^{3} + \frac{2}{5}a_1^{\dagger} \cdot a_2^{\dagger 2} \cdot a_2 \cdot a_3\\
& + \frac{2}{15}a_1^{\dagger} \cdot a_2^{\dagger 3} \cdot a_2^{2} \cdot a_3 + \frac{2}{5}a_1^{\dagger 2} \cdot a_1 \cdot a_2^{\dagger} \cdot a_3 + \frac{2}{15}a_1^{\dagger 2} \cdot a_1^{3} \cdot a_2 \cdot a_3^{\dagger} + \frac{2}{15}a_1^{\dagger 3} \cdot a_1^{2} \cdot a_2^{\dagger} \cdot a_3\\
& - \frac{13}{15}a_1 \cdot a_2^{\dagger} \cdot a_2^{2} \cdot a_3^{\dagger 2} \cdot a_3 - \frac{13}{15}a_1^{\dagger} \cdot a_1^{2} \cdot a_2 \cdot a_3^{\dagger 2} \cdot a_3 + \frac{13}{15}a_1^{\dagger} \cdot a_1^{2} \cdot a_2^{\dagger} \cdot a_2^{2} \cdot a_3^{\dagger}\\
& - \frac{13}{15}a_1^{\dagger} \cdot a_2^{\dagger 2} \cdot a_2 \cdot a_3^{\dagger} \cdot a_3^{2} - \frac{13}{15}a_1^{\dagger 2} \cdot a_1 \cdot a_2^{\dagger} \cdot a_3^{\dagger} \cdot a_3^{2} + \frac{13}{15}a_1^{\dagger 2} \cdot a_1 \cdot a_2^{\dagger 2} \cdot a_2 \cdot a_3)\\
O(6) =& \tau^6\chi^6(\frac{1}{45}(-2)a_3^{\dagger} \cdot a_3 + \frac{4}{9}a_3^{\dagger 2} \cdot a_3^{2} - \frac{2}{45}a_3^{\dagger 3} \cdot a_3^{3} - \frac{1}{2}a_1^{2} \cdot a_2^{2} \cdot a_3^{\dagger 2} - \frac{1}{2}a_1^{\dagger 2} \cdot a_2^{\dagger 2} \cdot a_3^{2}\\
& + \frac{1}{3}a_1^{2} \cdot a_2^{2} \cdot a_3^{\dagger 3} \cdot a_3 - \frac{1}{3}a_1^{2} \cdot a_2^{\dagger} \cdot a_2^{3} \cdot a_3^{\dagger 2} + \frac{2}{45}a_1^{\dagger} \cdot a_1 \cdot a_2^{\dagger} \cdot a_2 + \frac{2}{15}a_1^{\dagger} \cdot a_1 \cdot a_2^{\dagger 2} \cdot a_2^{2}\\
& + \frac{2}{45}a_1^{\dagger} \cdot a_1 \cdot a_2^{\dagger 3} \cdot a_2^{3} - \frac{14}{45}a_1^{\dagger} \cdot a_1 \cdot a_3^{\dagger} \cdot a_3 + \frac{46}{45}a_1^{\dagger} \cdot a_1 \cdot a_3^{\dagger 2} \cdot a_3^{2}\\
& - \frac{2}{45}a_1^{\dagger} \cdot a_1 \cdot a_3^{\dagger 3} \cdot a_3^{3} - \frac{1}{3}a_1^{\dagger} \cdot a_1^{3} \cdot a_2^{2} \cdot a_3^{\dagger 2} + \frac{2}{15}a_1^{\dagger 2} \cdot a_1^{2} \cdot a_2^{\dagger} \cdot a_2\\
& + \frac{13}{45}a_1^{\dagger 2} \cdot a_1^{2} \cdot a_2^{\dagger 2} \cdot a_2^{2} - \frac{4}{15}a_1^{\dagger 2} \cdot a_1^{2} \cdot a_3^{\dagger} \cdot a_3 + \frac{13}{45}a_1^{\dagger 2} \cdot a_1^{2} \cdot a_3^{\dagger 2} \cdot a_3^{2}\\
& + \frac{1}{3}a_1^{\dagger 2} \cdot a_2^{\dagger 2} \cdot a_3^{\dagger} \cdot a_3^{3} - \frac{1}{3}a_1^{\dagger 2} \cdot a_2^{\dagger 3} \cdot a_2 \cdot a_3^{2} - \frac{1}{3}a_1^{\dagger 3} \cdot a_1 \cdot a_2^{\dagger 2} \cdot a_3^{2} + \frac{2}{45}a_1^{\dagger 3} \cdot a_1^{3} \cdot a_2^{\dagger} \cdot a_2\\
& - \frac{2}{45}a_1^{\dagger 3} \cdot a_1^{3} \cdot a_3^{\dagger} \cdot a_3 - \frac{14}{45}a_2^{\dagger} \cdot a_2 \cdot a_3^{\dagger} \cdot a_3 \frac{46}{45}a_2^{\dagger} \cdot a_2 \cdot a_3^{\dagger 2} \cdot a_3^{2} - \frac{2}{45}a_2^{\dagger} \cdot a_2 \cdot a_3^{\dagger 3} \cdot a_3^{3}\\
& - \frac{4}{15}a_2^{\dagger 2} \cdot a_2^{2} \cdot a_3^{\dagger} \cdot a_3 + \frac{13}{45}a_2^{\dagger 2} \cdot a_2^{2} \cdot a_3^{\dagger 2} \cdot a_3^{2} - \frac{2}{45}a_2^{\dagger 3} \cdot a_2^{3} \cdot a_3^{\dagger} \cdot a_3\\
& - \frac{116}{45}a_1^{\dagger} \cdot a_1 \cdot a_2^{\dagger} \cdot a_2 \cdot a_3^{\dagger} \cdot a_3 + \frac{58}{45}a_1^{\dagger} \cdot a_1 \cdot a_2^{\dagger} \cdot a_2 \cdot a_3^{\dagger 2} \cdot a_3^{2}\\
& - \frac{58}{45}a_1^{\dagger} \cdot a_1 \cdot a_2^{\dagger 2} \cdot a_2^{2} \cdot a_3^{\dagger} \cdot a_3 - \frac{58}{45}a_1^{\dagger 2} \cdot a_1^{2} \cdot a_2^{\dagger} \cdot a_2 \cdot a_3^{\dagger} \cdot a_3\ )
\end{aligned}
\tag{8.1}
$$

# 9 BIBLIOGRAPHY

[1] AS Photonics. SNLO v.75. `https://as-photonics.com/`, 08/10/2020.

[2] R. S. Aspden, M. J. Padgett, and G. C. Spalding. Video recording true single-photon double-slit interference. *American Journal of Physics*, 84(9):671–677, 2016.

[3] M. Barner and F. Flohr. *Analysis I*. De Gruyter, 1991.

[4] Robert W. Boyd. *Nonlinear Optics, Third Edition*. Academic Press, Inc., USA, 3rd edition, 2008.

[5] Inc. Coherent. *Mira Optima 900-F Laser Operatorís Manual*. 5100 Patrick Henry DriveSanta Clara, CA 95054, 2004.

[6] Georgia State Univesity C.R. Nave. Hyperphysics - multiple slit diffraction, 2016.

[7] C. Davisson and L.H. Germer. Diffraction of electrons by a crystal of nickel. *Phys. Rev.*, 30:705–740, 1927.

[8] R. P. Feynman. Space-Time Approach to Non-Relativistic Quantum Mechanics. pages 71–109, 2005.

[9] C. Gerry and P. Knight. *Introductory Quantum Optics*. Cambridge University Press, 2005.

[10] F. Grossmann. A short introduction to laser physics. In *Theoretical Femtosecond Physics*, pages 3–17. Springer International Publishing, 2018.

[11] W. Haifeng and A. M. Weiner. Efficiency of short-pulse type-i second-harmonic generation with simultaneous spatial walk-off, temporal walk-off, and pump depletion. *IEEE Journal of Quantum Electronics*, 39(12):1600–1618, 2003.

[12] Castech Inc. Crystal catalog 2017. 2017.

[13] Thorlabs Inc. Product details - longpass dichroic mirrors/beamsplitters. `https://www.thorlabs.com/newgrouppage9.cfm?objectgroup_id=3313`,accessed: 28.09.2020, 2020.

[14] Thorlabs Inc. Product details - non-polarizing cube beamsplitters. `https://www.thorlabs.com/newgrouppage9.cfm?objectgroup_id=6207`, accessed:28.09.2020, 2020.

[15] Thorlabs Inc. Product Details - Photodiode Power Sensors (C-Series). `https://www.thorlabs.com/newgrouppage9.cfm?objectgroup_id=3328`, accesses: 28.09.2020, 2020.

[16] T. Jiang, D. Huang, J. Cheng, X. Fan, Z. Zhang, Y. Shan, Y. Yi, Y. Dai, L. Shi, K. Liu, and et al. Gate-tunable third-order nonlinear optical response of massless dirac fermions in graphene. *Nature Photonics*, 12(7):430–436, 2018.

[17] O. S. Magaña-Loaiza, I. De Leon, M. Mirhosseini, R. Fickler, A. Safari, U. Mick, B. McIntyre, P. Banzer, B. Rodenburg, G. Leuchs, and R. W. Boyd. Exotic looped trajectories of photons in three-slit interference. *Nature Communications*, 7(1), 2016.

[18] L. Mandel and E. Wolf. *Optical Coherence and Quantum Optics*. EBL-Schweitzer. Cambridge University Press, 1995.

[19] J. E. Midwinter and J. Warner. The effects of phase matching method and of uniaxial crystal symmetry on the polar distribution of second-order non-linear optical polarization. *British Journal of Applied Physics*, 16(8):1135–1142, 1965.

[20] G. Rengaraj, U. Prathwiraj, S. N. Sahoo, R Somashekhar, and U. Sinha. Measuring the deviation from the superposition principle in interference experiments. *New Journal of Physics*, 20(6):063049, 2018.

[21] L. A. Rozema, Z. Zhuo, T. Paterek, and B. Dakić. Higher-order interference in quantum physics. `https://arxiv.org/pdf/2003.11048.pdf`, 2020.

[22] B. E. A. Saleh and M.C. Teich. *Fundamentals of photonics; 2nd ed.* Wiley series in pure and applied optics. Wiley, New York, NY, 2007.

[23] R. Sawant, J. Samuel, A. Sinha, S. Sinha, and U. Sinha. Nonclassical paths in quantum interference experiments. *Phys. Rev. Lett.*, 113:120406, 2014.

[24] U. Sinha, C. Couteau, T. Jennewein, R. Laflamme, and G. Weihs. Ruling out multi-order interference in quantum mechanics. *Science*, 329(5990):418–421, 2010.

[25] A. V. Smith, D. J. Armstrong, and W. J. Alford. Increased acceptance bandwidths in optical frequency conversion by use of multiple walk-off-compensating nonlinear crystals. *J. Opt. Soc. Am. B*, 15(1):122–141, 1998.

[26] R. D. Sorkin. Quantum mechanics as quantum measurement theory. *Modern Physics Letters A*, 09(33):3119–3127, 1994.

[27] Wikipedia. Propagation of uncertainty. `https://en.wikipedia.org/wiki/Propagation_of_uncertainty`, accessed: 14/01/2021, 2020.

[28] Wikipedia. Wave interference. `https://en.wikipedia.org/wiki/Wave_interference`, accessed: 21/05/2020, 2020.

[29] Wikipedia. Coherence (physics). `https://en.wikipedia.org/wiki/Coherence_(physics)`, accessed: 14/01/2021, 2021.

[30] H. Yabuki. Feynman path integrals in the young double-slit experiment. *International Journal of Theoretical Physics*, 25(2):159–174, 1986.

[31] T. Young. II. the bakerian lecture. on the theory of light and colours. *Philosophical Transactions of the Royal Society of London*, 92:12–48, 1802.

[32] N. Zettili. *Quantum Mechanics: Concepts and Applications*. Wiley, 2009.